Università degli Studi di Genova

Scuola di Scienze Matematiche, Fisiche e Naturali

Doctorate in Sciences and Technologies of Chemistry and Materials

Curriculum: Science and Technology of Materials

Polymer Photonic Structures

for

Thermal Management

Candidate: Andrea LANFRANCHI

Matr. n. 4196732

Supervisor: Prof. Davide COMORETTO

XXXVII Cycle of the Doctorate Program, 2021-2024

Summary

Introduction & Overview

I begin the thesis with a short description of its title, which may sound a bit esoteric. “Photonic structures” in this case is primarily related to dielectric mirrors, also known as distributed Bragg reflectors. These structures, that will be presented thoroughly in **Chapter 1**, are essentially very effective mirrors for tunable, restricted spectral ranges. Instead, “thermal management” – on its own quite vague – refers to the passive reduction of heating of items in situation of exposure to sunlight and environmental conditions. Therefore, the overall goal of the PhD project was to develop photonic structures able to reduce the heating by screening objects, or even cooling them down in a passive, zero energy consumption manner. This will be apparent in the **Chapters 2** and **3**, dedicated to the fabrication of dielectric mirrors (aegises) able to reflect selectively near infrared light reducing strongly the heating of objects exposed to light irradiation. As aegises cannot lower the temperature below ambient, in **Chapter 4** I will report the results achieved in the field of radiative cooling and how it can help towards our goals – hence, this chapter is strictly linked to the main research topic as well.

The connection to other parts of the thesis to the main topic may however seem less obvious; to an extent, the part about “thermal management” is dropped in favor of the “photonic structures”. Indeed, **Chapter 5** reports the results I achieved during my period abroad at École Polytechnique Fédérale de Lausanne, where I worked on the assembly of an external cavity laser setup – quite far from the thermal management field. The intent behind working on such a different, heavily physics-oriented topic was to provide me with a different point of view on scientific research. The idea and main driving force for this research was therefore to make me, used to work in material science/chemistry environment, see the other side of the palisade studying from a Physics viewpoint, in virtue of my relatively interdisciplinary background (from a Physics bachelor to a PhD in an industrial chemistry department). Still, the topic is not completely unrelated; indeed, as I will explain in depth, the dielectric mirrors I initially fabricated for thermal shielding applications were effectively used as outcouplers for the external cavity laser assembly.

Along this line of exploring viewpoints and exploiting the expertise developed working on my main research, I cooperated with many other colleagues, both inside and outside the research group and the University of Genoa, on different topics related to application of photonic structures, as I will report in **Chapter 6**.

Overview. The thesis will be structured in six different chapters:

- **Chapter 1** will briefly introduce the topic of distributed Bragg reflectors and will serve as a general theoretical introduction to **Chapters 2**, **3** and **6**, as well as parts of **Chapters 4** and **5**. The general theory presented can be found on many books on the topic – Saleh's *Fundamentals of Photonics*, Giusfredi's *Manual of Optics*, Hecht's *Optics*, and especially MacLeod's *Thin Film Optical Filters* to cite some – but the data reported are calculated with codes developed by me over the years.
- **Chapter 2** will introduce the problem of excessive heating, the use of air conditioning and the challenges of managing temperature of indoor environments in a warming climate.
  The work on aegises for thermal management will be presented, intended as distributed Bragg reflectors reflecting near-infrared radiation. In the chapter, the first instances of this kind of structures are designed, reported, characterized and tested for thermal shielding, achieving promising results. The data presented were published in Lanfranchi et al., *ACS Appl. Mater. Interfaces* 2022, **14,** 12**,** 14550.
- **Chapter 3** will continue the same line of research, following the results reported in Lanfranchi et al., *Chem. Eng. Sci.* 2024, **283**, 5, 119377. The chapter will delve deeper into the topic of all-polymer aegises, providing a complete design rationale, followed by an exploration of the different materials that can be used and their influence on the thermal shielding performances with a complete characterization of the samples.
- **Chapter 4** will transition from thermal shielding to radiative cooling, providing a different example of passive thermal management. The focus will be on the challenges of the research field, the building of a quantitative model to describe the phenomenon as well as reporting the results achieved so far with various measuring setup and structures. All data reported are unpublished.
- **Chapter 5** reports the results I obtained during my period abroad, while I was working on the assembly of an external cavity laser setup by Prof. Benea-Chelmus at École Polytechnique Fédérale de Lausanne (CH). The workflow for the assembly of the setup in its iterations, the characterization of the parts and the final results will be presented. All the data reported are unpublished.
- **Chapter 6** will briefly report the results of all the collaborations and side projects I worked on during this years. Most of them will be published results (Megahd et al., *ACS Omega* 2024, **7**, 18, 15499; *Mater. Chem. Frontiers* 2022, **6**, 17, 2413; Benvenuti et al., *J. Mater. Chem. C* 2024, 12, 12, 4243; Magnasco et al., ACS Omega 2024, **9**, 41, 42375; Martusciello et al., ACS *Appl. Mater. Interfaces* 2024, **16**, 38, 51384; Baouch et al., *Add. Manufactur*, 2024, 83, 31,

104063), with few relative to work in preparation (Martusciello et al., submitted 2024, Di Fonzo et al., in preparation).

- **Appendices** contain the Fresnel coefficients (**A.1**), a thorough description of transfer matrix method (**A.2**) and additional details on experimental procedures (**B.1**).

Chapter 1. Photonic Structures

In this first chapter, I will temporarily postpone the full discussion of the thermal management issue and the motivation to pursue its solution, which will be thoroughly presented in the **Introduction** to **Chapter 1**. I will focus instead on the photonic structures used in this thesis which are the fundamentals for **Chapters 2,3** and **6**, plus part of **Chapter 4** and **5**. To give some context, the idea behind the thermal management is to fabricate structures that are reflective in the near-infrared range whereas remaining transparent or almost transparent in the visible (Vis) range, to effectively shield materials from sunlight reducing their heating up. The path I followed to do so is using the so-called distributed Bragg reflectors (DBRs) or dielectric mirrors. The typical cross-section of a DBR is reported in Figure 1.1a: a stack of thin films, with periodically alternating refractive index.[1-3]

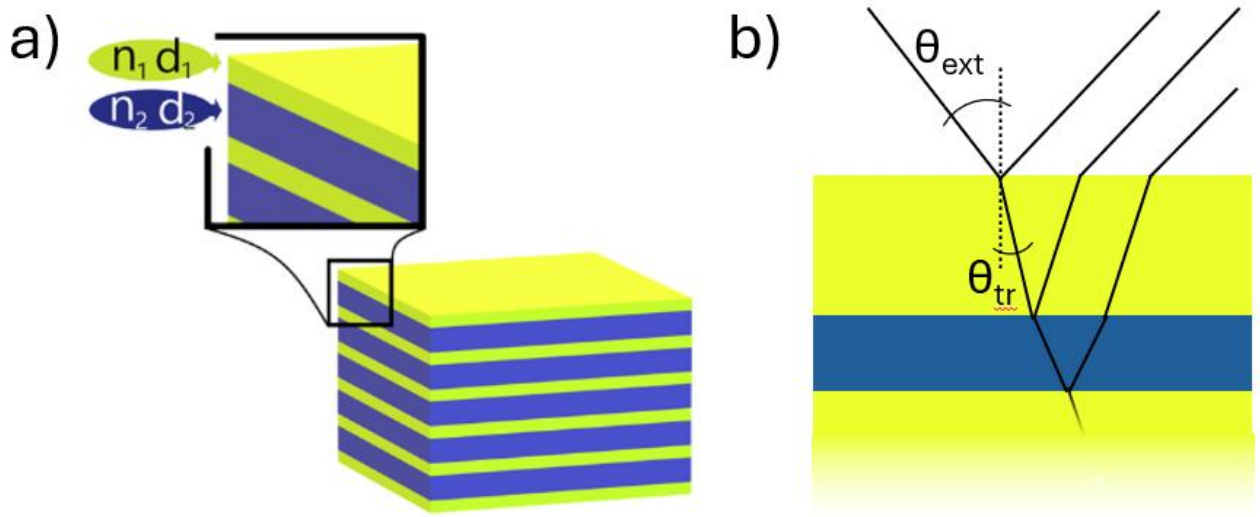

Figure 1.1. **a)** *Schematic of a standard distributed Bragg reflectors made up by repeating periodically a single BL. The BL is defined as a film of two materials of refractive indices* n_1, n_2 *and thicknesses* d_1, d_2. **b)** *Schematic of the reflection and propagation of light rays due to the presence of the DBR.*

The fundamental pair or layers (bilayer, BL) is composed of one layer with higher refractive index n_H and thickness d_H, and another layer with lower refractive index n_L and thickness d_L. The periodicity of the system, given by the sum $D = d_H + d_L$, is usually in the same order of magnitude of the visible (Vis) or near-infrared (NIR) wavelength, hence a few hundreds of nanometers.

Considering the schematization in **Figure 1.1b**, which shows the propagation of radiation incident on a multilayer structure at an angle θ_{ext} relative to the normal. The light encounters the first interface, from air to material 1, where it undergoes reflection and transmission. The transmitted wave continues within the material; upon reaching the 1→2 interface, it undergoes further reflection and transmission,

then proceeds within medium 2, encounters the 2→1 interface, and so on until the end of the multilayer, assuming no absorption occurs. The reflected rays travel back through the structure to the surface, where they interfere with each other, and so do the refracted ones exiting the structure. For certain wavelengths, the radiation experiences destructive interference, where the waves cancel each other out and are not detected in the spectra, while for others, constructive interference occurs. This is a diffraction phenomenon, similar in principle to the Bragg one for X-rays with crystal planes. The diffraction orders are observable as high-reflectance, low-transmittance spectral regions due to the constructive interference of the backward-travelling rays (and destructive interference of the forward-travelling ones). As photon propagation is effectively impeded, these regions are called "photon bandgaps" (bandgaps), in analogy to semiconductor physics.[4]

The spectral position of the bandgaps are given by Bragg diffraction and the refraction given by Snell's law, combining the two into Bragg-Snell law:[2, 5]

$$m\lambda_m = 2D\sqrt{n_{eff}^2 - sin^2\vartheta_{ext}} \qquad m = 1, 2, 3 \ldots \tag{1.1}$$

For $m = 1$ Equation 1.1 give the spectral position λ_1 of the first bandgap, which depends on the periodicity D and the effective refractive index of the structure $n_{eff} = \sqrt{\frac{n_H^2 d_H + n_L^2 d_L}{D}} \cong \frac{n_H d_H + n_L d_L}{D}$. The latter is derived from the volume average of the dielectric functions of the two media, and usually can be approximated with the volume average of the refractive indices. As seen by the inclusion of the angle of incidence of light ϑ_{ext} in Bragg-Snell law, the optical response of DBRs show angular dispersion, its bandgaps shifting towards shorter wavelengths as the angle increases; at normal incidence, however, **Equation 1.1** simplifies to **Equation 1.2**:

$$m\lambda_m \cong 2\cancel{D}\frac{n_H d_H + n_L d_L}{\cancel{D}} \cong 2(n_H d_H + n_L d_L) \tag{1.2}$$

From **Equation 1.2** (which is slightly approximated) the effect of layers thickness and refractive index is apparent as the spectral position of the first bandgap is double the sum of the optical thicknesses $n_j d_j$ (for $j = H, L$) of the building blocks.

Other reflection peaks are observed for $m = 2, 3 \ldots$, at the corresponding integer fractions of the value obtained for $m = 1$. These peaks are usually labeled according to their m value and referred to as 2nd, 3rd... diffraction order, or 2nd, 3rd… order bandgap.[2, 6]

Tuning thicknesses and refractive indices allow DBRs to perform as effective structures for thermal management. Indeed, the typical optical response of a DBR is reported in **Figure 1.2**, as reflectance (R, ratio of light intensity reflected and incident on the DBR, red line) and transmittance (T, ratio of light intensity transmitted and incident on the DBR, blue line). The parameters of the DBR are $n_H \cong 1.58, d_H \cong 85\,nm$, $n_L \cong 1.34, n_L \cong 493\,nm$ and a total of 60 BLs. As the structure is not absorbing R + T = 1 for all wavelengths for energy conservation, hence the perfect correspondence between the two spectra. The bandgaps are apparent and intense, showing $R \cong 100$ %. This is more than what is achievable with a metallic mirror with its intrinsic losses; indeed, DBRs are often called dielectric mirrors and used for photonic applications. Between bandgaps, a low-reflection oscillating background due to Fabry-Pérot interference arising from the optical cavity formed by the first and last interfaces is observed.[4] These interference fringes have a periodicity determined by the total thickness of the DBR and its effective refractive index.[7] This structure is already an example of an effective shield for NIR radiation, highly reflective at 800 and 1600 nm, whereas almost transparent to Vis light, reflecting only in the green-cyan region (540 nm).

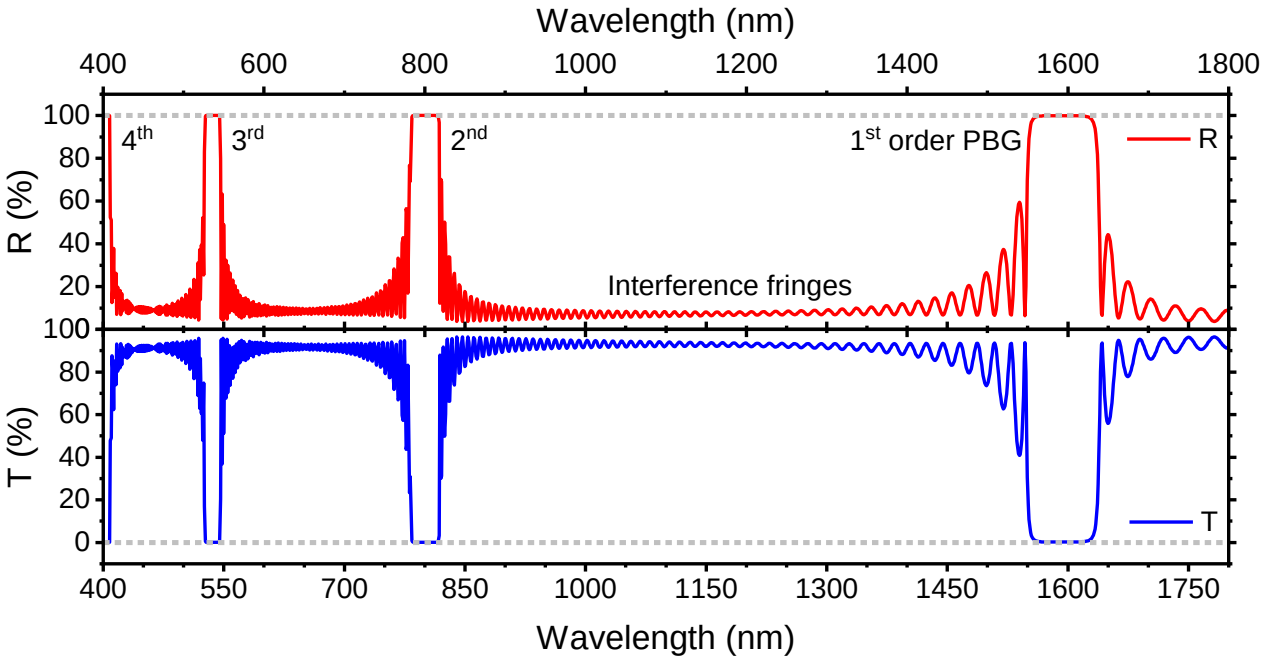

Figure 1.2. *Calculated reflectance (red line) and transmittance (blue line) of a 60-layer DBR made of polystyrene* $n_H \cong 1.58$ *and Aquivion®* ($n_L \cong 1.34$).

The sum of optical thicknesses, that is the periodicity of refractive index modulation, gives the spectral position of the peaks, as stated by **Equation 1.2**. However, the ratio between $n_H d_H$ and $n_L d_L$ has important consequences on the overall optical response of DBRs. **Figure 1.3** shows as contour plot the reflectance spectra of DBRs with the same optical thickness of the repeating BL, but different

ratios between its two components. The spectra re reported with respect to energy, expressed in multiples of the energy where the first-order bandgap is found ($E_{bandgap}$). Each spectrum makes up a row of the contour plot, with the reflectance intensity yielded by the color as per the color scale. Ideal photonic crystals are represented by the middle point, where $n_H d_H = n_L d_L = \frac{\lambda_1}{4}$; in that condition, called "lambda fourth", the width of the first-order bandgap is maximum, whereas the even-order bandgaps are completely suppressed. For each mth order, there are $m - 1$ ratios to make that order disappear and, in general, ratio affect the relative intensity and width between the various orders.

The ratio can be either beneficial or detrimental depending on the goal; for example, to achieve maximum reflection in a broad wavelength interval the lambda fourth condition is best (for example, when making a stopband optical filter). On the other hand, if greater thicknesses of one material are required, the structure may be purposedly built out of lambda fourth, for example for sensors.[5, 8] Additionally – as it will be presented in **Chapter 1** – tuning the thickness ratio allows to selectively remove from the spectrum a selected bandgap (or all the even ones for lambda fourth condition), allowing transparency in broad regions such as the Vis range.

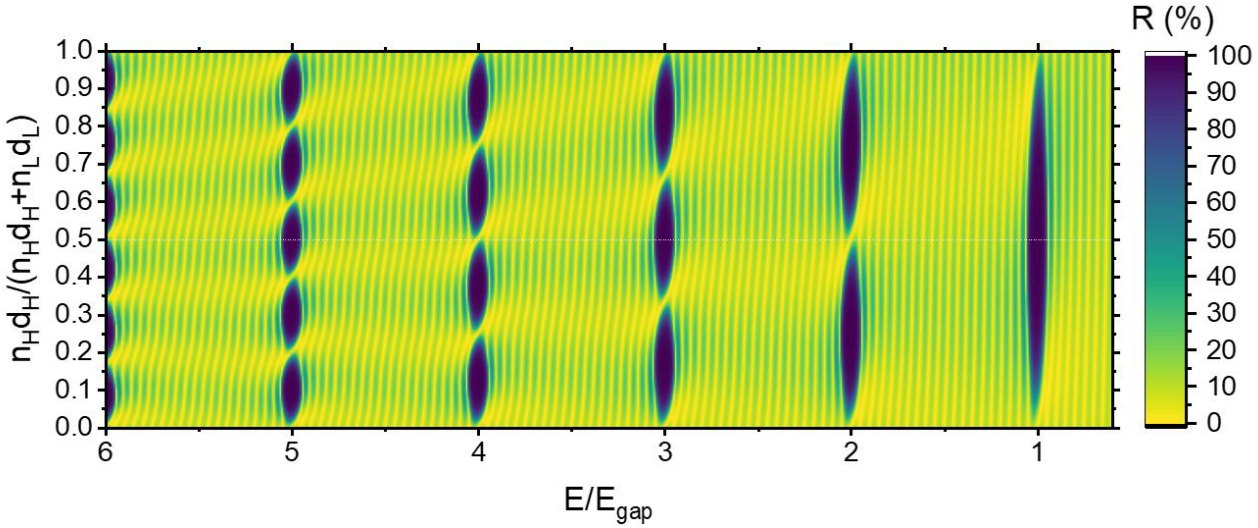

Figure 1.3. *Calculated reflectance of a 20-BLs DBR $n_H \cong 1.67$, $n_L \cong 1.47$ for variable ratio between the optical thicknesses of the constituting layer. On the x-axis, the energy expressed as multiple of the first-order bandgap energy. The white line identifies lambda fourth condition.*

1.1. Effect of dielectric contrast. Dielectric contrast is the difference in refractive index between a DBRs' building blocks, and it is a crucial parameter determining its optical response. Intuitively, since the whole optical response of a DBR depends on reflections at interfaces, which are greater the greater the dielectric contrast (due to the behavior of Fresnel's coefficients, see **Appendix A.1**), this parameter will enhance the reflectance. Indeed, **Figure 1.4** represents the variation of optical response of a DBR when the dielectric contrast is increased, as a contour plot. The bandgap appears as an intense reflectance plateau, its width increasing together with dielectric contrast, whereas the

interference fringes occupy the background with their oscillating pattern alternating high and low intensity. Note that the thickness of the materials is changed with dielectric contrast accordingly to Bragg-Snell law to keep the bandgaps in the same spectral position.[9]

The effect is apparent; increasing the dielectric contrast enhances the intensity of bandgaps as well as having a strong effect on their width. This is the reason why historically DBRs have been fabricated out of inorganic materials, especially metal oxides such as SiO_2, HfO_2, TiO_2 and many others. The red line, indeed, marks the spot corresponding to a typical dielectric contrast achievable with such materials; the width of the bandgap is around 0.4. The latter is essentially double the maximum value achievable with polymers, as seen by comparing the section corresponding to the white line, with a bandgap width around 0.2.[2, 9, 10] Therefore, a greater dielectric contrast is beneficial when the goal is reflecting as much light as possible – this will become clear in **Chapter 3**, where I explored the effect of different polymer pairs on DBRs performances in thermal management.

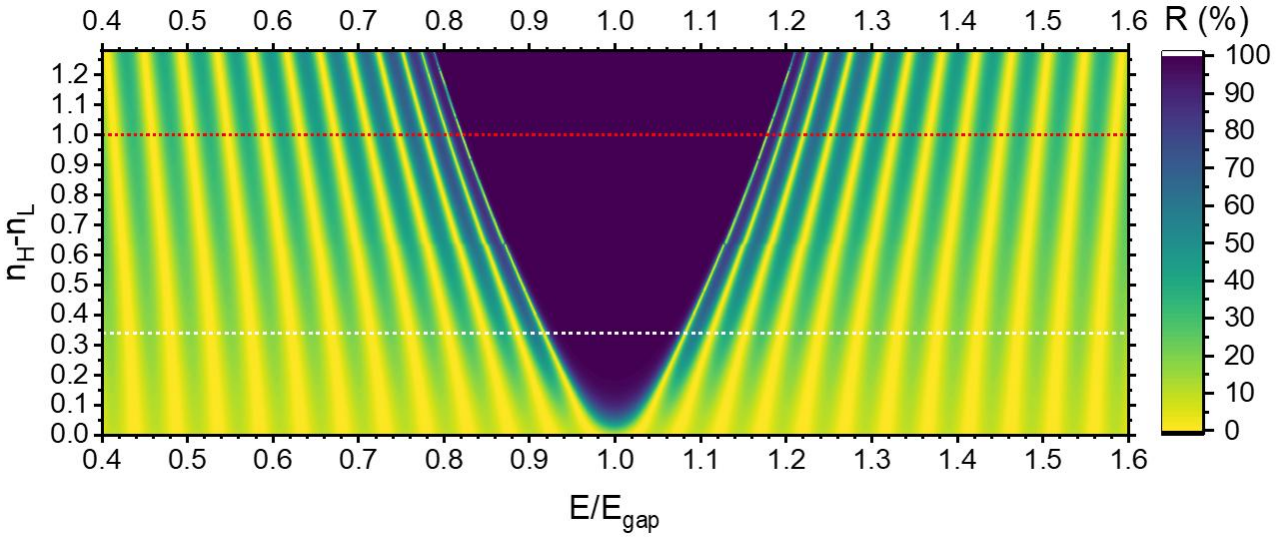

Figure 1.4. *Calculated reflectance of a 20-BLs DBR for variable dielectric contrast. On the x-axis, the energy expressed as multiple of the first-order bandgap energy. The white line marks the highest dielectric contrast attainable with commercial polymers (0.34), the red line a value obtainable using metal oxides (1).*

1.2. Effect of the number of layers. The intensity of the bandgap in a DBR is positively influenced by the number of layers; in **Figure 1.5** reports the reflectance of DBRs with progressively higher number BLs, with total layer count odd (**a**) or even (**b**). The odd-numbered DBRs show a higher reflectance intensity in the bandgap region, especially for a low number of layers, since the even-numbered ones show less intense bandgap due to the presence of an interference fringe in the middle. In both cases the reflectance peak becomes more intense and squarer as the number of layers increases. This can be exploited to circumvent the limitation due to the reduced dielectric contrast in

polymer structures. Simply, a higher number of layers is required to achieve the same reflectance values, which most of the time is not an issue due to the possibility of processing many more layers easily with polymer structures. However, the main problem remains the width of the bandgap; the only way to attain broad reflectance regions with low dielectric contrast is the fabrication of multilayer photonic structures more complex than standard DBRs.[2]

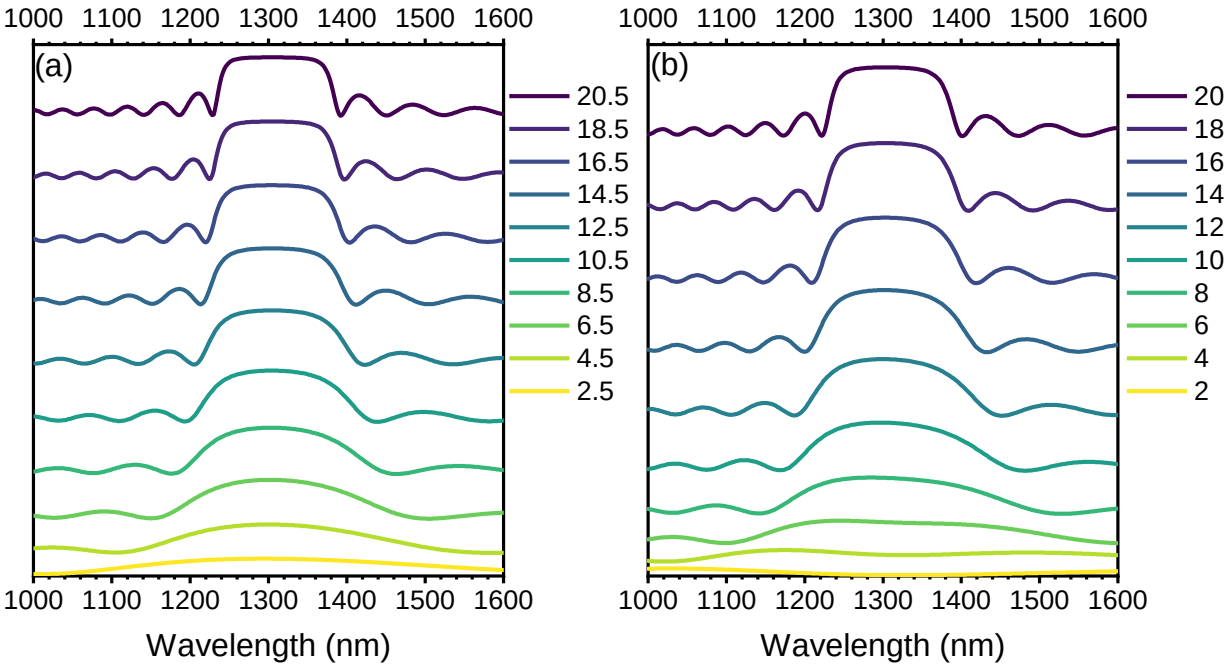

Figure 1.5. *Calculated reflectance of a DBR ($n_H \cong 1.67$, $n_L \cong 1.47$) with an increasing number of BLs. Each spectrum is labeled with its corresponding number of BLs; the .5 means the structure is symmetric, with an odd number of total layers.*

1.3. More complex structures – Broadening the bandgap. To make DBRs with broad bandgaps, there are different methods that can be exploited, borrowing ideas from the fabrication of inorganic optical filters. For inorganic materials, usually chirped mirrors are used to achieve broadband reflectance; these are represented schematically in **Figure 1.6a**. They are DBRs where the optical thickness of the layers changes progressively from a value $\frac{\lambda_1}{4}$ to $\frac{\lambda_2}{4}$. This way (with proper dielectric contrast $n_H - n_L$ and an adequate number of layers) a reflectance spectrum with a bandgap extending from λ_1 to λ_2 can be obtained.

Due to the lower dielectric contrast offered by polymers and the requirements of my research, I tweaked this idea working with slightly different structures, as reported in **Chapter 2.** These will be referred to as tandem DBRs or superperiodic DBRs respectively. Tandem DBRs, represented in **Figure 1.6b**, are essentially full-fledged DBRs placed one on top of the other. This allows to have a

structure showing multiple bandgaps, that can be either merged or separated. The reflectance spectra reported in **Figure 1.6d** corresponds to a tandem of two DBRs, with well-distanced bandgaps. Superperiodic DBRs are a different take on chirped mirrors; instead of having the thickness varying progressively from a λ_1 to λ_2, it oscillates from one value to the other back and forth multiple times – one for each superperiod making up the structure. The schematic of a structure with three superperiods is represented in **Figure 1.6c**, whereas the typical optical response of a superperiodic structure is represented in **Figure 1.6e**. The formation of an oscillating, high-reflectance region is apparent. The bandgap region extend between the λ_1, λ_2 values corresponding to the extremes of the single superperiod.[11]

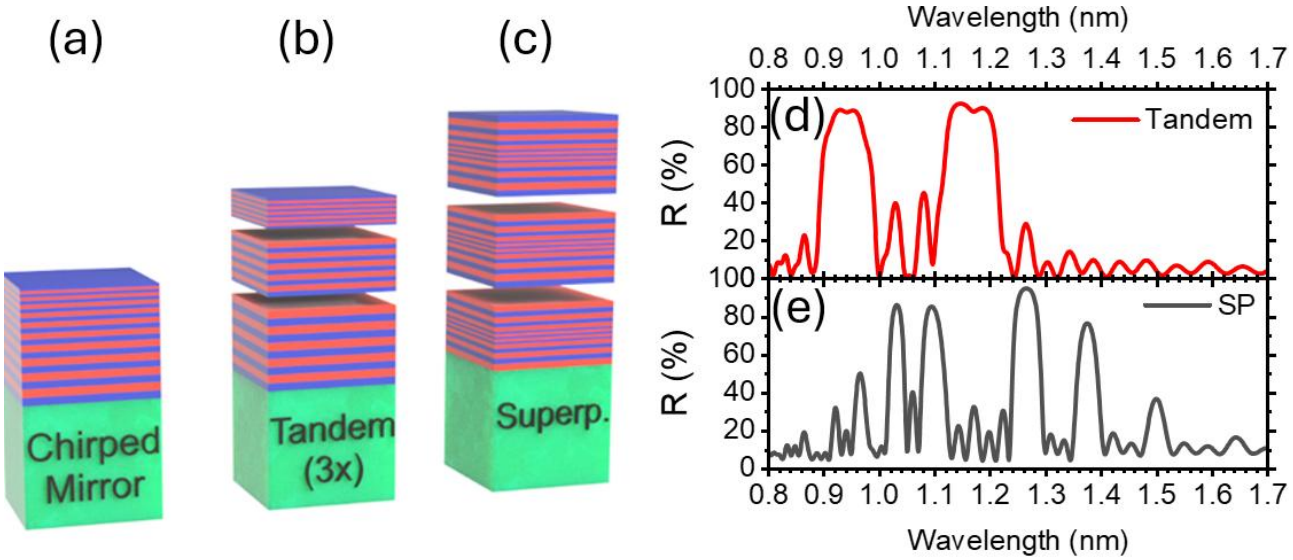

Figure 1.6. *Schematic, not in scale structures of **a)** a chirped mirror, **b)** a three-DBR tandem DBR, **c)** three superperiods of a superperiodic DBR. Gaps are only for visualization, substrate is 1 mm glass. **d)** reflectance spectrum of a 2x Tandem DBR; **e)** reflectance spectrum of a 3 superperiods superperiodic DBR.*

1.4. Angular dependency. Due to the angular dependence term in **Equation 1.1**, increasing the incidence angle θ_{ext} reduces the term under the square root, as the angle of incidence increases, the peak wavelength decreases, shifting the peaks towards the blue, towards shorter wavelengths. **Figure 1.7** represents the reflectance of a single DBR, for incidence angle between 0° and 90° (y axis) with respect to wavelength (x axis). the intensity of reflectance is shown as per the color bar, with darker tones meaning higher values.[1, 7]

The graphs show that beyond 15°, the behavior differs for p-polarized and s-polarized light. Specifically, for s-polarization, there is a gradual decrease in the transmission background, which becomes more pronounced as the angle approaches the total reflection value of 90°, while the overall structure remains more or less intact, with the stop bands still recognizable, slightly widening together with fringes that behave similarly. For p-polarization instead both the main peak and the fringes tend

to narrow and disappear, thus increasing the background transmittance, until a point around 65-70°, where the transmittance approaches 100% across the entire spectrum except in the stop bands, which are more than halved in width, where transmittance remains between 50% and 30%. After this point, transmittance decreases again in correspondence with fringes and stop bands, eventually collapsing sharply overall between 80° and 90°.

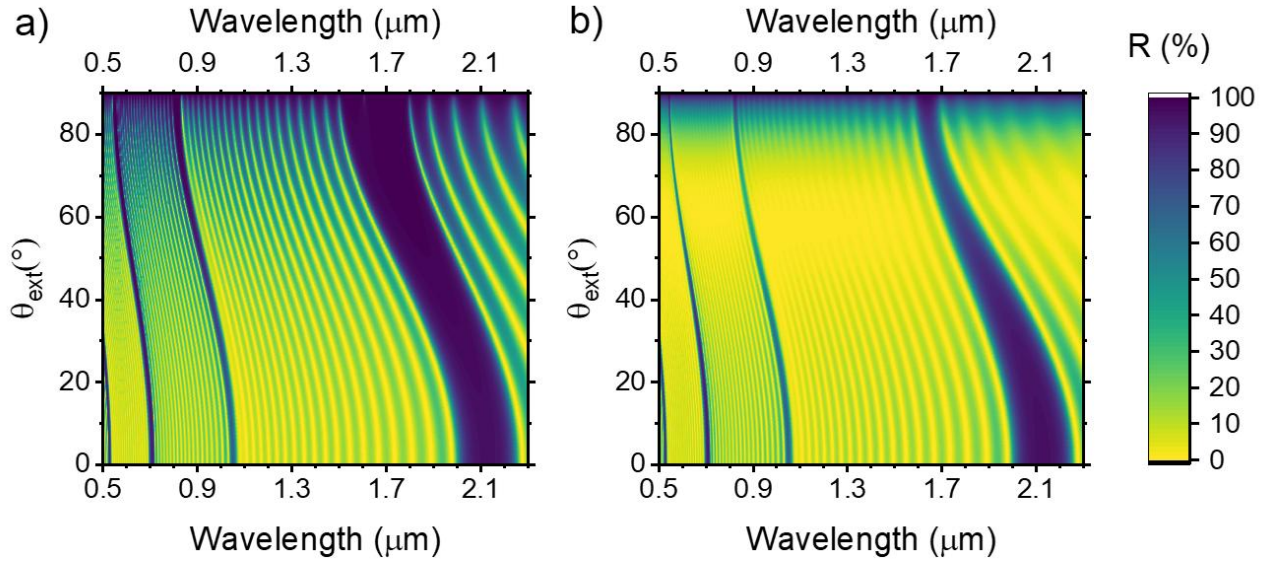

Figure 1.7. *Calculated transmission spectrum of a DBR with n_1=1.68, n_2=1.47, d_1=285 nm, d_2=375 nm, 20.5 BLs, varying the angle of incidence for polarizations* **a)** *parallel and* **b)** *perpendicular to the plane of incidence.*

This reflects the well-known behavior of Fresnel's coefficients, reported in **Appendix A.1** and specifically in **Equations A.1.1-A.1.4** and **Figure A.1.1**.[4, 7] Indeed, as the angle increases, reflectance monotonically increases for the coefficient for s-polarized light. The same does the overall reflectance of the bandgaps. The coefficient for p-polarization, instead, decreases slightly until reaching a point of zero reflectance, after which it starts to rise again. The point of zero reflectance is known as Brewster's angle; it is the same angle where the width of the bandgaps is minimum, and its intensity mostly suppressed. The effect of the angular dependency of the optical response on the thermal management performances will be investigated at the end of **Chapter 3**.

1.5. The Transfer Matrix Method. A large part of my thesis was dedicated to the numerical implementation of a method to calculate the optical response of multilayer structures, such as all those reported until now in this chapter. Indeed, even though there are formulas to predict the bandgap spectral position, and some approximate formulas to get the bandgaps width and intensity, no

analytical expression exists for the overall reflectance/transmittance of a DBR. Therefore, the main way of obtaining the spectrum is the transfer matrix method (TMM).[1, 3, 4]

TMM is not conceptually difficult, but the algebra is relatively cumbersome – I describe it in-depth in **Appendix A.2** for the bravest readers. Very briefly, the method assigns a specific matrix calculated from the Fresnel's coefficients to each interface of the DBR (interface matrices). It then assigns a matrix symbolizing the propagation through each layer (propagation matrices). Multiplying all these matrices in the proper order allows to calculate the electric/magnetic fields across the whole structure, thus knowing the final values of reflectivity and transmissivity relative to the DBR. Technically the method is analytical, but if the structure is not regular enough for drastic simplification (not in lambda fourth or with nonconstant refractive indices) the equations quickly spiral out of control. Therefore, the best approach is usually a numeric calculation performed through an adequate code on a computer.[1, 3, 4]

I used the TMM to calculate all the spectra presented in this chapter, considering the presence of an incoherent glass substrate. Indeed, I implemented the method both on *MatLab* and *Python* to be able to model effectively the optical response of all structures. This was essential in the design of the structures throughout my doctorate; it greatly helped to start with a design rationale, as described in **Chapter 1**, and to thoroughly improve it, as described in **Chapter 2**. The codes were used to provide design and post-fabrication characterization as well. Indeed, studying the reflectance and transmittance spectra of a DBR is the most reliable method for its characterization. From that, the calculated spectra can be fitted to the measured ones to obtain information about the thickness of the layers, very difficult to obtain otherwise for polymer structures, as demonstrated in the next chapter. Additionally, the information obtained through this kind of modeling greatly helps in tweaking the various parameters during the fabrication process, saving large amounts of time and effort. I will not report the codes directly in this Thesis. However, to put in perspective the large use that has been made of them during this years, numerical modeling was used in most of the work I either authored or co-authored: Megahd et al. *Adv. Opt. Mater.* **2021,** 9, 5, 2002006;[5] Lanfranchi et al. *ACS Appl. Mater. Interfaces* **2022**, 14, 12, 14550;[11] Megahd et al. *Mater. Chem. Frontiers* **2022**, 6, 17, 2413 [12] Megahd et al. *ACS Omega* **2022**, **7**, 18, 15499 [13] Lanfranchi et al. *Chem. Eng. Sci.* **2024**,[14] Benvenuti et al. *J. Mater. Chem. C.* **2024**, 12, 12, 4243 [15] Martusciello et al. *ACS Appl. Mater. Interfaces* **2024**, 283, 5, 119377 [16] Magnasco et al. *ACS Omega* **2024,** 9, 41, 42375.[17]

The TMM method will be essential to provide characterization of the structures and justification to the results of thermal experiments reported in the main subject of the next chapters, where I will present the foundation of my work over aegises, as we named DBRs engineered to reflect Near-Infrared radiation and reduce the heating of irradiated samples.

Bibliography

1. B. E. A. Saleh , M. C. Teich, *Fundamentals of Photonics.* John Wiley & Sons, **2019**

2. P. Lova, G. Manfredi , D. Comoretto. *Adv. Opt. Mater.*, **6**, 24, 1800730, (**2018**)

3. H. A. Macleod, *Thin-Film Optical Filters, 5th Edition.* CRC Press, Boca Raton, FL (USA), **2017**

4. G. Giusfredi, *Manuale di Ottica.* Springer, Rome (IT), **2015**

5. H. Megahd, C. Oldani, S. Radice, A. Lanfranchi, M. Patrini, P. Lova , D. Comoretto. *Adv. Opt. Mater.*, **9**, 5, 2002006, (**2021**)

6. P. Lova, M. Olivieri, A. Surace, G. Topcu, M. Emirdag-Eanes, M. M. Demir , D. Comoretto, *Crystals*, 10, **2020**

7. E. Hecht, *Optics, 5th Edition.* Addison-Wesley, London (UK), **2017**

8. P. Lova, C. Bastianini, P. Giusto, M. Patrini, P. Rizzo, G. Guerra, M. Iodice, C. Soci , D. Comoretto. *ACS Appl. Mater. Interfaces*, **8**, 46, 31941, (**2016**)

9. P. Lova, H. Megahd, P. Stagnaro, M. Alloisio, M. Patrini , D. Comoretto, *Appl. Sci.*, 10, **2020**

10. H. Megahd, D. Comoretto , P. Lova. *Opt. Mater. X*, **13**, 100130, (**2022**)

11. A. Lanfranchi, H. Megahd, P. Lova , D. Comoretto. *ACS Appl. Mater. Interfaces*, **14**, 12, 14550, (**2022**)

12. H. Megahd, P. Lova, S. Sardar, C. D'Andrea, A. Lanfranchi, B. Koszarna, M. Patrini, D. T. Gryko , D. Comoretto. *ACS Omega*, **7**, 18, 15499, (**2022**)

13. H. Megahd, M. Villarreal Brito, A. Lanfranchi, P. Stagnaro, P. Lova , D. Comoretto. *Materials Chemistry Frontiers*, **6**, 17, 2413, (**2022**)

14. A. Lanfranchi, H. Megahd, P. Lova , D. Comoretto. *Chem. Eng. Sci.*, **283**, 5, 119377, (**2024**)

15. E. Benvenuti, A. Lanfranchi, S. Moschetto, M. Natali, M. Angelini, P. Lova, F. Prescimone, V. Ragona, D. Comoretto, M. Prosa, M. Bolognesi , S. Toffanin. *J. Mater. Chem. C*, **12**, 12, 4243, (**2024**)

16. M. Martusciello, A. Lanfranchi, M. Castellano, M. Patrini, P. Lova , D. Comoretto. *ACS Appl. Mater. Interfaces*, **16**, 38, 51384, (**2024**)

17. L. Magnasco, A. Lanfranchi, M. Martusciello, H. Megahd, G. Manfredi, P. Lova, B. Koszarna, D. T. Gryko , D. Comoretto. *ACS Omega*, **9**, 41, 42375, (**2024**)

Chapter 2 – Aegises for Thermal Management

This chapter is partially published as Lanfranchi et al.,
ACS Applied Materials & Interfaces **2022,** 14**, 14550**[1]

Abstract

The looming ghost of climate change is ever pushing the developed world to the principles of sustainability and energy efficiency. In this regard, air conditioning systems are an essential mean in a warming climate, as well as a problem due to their high energy consumption and the tendency to worsen the urban heat island phenomenon. I investigated a passive method able to reduce the internal heating of screened objects – thermal shielding. I designed and fabricated aegises, multilayer dielectric mirrors able to reflect light in the near-infrared range while maintaining transparency in the visible range. Near-infrared light amounts to half the total energy of sunlight and is efficiently absorbed by bodies thanks to the vibrational overtones and combination bands of their moieties. The aegises were designed to reflect near-infrared light in correspondence to the principal absorption peaks of selected test materials, namely water and paraffine – chosen to emulate ubiquitous moieties such as O-H and C-H, present respectively in water/ambient humidity and polymer/organic materials. The aegises were fabricated via solution processing (spin-coating) using poly(acrylic acid), cellulose acetate and poly (*N*-vinylcarbazole). Samples were thoroughly characterized and their optical response calculated with the suitable model, obtaining a good agreement. Different structures were investigated, namely single distributed Bragg reflectors, tandem aegises, and superperiodic ones. All the structures were subjected to thermal experiments to assess their performances in thermal shielding; while screening representative test materials (water and paraffine), I obtained efficiencies in temperature increase reduction as large as 20 %, rising to more than 50 % with reduced bandwidth of incident radiation. The results were correlated with the aegises' efficacy in shielding absorption peaks – spectral coverage, yielding promising results in the thermal shielding field.

2.1 Introduction

Global warming is becoming increasingly worrying as extreme weather events become more frequent and natural ecosystems undergo changes that reduce biodiversity.[2, 3] To combat this escalating crisis and keep the global temperature rise within tolerable limits, the international community is now prioritizing carbon neutrality by drastically reducing CO_2 emissions until net zero is reached.[4, 5] In this context, passive methods to improve energy efficiency and energy conservation are gaining attention worldwide. However, they are especially important for developing countries, which face greater challenges in reducing emissions as they often rely on cheap, high carbon emission sources of energy such as coal.[6, 7] Many of these countries, such as India and Brazil, are located in tropical and equatorial regions where the increasing use of air conditioning is a major challenge as living standards rise. For example, a study from Akpinar-Ferrand & Singh foresee an increase in India's CO_2 emissions of 25 % in the best-case scenario with a steady reduction of population growth (**Figure 2.1a**, green curve; worst-case scenario is the orange curve) only due to the penetration of air conditioning in the market.[8] Although air conditioning systems provide cooling, they are highly unsustainable and inefficient as they consume energy to lower indoor temperatures and at the same time emit heat outside, contributing to the urban heat island effect.[9, 10] This creates a feedback loop in which rising temperatures in cities increase the demand for air conditioning, which in turn exacerbates the problem.[9] Similar challenges arise in the transportation sector, where air conditioning not only consumes additional energy but also increases CO_2 emissions and heat dissipated in the environment.[11] Aside from the direct impact on energy consumption, this vicious cycle also has broader implications for urban efficiency. Cities are becoming less efficient because many processes rely on Carnot engines, whose efficiency decreases as the ambient temperature rises. As global and urban temperatures rise, the efficiency of these processes will continue to decline. [1] All these problems are already well known in highly developed equatorial countries such as Singapore, which is actively seeking alternative cooling strategies.[12]

One promising approach to solving this problem is radiative cooling, a technique that makes use of materials designed to emit thermal radiation in the range of atmospheric transparency (8-13 μm), allowing heat to escape into the cold of space.[13] However, radiative cooling requires not only a powerful radiator, but also an efficient mirror that reflects the sunlight and prevents further heating.[14] Reflecting sunlight to reduce heat build-up is therefore a fundamental aspect of this method, which is also valuable in its own right. Current commercial approaches to reflecting sunlight, such as adding

[1] I acknowledge Prof. Ioannis Papakonstantinou from King's College (London, UK), who I met at European Optical Society's 2024 meeting, for this fascinating observation.

highly reflective or scattering particles to paints, have proven successful. For example, TiO_2 particles in white paints can reflect up to 85% of sunlight, providing significant thermal protection.[15] However, this solution is not suitable where transparent surfaces are required, such as for windows of buildings and transportation means.

The need for transparent materials that can shield heat while allowing visible light to pass through is also important in other industries such as food & beverage. In this case, excessive heat can cause plastic containers to release substances into their contents, affecting the quality of the products and potentially leading to microbial growth.[16] Greenhouse crops also face the problem of overheating, particularly in summer when greenhouse temperatures can exceed acceptable limits for plants. Passive solutions such as spraying water and evaporating it, increasing airflow or using gray tinted films are commonplace in open greenhouses.[17-19] However, these methods are either unsustainable or reduce crop yields as they also block part of the fundamental visible (Vis) light. A smarter approach would be to selectively filter out near-infrared (NIR) light, reducing heat without affecting plant growth.[20] Of course, blocking NIR light while maintaining transparency would also be beneficial for transparent windows in buildings and vehicles, as well as for transparent packaging.

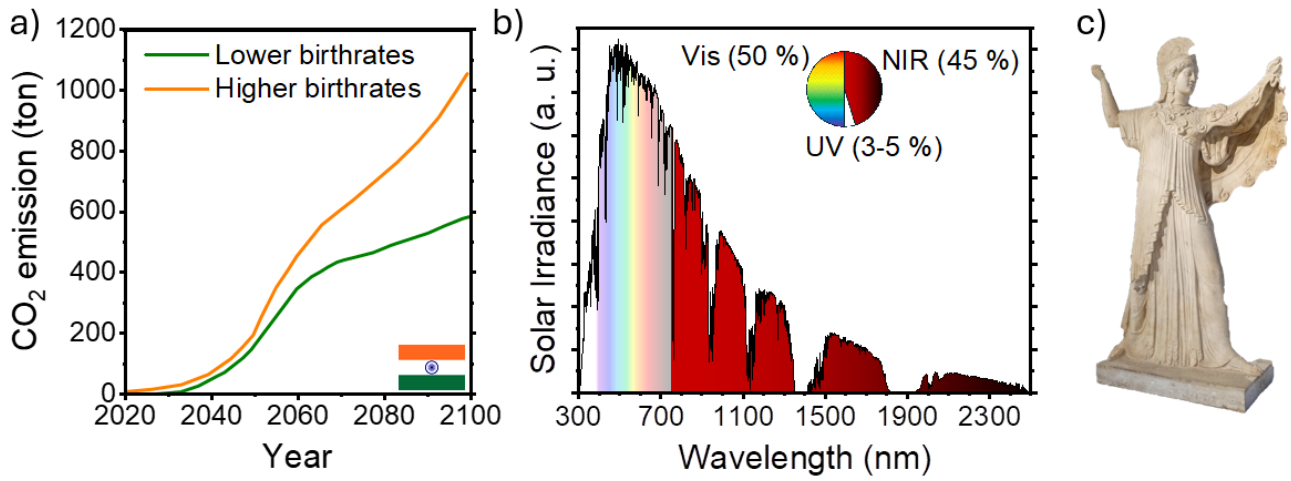

Figure 2.1. **a)** *Projected increase in CO2 emissions in India due to the penetration in the market of air-conditioning plants (orange curve: higher population growth, green curve: lower population growth);*[8] **b)** *solar spectrum AM 2.5 G;*[21] **c)** *Roman statue of the goddess Athena (Naples National Archeological Museum).*

Indeed, the integration of the solar spectrum near the ground (AM 2.5 G, black line in **Figure 2.1b**) shows that almost 50% of the energy comes from the Vis range, but the NIR still makes up a significant proportion of the total energy at around 45 % (on the other hand, UV light accounts for 5 % of the total at most).[21] Additionally, although NIR radiation is invisible to the human eye, it is efficiently absorbed by many materials including white or transparent ones such as water and

polymers leading to heat build-up. Therefore, reflecting NIR light could reduce heating without compromising transparency.

In response to this challenge, my work has focused on the development of all-polymer screens that reflect NIR light while remaining transparent in the Vis region. Various methods have been proposed and reported in literature for NIR reflection, including liquid crystals,[22] delignified wood,[23] and assemblies of nano/microstructures.[24] While many of these methods are effective, they often either lack selectivity for different wavelengths or scalability. Considering the latter requirement, I have investigated the use of distributed Bragg reflectors (DBRs) for selective NIR reflection. Due to the tunability of their optical response in terms of reflectance and transmittance – thoroughly described in **Chapter 1** – they are perfect candidates to fabricate thermal shields reflecting NIR radiation in correspondence to selected wavelengths while remaining transparent or partially transparent to Vis one.

Similar approaches were explored in earlier studies, such as by Nakamura et al. who achieved good thermal shielding by combining polymers with inorganic particles.[25] Radice et al. instead developed all-polymer NIR-reflective DBRs using expensive, difficult-to-process fluoropolymers to produce high dielectric contrast and broad, intense bandgaps.[26] They demonstrated that these DBRs can reduce temperature rise by up to 12% when used as thermal shielding. My research was built on these findings, using less expensive and easier to process polymers; although the latter have a lower dielectric contrast than those used by Radice, I have compensated for this by designing more complex structures allowing for greater reflection, such as tandem and superperiodic ones (see **Chapter 1**, **Subsection 1.3**). Additionally, I carefully matched the DBRs reflectance spectra to the absorption peaks of shielded materials, thus considering the spectral coverage that each DBR could provide to a certain test material.

These DBRs were tested for thermal shielding in water and paraffin and achieved record efficiency values. We refer to these DBRs used as thermal shields with the name "*aegises*", inspired by the protective, lightweight goatskin of the goddess Athena, like that worn on the shoulder by the statue reported in **Figure 2.1c** (*Museo Archeologico Nazionale di Napoli*, photo taken by me). Like the Aegis, these shields are thin, flexible and modest, but provide excellent protection against radiant heat.[27]

1.1.1. Aegises' Fabrication Methods – Coextrusion. There is an industrial approach that allows for the fabrication of photonic structures over large areas, that is called coextrusion (**Figure 2.2a**).[28] This method implies the simultaneous extrusion of two different polymer films which are then hot-rolled one on top of the other to halve the total thickness. The two-layers foil is than cut in half through

its length, the two halves hot rolled again one on top of the other; this is repeated for N total times, obtaining a film formed by 2^N layers. However, this method is not viable for laboratory scale, due to the high cost of the equipment and the amount of materials used for each run. Hence, on laboratory scale DBRs are fabricated through solution-processing methods, such as slot die-, dip- or spin-coating. A section of chapter 6 will be dedicated to the use of dip-coating methods; however, the state-of-the-art technique for the fabrication of polymer DBRs is spin-coating.[29]

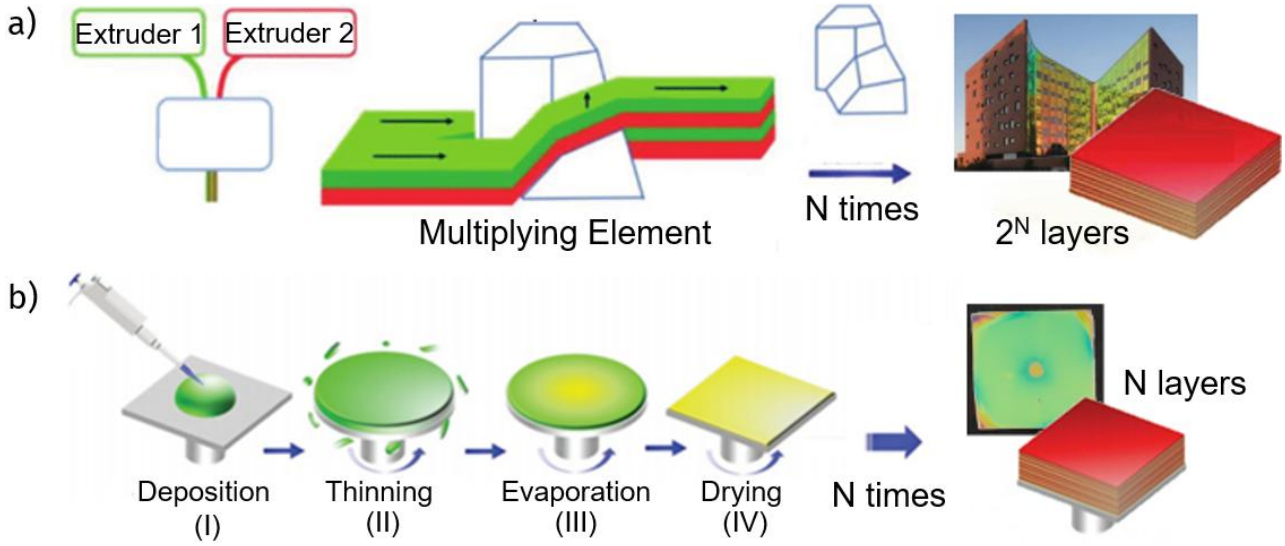

Figure 2.2. a) *Schematics of the coextrusion process.* **b)** *schematics of the spin-coating process*.

1.1.2. Aegises' Fabrication Methods – Spin Coating. The spin-coating technique is represented in **Figure 2.2b**.[29] A controlled volume of a polymer solution is deposited on a substrate which in our case (dynamic spin-coating) is rotating at a fixed speed. The centrifugal forces act on the liquid as soon as it touches the center of the substrate, making it spread in all radial directions simultaneously. Most of the solution is thrown off the substrate, but if the wettability of it with respect to the coating solution is enough, a thin film of solution will be retained. Upon evaporation of the solvent, the layer solidifies and dries, forming a thin film of the polymer. In some cases, a thermal annealing can be exploited to prevent problems such as percolation of solvents in the layer. When the film is ready, the process is repeated with a second polymer solution; then again with the first one, and so on and so forth. After N steps, an N-layer DBR is formed. The thickness of the layer deposited via the spin-coating technique can be extrapolated using different models. For example, Meyerhofer proposed that early in the spin coating process, the physical flow of solution getting thrown off the substrate dominates the thinning process of the film (I). On the other hand, later in the process, thinning is mainly due to evaporation (III). Hence, Meyerhofer found that the film thickness can be predicted analytically as long as the transition from flow-induced dilution to evaporation-induced dilution occurs abruptly, provided that the film is so thin that the solvent concentration remains uniform

throughout its depth. The final thickness of a spin-coated film can also be determined without considering the evaporation rate of the solvent. This is possible if some assumptions are made, for instance the assumption that the air flow remains laminar throughout the process. This leads to the following relationship between the final thickness h_f and the rotational speed ω:

$$h_f = \left(\frac{3kC_0\eta_0}{2(1-C_0)\rho}\right)^{\frac{1}{3}} \omega^{\frac{1}{2}} \qquad \text{or} \qquad h_f \propto \sqrt{\omega} \qquad (2.1)$$

Where C_0 is the initial concentration of the solute (as volume fraction), η_0 is the viscosity of the solution and concentration C_0, and ρ is its density. It is assumed that the concentration of the solute remains at C_0 until the evaporative dilution transition begins. k is a constant specific to the coating solvent and for typical spin coating solvents equals to 10^{-7} m $s^{-1/2}$. However, despite **Equation 2.1**, the final film thickness in spin coating is not always proportional to $\sqrt{\omega}$. Indeed, the validity of this equation depends on several assumptions, and if the latter are not met, the proportionality breaks down; for example, since the evaporation rate is omitted, no influence of temperature and ambient humidity is apparent from **Equation 2.1**, whereas both parameters play a fundamental role. Nonetheless, the equation gives a useful starting point for the tuning of thicknesses and henceforth of the overall optical response of photonic structures.[30]

There are two main limitations to the fabrication process.[29] The first one is that the two polymers used must be soluble in orthogonal solvents, which means the solvent of the first solution must not dissolve the second polymer and vice versa; otherwise, each layer's deposition ruins the previous one and the photonic structure is not formed. This precludes the fabrication of DBRs using similar polymer pairs, as well as impeding the use of some polymers altogether, such as insoluble materials like polyethylene terephthalate or polytetrafluoroethylene. Additionally, the second limitation is that most polymers have a similar refractive index, being formed by relatively similar carbon chains full of hydrogen atoms. This, together with the limitation of orthogonal solvents, greatly reduces the number of materials compatible with the process. An additional obstacle to overcome is that many materials are not compatible with each other due to the low wettability of one solution with films of the other solution; for example, perfluorinated polymers such as Hyflon® do not allow for any other solution to be cast on top unless the surface is properly activated in some way, i. e. via plasma treatment.[26]

2.2 Results & Discussion

2.2.1. Materials choice. Three polymers adequate to the spin-coating process were used in this work. The first one is poly(*N*-vinylcarbazole) (PVK), whose structure formula is reported in **Figure 2.3a**. Its refractive index dispersion is reported in **Figure 2.3d** (solid black line: real part/refractive index, dotted black line: imaginary part/extinction coefficient).[31] As seen by the plot, PVK's refractive index is extremely high for polymer standards (n ~ 1.67 in the Vis, n ~ 1.63 in the NIR) and actually the highest amongst easily processable, commercial polymers. This is due to a preresonant enhancement caused by the carbazolic group's absorption of UV light, as apparent by the rapid increase in value of the extinction coefficient from 375 nm of wavelength (black dotted line). Its high solubility in a spin-coating friendly solvent such as toluene makes it the perfect choice as high-refractive index layer for aegises.

To complement PVK, polyacrylic acid (PAA, structure formula in **Figure 2.3b**) dissolved in 4-methyl-2-pentanol or cellulose acetate (CA, structure formula in **Figure 2.3c**) dissolved in 4-hydroxy-4-methyl-2-pentanone (diacetone alcohol) were used as low refractive index polymers. **Figure 2.3d** shows the dispersion of their refractive indices with wavelength. CA (red line)[29] has a much lower refractive index than PVK, ranging from 1.48 in the Vis to 1.46 in the NIR. In contrast, polyacrylic acid (blue line)[29] ranges from 1.53 to 1.51 in the NIR. Both show no absorption in the wavelength range considered. The PVK-CA pair provides a dielectric contrast that is 0.05 higher than that of PVK-PAA. However, its solution viscosity is very high at high concentrations, which makes spin-coating deposition more difficult. In addition to the manual difficulties in generating a uniform solution flow on the rotating substrate, where a systematic distance of less than one millimeter to the spin plate must be maintained without touching it, drying times are quite long (several minutes), which makes the fabrication of the structures very slow. Moreover, a 50 to 70 °C 2-minutes long thermal annealing must be performed on each PVK layer to avoid 4-hydroxy-4-methyl-2-pentanol percolation, slowing down further the fabrication process.

PAA in 4-methyl-2-pentanol is instead less viscous and its solvent faster to evaporate allowing for quicker and easier deposition. However, it produces unstable films whose thickness varies greatly depending on manufacturing conditions and ambient humidity, as they tend to absorb water, swell and crack over time. Additionally, highly concentrated PAA solutions tend to form opaque and non-uniform films. Upon these considerations, apart from two structures with a high number of layers where PAA has an edge for its quicker fabrication time, CA was used as low refractive index material.

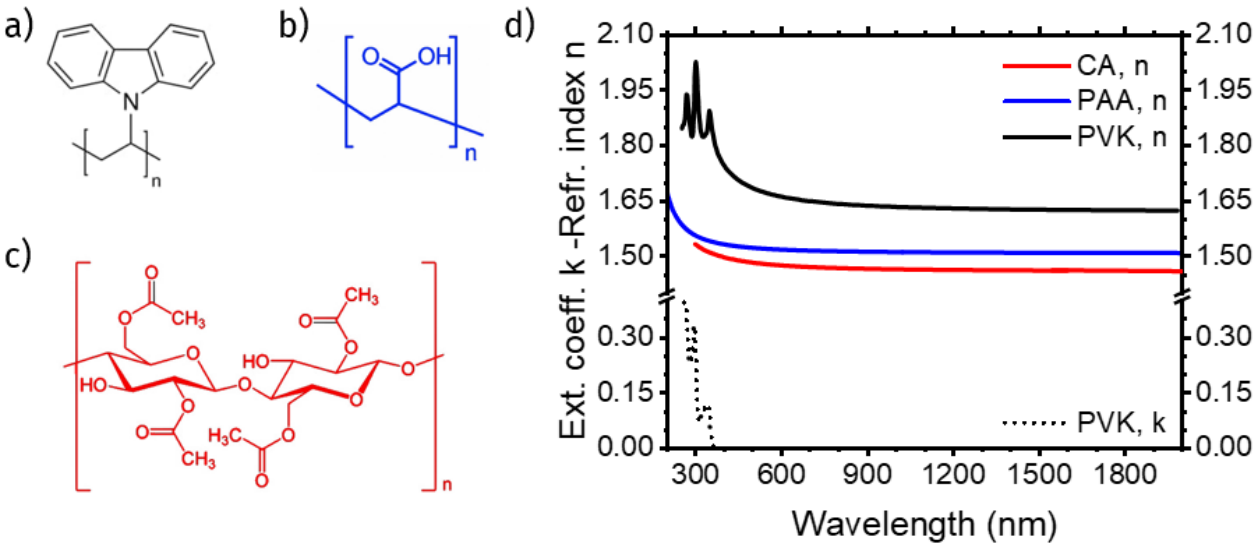

Figure 2.3. a-c) *Structure formulae of* **a)** *poly (N-vinylcarbazole),* **b)** *poly (acrylic acid),* ***c)*** *cellulose acetate;* **d)** *Refractive indexes of cellulose acetate (red line)[29] poly (acrylic acid) (blue line)[29] and poly(N-vinylcarbazole) (black line)[31]. The extinction coefficient of PVK is represented by the dotted black line.[31]*

2.2.2. Structures and design rationale. Three types of aegises were fabricated: single, tandem and superperiodic aegises. Single aegises are well-known in literature for sensing, fluorescence control, and thermal shielding applications, and are formed by repeating a single period, whereas tandem aegises are formed by stacking aegises tuned to different wavelengths one on top of the other. Superperiodic aegises, instead, are fabricated repeating three times a single superperiod, in which bilayers thickness gradually decrease and then increase again. This is a variation of the wide-bandgap inorganic structures with gradually increasing layer thickness, to compensate the lower dielectric contrast achievable with polymers. The structures were fabricated in $\frac{\lambda}{4}$ condition, with layers' optical thickness equal to one fourth of the bandgap's wavelength. In this condition, as explained in the introduction, the even diffraction orders disappear allowing for complete transparency in the visible region. The rationale for the design of structures was to consider the NIR absorption spectra of the materials to be shielded and reflect light in correspondence to the more pronounced peaks. This rationale will be greatly improved with more quantitative considerations in **Chapter 2**. Water and paraffine were used as test material, as they are representative of the usual moieties which are absorbing NIR light: CH and OH groups. These moieties are ubiquitous and present in most materials, mainly polymers, water and ambient humidity.[32] **Figure 2.4a** shows a comparison the NIR spectra of the two prototype materials to be shielded, water (violet curve) and paraffin (red curve). The spectrum of water (data from Bertie et al., *Appl. Spectr.* **1996**, 8, 1047[33]) shows remarkable peaks at 950, 1200, 1450 and 1950 nm, which are due to the overtones and combination bands of its three primary vibrational modes: symmetric O-H stretching (ν_1), H-O-H bending (ν_2) and asymmetric O-

H stretching (ν_3). The spectrum of paraffin was measured through transmittance measurements (see **Appendix B.2.1** for experimental details) reveals several peaks corresponding to the vibrational modes of the -CH, -CH_2, -CH_3 and -OH groups at 900, 1050, 1200, 1400, 1800 and 2200 nm.[34] Although the data for liquid paraffin better illustrate the absorption in the lower wavelength range, the shielding experiment was performed with solid Parafilm (green curve in **Figure 2.4a**). The solid form exhibits scattering in the shorter wavelength range, which makes it difficult to clearly resolve certain peaks but is otherwise identical to the liquid one.

2.2.3 Optical characterization. Seven different aegises were prepared to shield water and paraffin, using the design rationale described in **Section 2.2.3** via the spin-coating method described in **Section 2.1.1** (precise details in **Appendix B.2.2)**. The aegises are pictured over a *Paperino* comic background in the insets of **Figure 2.4b-h**, alongside a schematization of each structure. To provide quantitative data on their effect in thermal shielding, the aegises were optically characterized through reflection measurements. Their reflectance spectra were measured with a simple optical fiber setup (described in **Appendix B.2.3)** and are reported in **Figure 2.4b-h**. Three of them were simple aegises prepared with photonic band gaps (bandgaps) at 950 nm (AE1, **Figure 2.4b**), 1160 nm (AE2, **Figure 2.4c**) and 1430 nm (AE3, **Figure 2.4d**), respectively. AE1 and AE2 appear transparent and colorless in the visible spectrum, while AE3 has a slight yellow tint due to the partially suppressed second- and third-order bandgaps (see also its picture in the inset). These single aegises were tuned to match the corresponding absorption peaks of water and paraffin, as seen comparing the spectra with those reported in **Figure 2.4a**. In addition, two tandem aegises, consisting of double and triple mirrors, were created. The first tandem aegis (TAE1, **Figure 2.4e**) has bandgaps at 950 and 1150 nm, combining the properties of AE1 and AE2, with interference fringes between the bandgaps allowing high reflectance over an extended range. There are no second-order bandgaps, suggesting that TAE1 consists of two dielectric quarter-wave DBRs with layers of equal optical thickness. Although a third-order peak is present at 400 nm, it does not affect the transparency of TAE1 because the eye sensitivity at this wavelength is minimal, as seen by its picture in the inset. The second tandem aegis (TAE2, **Figure 2.4f**) is a triple mirror with a 200 nm wide bandgap centered at 970 nm, resulting from the overlap of the bandgaps and interference fringes of the individual DBRs. Second-order bandgaps are suppressed, while a third-order peak occurs at 380 nm in the UV range. TAE2 is designed to reflect most of the light emitted by an LED light source at 970 nm.

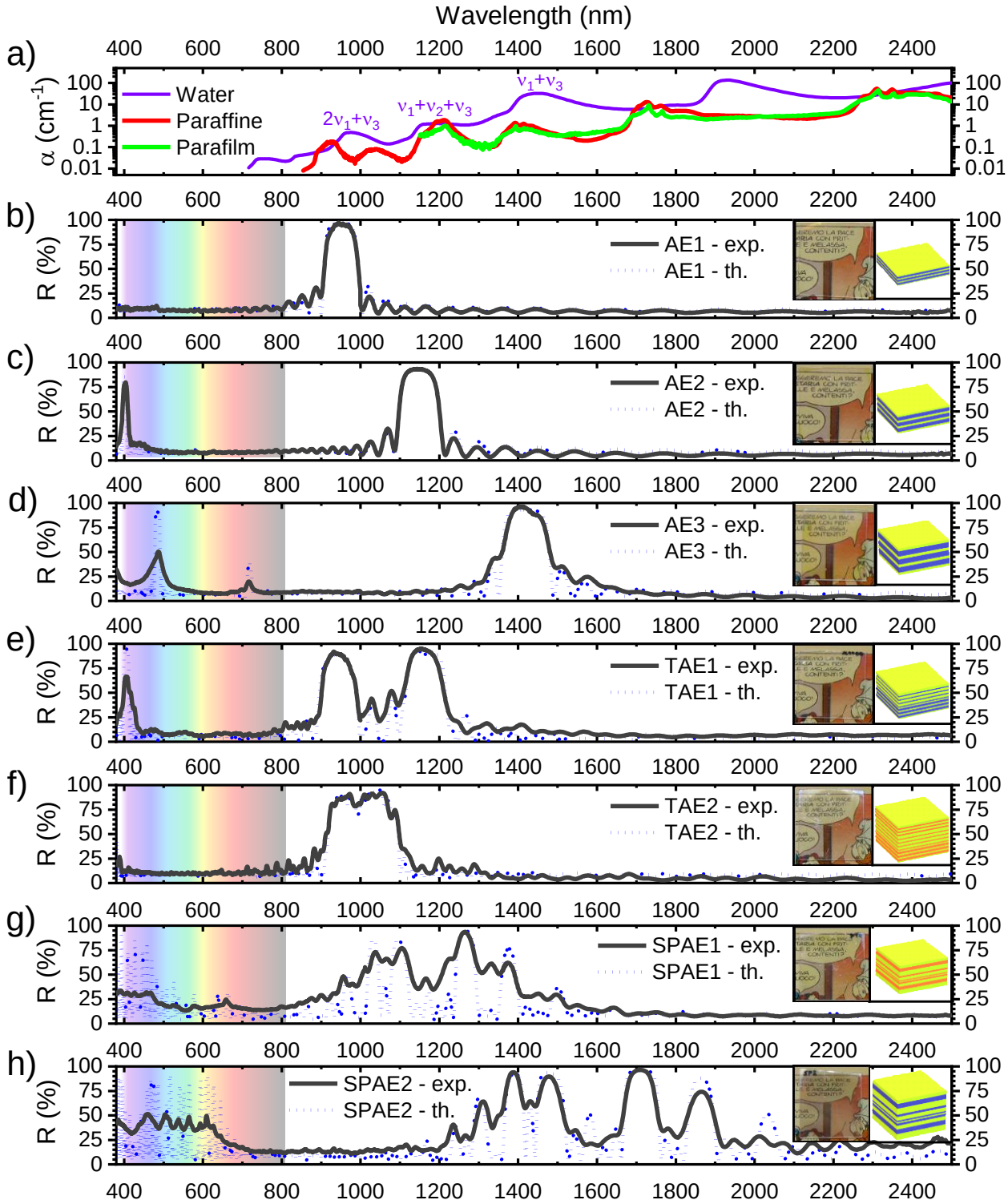

Figure 2.4. **a)** *Water (purple), paraffine (red) and Parafilm (green) absorption coefficient. Water absorption peaks due to overtones and combination bands are labeled as sum of fundamental vibrational modes (symmetric stretching ν_1, bending ν_2, and asymmetric stretching ν_3);* ***b-h)*** *Measured (black lines) and calculated (blue dotted lines) reflectance spectra of aegises* **b)** *AE1,* **c)** *AE2,* **d)** *AE3,* **e)** *TAE1,* **f)** *TAE2,* **g)** *SPAE1,* **h)** *SPAE2. In the insets, a top-view picture on a comic panel background (left) and a schematic (right) for each sample.* Adapted from [1]

Two other aegises were fabricated with superperiodic structures to exhibit multiple bandgaps. The first (SPAE1, **Figure 2.4g**) has a reflectance range between 950 and 1400 nm, with peaks at 1100 and

1300 nm and a plateau around 450 nm in the visible spectrum, making it largely colorless with an overall transmittance of about 75%. The second superperiodic aegis (SPAE2, **Figure 2.4h**) has a high-reflectance region in the near infrared (NIR) between 1250 and 1900 nm, with peaks at 1250, 1300, 1400, 1500, 1700 and 1900 nm. In the visible range, SPAE2 shows a reflection plateau in the blue - yellow region. Clearly, the aegises are able to reflect a different amount of NIR light depending on their structure; additionally, their effect will depend on how light is efficiently absorbed by the materials at wavelengths corresponding to the aegises' reflection. This will be quantified in **Subsection 2.3.2** by using a parameter named spectral coverage.

The aegises' optical responses (solid black lines in **Figure 2.4b-h**) were also modeled using transfer matrix method calculations (blue dotted lines in the same figure) to determine the most likely thicknesses of the repeating layers. The calculated spectra agree well with the measured data for all samples, especially for the major bandgaps in the NIR region. Minor deviations occur at shorter wavelengths, probably due to light scattering effects that influence the experimental results. SPAE1 shows the least experimental-theoretical agreement. This is most probably due to the use of PAA for thick layers in a very complex structure, which causes an inevitable degradation of the optical response. Overall, the agreement remains acceptable, and the thicknesses resulting from the fit of the calculated spectra to the experimental data are listed in **Table 2.1**. For SPAE1 and SPAE2, the table reports three thickness values for d_H and d_L. This means that over the 30 BLs making up each superperiod, values decrease progressively from the first value indicated to the second one, then increase again to the third one.

Table 2.1. *Calculated layer thicknesses for the aegises fabricated (d_H and d_L), their number of layers (NoL), and their calculated total thickness (TT). High refractive index layers (subscript H) are always of PVK, low refractive index ones are of CA unless otherwise noted.*

Aegis		d_H(nm)	d_L (nm)	NoL	TT (μm)
AE1		141	167	51	7.8
AE2		175	197	51	9.3
AE3		202	259	51	12.6
TAE1	(top)	140	166	40	10.8
	(bot)	178	199	41	
[a)]TAE2	(top)	144	158	40	19.8
	(mid)	154	170	40	
	(bot)	161	177	41	

[a, b] SPAE1	238 to 150 to 238	213 to 151 to 213	30×3	16.2
[b] SPAE2	323 to 221 to 323	295 to 200 to 295	30×3	22.5

[a] *Low refractive index layer is PAA instead of CA.* [b] *Layers thicknesses in each superperiodic aegis's single superperiod vary with arithmetic progression from maximum to minimum and vice versa.* Reproduced from [1]

Figure 2.5 shows angle-resolved transmittance spectra for TAE1 (panel **a**) and SPAE2 (panel **b**). The measurements were performed as per **Appendix B.2.1**. Briefly, the setup uses a fixed collimated white light beam and a rotating mount with 5° resolution to measure spectra of the sample at each angle between 0 and 70°. The light is polarized to probe the effect of the two polarizations.

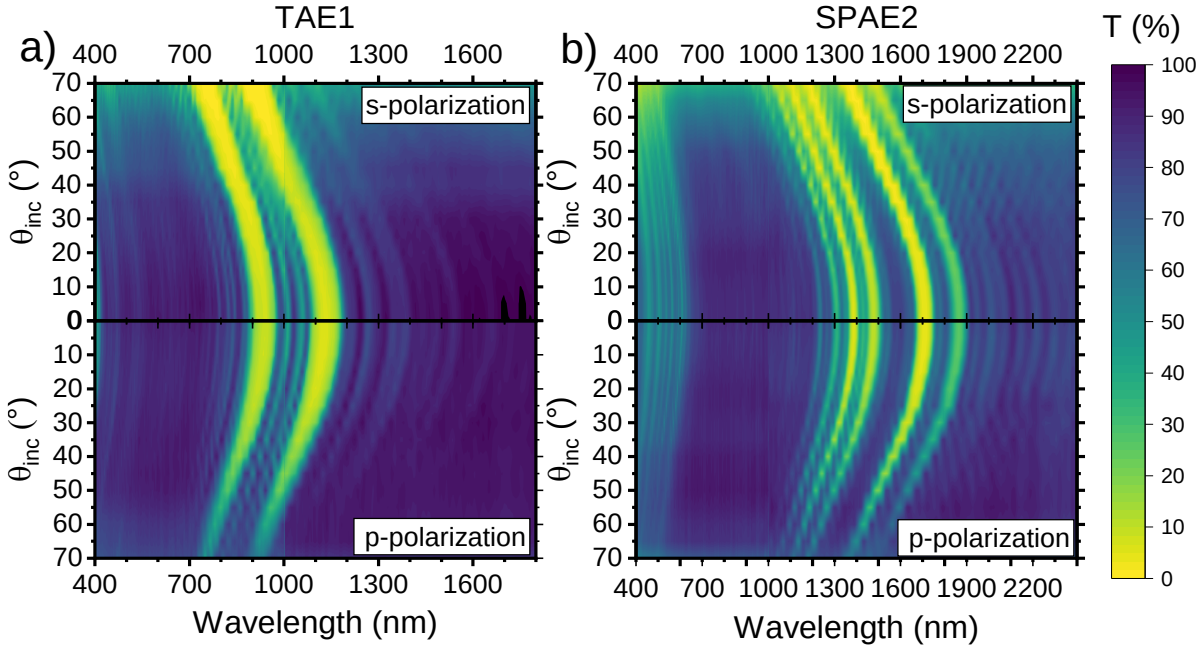

Figure 2.5. **a)** *Transmission spectra of TAE1 for angles 0-70° every 5°, in perpendicular (top) and parallel (bottom) polarization.* **b)** *Transmission spectra of SPAE2 for angles 0-70° every 5°, in perpendicular (top) and parallel (bottom) polarization.* Adapted from [1]

In **Figure 2.5a**, the upper plot shows that the bandgaps of TAE1 move to shorter wavelengths when s-polarized light is used. The behavior follows closely that reported in **Subsection 1.4**, the bandgaps widening and becoming more intense with increasing angle of incidence, while the overall transmittance is decreasing. With p-polarized light (lower diagram), the bandgaps narrow with increasing angle of incidence, whereby the transmittance increases until the Brewster angle (approximately 60°) is reached, after which the overall transmittance decreases sharply. This behavior mimics that due to Fresnel's coefficient for the single interfaces (see **Appendix A.1**), is consistent for

both TAE1 and SPAE2 across both polarizations, and it is compatible with the typical behavior of DBRs reported in **Subsection 1.4**. Angular dispersion must be considered for thermal shielding applications, as sunlight strikes surfaces at different angles throughout the day.

2.2.4. Scanning electron microscope analysis. To further verify the calculated thicknesses, we performed scanning electron microscopy (SEM) on two selected samples, TAE1 and SPAE2, as they represent the most complex structures. Both samples experienced significant delamination during preparation for SEM imaging, caused by the freeze process. I report only part of SPAE2, which consists of 20 layers, is visible in **Figure 2.6a**. Although the individual layers can be distinguished, the interfaces between them appear blurred. The PVK layers are more compact and have less visible globular structures. The layer thicknesses were estimated from this image after the contrast was enhanced (**Figure 2.6b**). However, due to the difficulties in clearly identifying the interfaces and the limited resolution of the image, a considerable margin of error remains in the measurements, which is related to the sample preparation process. This is illustrated in **Figure 2.6c**, where the measured thicknesses for each bilayer are shown as light bars, distinguishing between PVK (red) and CA (cyan). The thickness values derived from the optical modeling are also shown as faded bars in the same figure. Despite the measurement errors, the agreement is quite good, whereby the discrepancies are largely due to the sample preparation and the measurement process. The thicknesses agree with the calculated values, and the expected trend in thickness variation for the superperiodic structures supports the accuracy of the transfer matrix results.

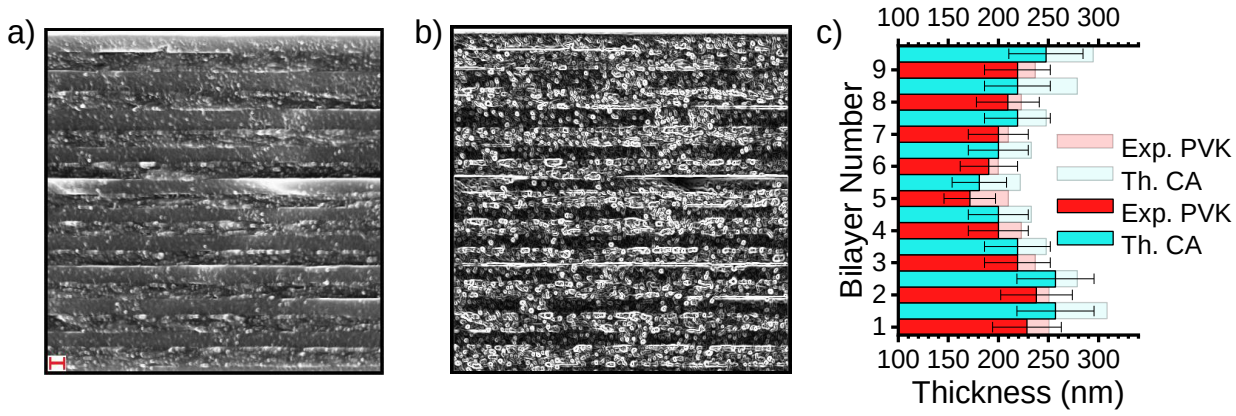

Figure 2.6. **a)** *SEM image of the cross-section of SPAE2.* **b)** *Same picture after contrast enhancement.* **c)** *Measured (solid bars with error) and calculated (faded bars) for sample SPAE2.* Adapted from [1]

2.2.5. Thermal shielding measurements - Parafilm. The aegises shielding efficiency was assessed by interposing alternatively an aegis or a reference between a light source and a sample while measuring and comparing its temperature increase. A simplified model for heating based on basic

thermodynamics was developed to obtain the essential parameters of the process. The model describes an asymptotic growth for the temperature increase over time, reported in **Equation 2.2**:

$$\Delta T(t) = \Delta T_{\infty}\left(1 - e^{-\frac{t}{\tau}}\right) \tag{2.2}$$

The terms equilibrium temperature (ΔT_{∞},), and the characteristic time of the process (τ), are found to be dependent on the incoming power, w_{lamp}, the mass and specific heat of the body (m and c respectively) and the heat exchange factor h, which is characteristic of the setup geometry and the subsequent heat exchange:

$$\Delta T_{\infty} = \frac{w_{lamp}}{h} \tag{2.3a}$$

$$\tau = \frac{mc}{h} \tag{2.3b}$$

Equation 2.2, with **Equation 2.3a** and **2.3b,** predicts the temperature increase over time in heated samples and will therefore be used to fit the experimental data and extrapolate the ΔT_{∞} and τ parameters. The initial shielding experiment was conducted using a solid paraffin film (Parafilm). To perform the experiments, I designed and assembled a setup represented in **Figure 2.7a**, allowing to measure the temperature increase of a Parafilm sample upon illumination via a fiber coupled illuminator (not represented; inserted in the support with hole on the right). Parafilm is applied on glass for stability, its temperature measured from behind, and an aegis or a reference respectively are placed in front and used to shield it. **Figure 2.8a** illustrates the dynamic temperature increase of Parafilm under irradiation when shielded by a clear glass reference substrate or various aegises, all cast on the same substrate: bare glass reference (black squares), AE1 (purple circles), AE2 (orange diamonds), or TAE1 (brown hexagons). In all cases, the temperature increases linearly before reaching a plateau, indicating thermal equilibrium. The smallest ΔT_{∞} was observed with TAE1, followed by AE2 and AE1. The curves were then fitted using **Equation 2.2** to extract the $\Delta T_{\infty,aegis}$ equilibrium value for each aegis. These values were used together with the equilibrium value relative to the reference $\Delta T_{\infty,ref}$ to calculate the "shielding efficiency" η:

$$\eta = 1 - \frac{\Delta T_{\infty,aegis}}{\Delta T_{\infty,ref}} \tag{2.4}$$

The fittings showed good agreement between the data and the model. The efficiencies were found to be 6% for AE1, 10% for AE2, and 18% for TAE1 (Table 2).

This outcome can be explained by examining the liquid paraffin absorption spectrum in **Figure 2.4a**. Aegis AE1 (**Figure 2.4b**) has a bandgap centered at 950 nm, partially overlapping with paraffin's absorption peak at 900 nm. AE2 (**Figure 2.4c**) has a bandgap at 1160 nm, which overlaps with the stronger absorption peak at 1200 nm, accounting for its higher efficiency. TAE1, in addition to covering both peaks, exhibits strong fringes in the spectral region between the two bandgaps, partially shielding paraffin's absorption peak at 1000 nm. The greater efficiency of TAE1 is due to its ability to simultaneously shield all three absorption peaks.

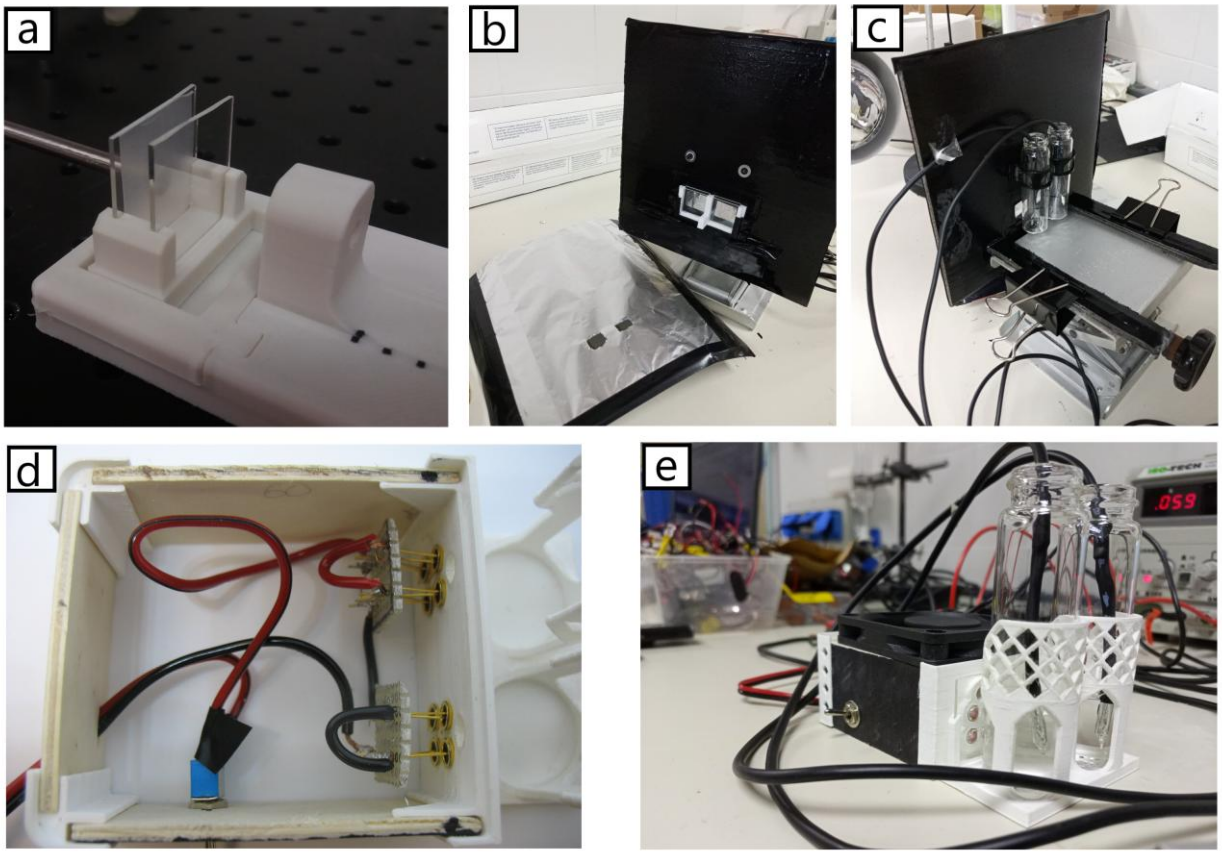

Figure 2.7. **a)** *Setup for the Parafilm^{TM} thermal experiments.* **b,c)** *front and back respectively of the setup for the water thermal experiments using an incandescent lamp as a light source.* **d,e)** *interior and exterior respectively of the setup for water thermal experiments with LED light source.* Adapted from [1]

To express quantitatively these differences in efficiency we defined a parameter, called spectral coverage (S). Given $T_{Aegis}(\lambda)$, transmission spectrum of an aegis, $T_{Ref}(\lambda)$ transmission spectrum of the reference and $A(\lambda)$, absorbance spectrum of the material to be shielded:

$$S = 1 - \frac{\int_{\lambda_1}^{\lambda_2} T_{Aegis}(\lambda) \cdot A(\lambda) d\lambda}{\int_{\lambda_1}^{\lambda_2} T_{Ref}(\lambda) \cdot A(\lambda) d\lambda} \tag{2.5}$$

The integration was carried out numerically, specifically for the Parafilm case, by integrating over the 900 to 1400 nm range, which encompasses all relevant bandgaps. The efficiencies of the various aegises are plotted as brown circles in **Figure 2.8b**, alongside their respective spectral coverage values calculated using **Equation 2.5**. The results show that as spectral coverage increases, so does efficiency. This is expected, as spectral coverage is influenced by how well the aegises are tuned to the absorption peaks they shield, as well as the intensity of the shielded peaks.

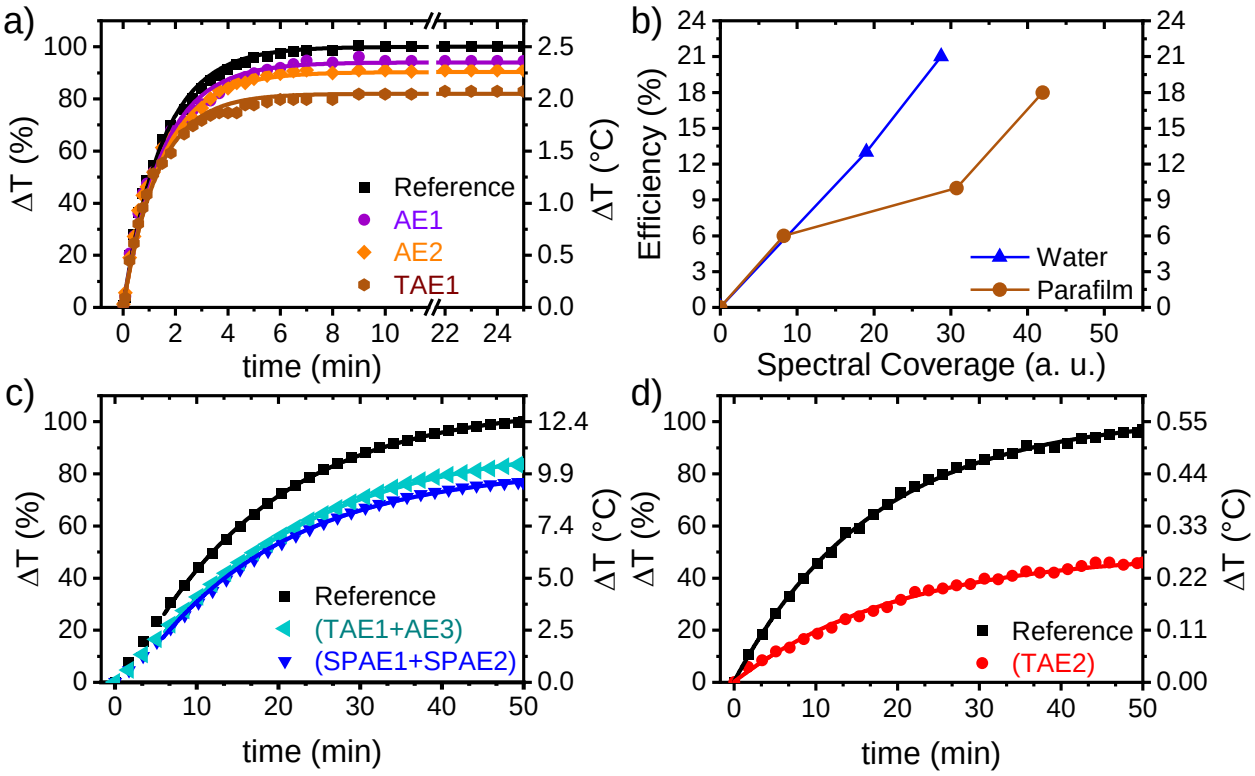

Figure 2.8. *Temperature increase, measured over time during thermal experiments, for* **a)** *Parafilm sample,* **c)** *water sample illuminated with incandescent bulb,* **d)** *water sample illuminated by 970 nm LED. Marks are experimental data; continuous lines are fittings.* **b)** *Efficiency of the aegises and reference against the respective spectral coverage values. Lines are only a guide to the eye.* Adapted from [1]

These findings are significant on two levels. First, the absorption peaks in the paraffin film correspond to overtones and combination bands of C-H bonds,18 which, with slight variations, are common to many organic substances and polymers. This demonstrates how a VIS-transparent, NIR-reflective aegis can effectively reduce temperature increases in a wide range of materials, such as those used in packaging. Compared to the results reported by Radice et al., which showed an

efficiency of 12%, the current results represent an improvement in three areas: better performance, the use of more easily processed materials, and a structural design that achieves these results using polymers with a relatively low dielectric contrast (0.22 in this study versus 0.34 in Radice et al.).

2.2.5. Shielding experiments - water, incandescent lamp. We used two different methods to evaluate the aegises' efficiency under different conditions of spectral coverage. In the first method, we used a high-power incandescent bulb as a broadband light source, while in the second method we used 970-nm LEDs as a narrowband emitter. In the first case, a more powerful light source was used due to the larger volume of material to be shielded compared to the previous experiment (8 g of water versus 0.05 g of Parafilm). The setup used for the latter experiment is represented in **Figure 2.7** (panel b: front, panel c: back); a powerful incandescent lamp (Philips IR250, 250 W) was used as the light source. A removable component enabled the simultaneous use of two aegises and two references for each side, to cover the two windows through which the light passed. Indeed, to make the shielding effect more obvious, we shielded the sample with two aegises simultaneously. An additional screen, covered in aluminum foil (lower left of the panel), was placed in front of the black screen during measurements. The vials were positioned behind the windows, as illustrated in **Figure 2.7c**, and the temperature of their contents was recorded over time with thermistors. Due to the lamp's asymmetrical light emission, each measurement was repeated twice, swapping the positions of the aegis and reference in each run averaging the final results.

The selected aegises pairs for the measurements were TAE1+AE3 and SPAE1+SPAE2. The first pair was chosen as a selective reflector for light near the first three absorption peaks of water and is well documented in the literature. The second pair acts as a broadband reflector with broader spectral coverage and was used to evaluate the effectiveness of the new superperiodic structures presented in this study. Due to the greater mass and specific heat of water, which increase the time constant τ (**Equation 2.3b**), the time required to reach equilibrium temperature was longer. The plotted heating curves, shown in **Figure 2.8c**, include a lag time (t_0) resulting in a modified version of **Equation 2.2**:

$$\Delta T(t) = \Delta T_{\infty}\left(1 - e^{-\frac{t-t_0}{\tau}}\right) \tag{2.6}$$

Fitting the data using **Equation 2.6** allowed the determination of ΔT_{∞} and the efficiency of the aegises, which were 13% for the pair TAE1+AE3 (with bandgaps at 950 and 1160 nm for TAE1 and at 1450 nm for AE3) and 21% for the pair SPAE1+SPAE2 (the two superperiodic aegises), as shown in Table 2. The spectral coverage for both pairs was calculated using **Equation 2.5**, integrating over the range from 780 to 2400 nm. The efficiencies of these pairs were then plotted as blue squares

against their respective spectral coverage values in **Figure 2.8b**. As expected, the SPAEs exhibited greater spectral coverage, resulting in higher efficiency, while the TAE1+AE3 pair exhibited lower spectral coverage and efficiency. This result is due to the broader NIR reflectance and higher reflectance intensity of the SPAEs, as well as some scattering due to defects in the SPAE2 sample. It should be noted that the two data sets shown in **Figure 2.8b** are not directly comparable as the efficiencies were measured under different conditions and the spectral coverage was calculated over different ranges.

2.2.7. Shielding Experiment – Water, LED. To determine the theoretical efficiency limit, we performed a second experiment in which we irradiated liquid water with a light source whose wavelength perfectly matches one of its absorption peaks (**Figure 2.4a**). The measurement setup in this condition included a homemade circuit and is shown in **Figure 2.7d** (interior) and **2.7e** (exterior). The circuit powered two groups of four 970 nm, 5 mW LEDs each, providing illumination for each of the two water vials through the aegis/reference. A standard 12V PC fan was installed at the top of the setup to cool the LEDs and prevent overheating. This setup simulates the scenario where all absorption peaks are shielded by white light. As expected, the ΔT_∞ values were significantly lower compared to the previous experiment due to the lower power of the LEDs, with 100 % corresponding to a temperature increase of about 0.55 °C. **Figure 2.8d** shows the temperature rise of water when shielded by TAE2 or its reference. Due to the long duration of these measurements and in contrast to the previous cases where the room temperature variations were negligible compared to ΔT_∞, we accounted for the room temperature variations by subtracting them from the measured curves to remove environmental influences. The data were then fitted using **Equation 2.6**, and the results are summarized in **Table 2.2**.

The efficiency reached η = 52 %, showing that high shielding efficiencies can be achieved with transparent aegises if strong spectral coverage of the absorption peaks is provided. It also opens up possibilities for novel, processable materials with higher dielectric contrast. These materials could potentially enable broader, more intense and selective bandgaps that can shield absorption peaks even when the angle of incidence deviates from the norm.

Table 2.2. *Values of equilibrium temperature (ΔT_∞), shielding efficiency (η), characteristic time (τ), delay (t_0), and heat exchange coefficient (h) obtained for reference and aegises by fitting the plots in* **Figure 2.8a**, **c** *and* **d**.

Aegis	Material	ΔT_∞ (°C)	η (%)	τ (s)	t_0 (s)	h (mW K^{-1})
Reference	Parafilm	2.50	0	80	-	[a] 2.43
AE1	Parafilm	2.34	6	73	-	[a] 2.57

AE2	Parafilm	2.27	10	77	-	[a] 2.49
TAE1	Parafilm	2.05	18	74	-	[a] 2.56
Reference	Water	13.0	0	1140	80	[b] 30
TAE1+AE3	Water	12.5	13	1180	116	[b] 28
SPAE1+SPAE2	Water	10.6	21	1210	118	[b] 28
Reference	[c] Water	0.55	0	~1100	-	[b] 27
TAE2	[c] Water	0.26	~52	~1100	-	[b] 27

[a] *The heat exchange coefficient h is calculated from τ according to its definition (**Equation 2.3b**), known Parafilm™ mass to be 0.05 g and assuming specific heat 2.3 J g^{-1} $K^{-2.58}$* [b] *h is calculated as stated before, known water mass to be 8 g and its specific heat 4.196 J g^{-1} K^{-1}.* [c] *Light source is the LED.* Adapted from [1]

2.3. Conclusion

This study demonstrates that polymer dielectric aegises can effectively shield materials from unwanted radiative heating. Various spin-cast multilayer structures, made from widely available commercial polymers, reduced radiative heating from different light sources by up to 20%, with maximum efficiency reaching 52%. The reduction in heating is strongly influenced by the incident spectrum, the amount of light reflected by the aegises, and the alignment between the photonic band gap (bandgap) and the absorption peaks of the material being shielded (spectral coverage). Efficiency is enhanced by tuning the bandgap to the wavelengths where the material's absorption coefficient is highest, or by increasing the structural complexity to improve overall reflectance. Superperiodic structures, which exhibit broad, multi-peak bandgaps, demonstrated the highest efficiency, though this resulted in reduced transparency in the visible spectrum.

The results here obtained were promising for thermal shielding applications, and the following work presented in the next chapter will focus on evaluating the impact of dielectric contrast on the aegises' efficiency. Additionally, an improved design rationale will be developed, considering both the spectrum of the light source and the absorption characteristics of the material to be shielded. These steps aim to further optimize the shielding performance and broaden the applicability of the technology.

Bibliography

1. A. Lanfranchi, H. Megahd, P. Lova , D. Comoretto. *ACS Appl. Mater. Interfaces*, **14**, 12, 14550, (**2022**)

2. A. Jentsch , C. Beierkuhnlein. *CR Geosci.*, **340**, 9, 621, (**2008**)

3. G. A. Meehl, F. Zwiers, J. Evans, T. Knutson, L. Mearns , P. Whetton. *Bull. Am. Met. Soc.*, **81**, 3, 427, (**2000**)

4. The 2030 Agenda for Sustainable Development, https://www.un.org/ga/search/view_doc.asp?symbol=A/RES/70/1&Lang=E (accessed December, 2024)

5. European Green Deal, https://ec.europa.eu/info/strategy/priorities-2019-2024/european-green-deal_en (accessed December, 2024)

6. M. E. Hossain, S. Rej, S. M. Saha, J. C. Onwe, N. Nwulu, F. V. Bekun , A. Taha. *Sustainability*, **14**, 13, 7537, (**2022**)

7. Z. Sun, Z. Ma, M. Ma, W. Cai, X. Xiang, S. Zhang, M. Chen , L. Chen. *Buildings*, **12**, 2, 128, (**2022**)

8. E. Akpinar-Ferrand , A. Singh. *Environ. Sci. Policy*, **13**, 8, 702, (**2010**)

9. U. S. E. I. Administration, Air conditioning accounts for about 12% of U.S. home energy expenditures, https://www.eia.gov/todayinenergy/detail.php?id=36692 (accessed December, 2024)

10. E. D. H. Karin Lundgren Kownacki, Tuan Anh Chu, Johanna Alkan Olsson, Per Becker. *Int. J. Biometrol.*, **62**, 3, 132, (**2017**)

11. Z. Zhang, C. Liu, X. Chen, C. Zhang , J. Chen. *Appl. Thermal Eng.*, **125**, 567, (**2017**)

12. J. Vasagar, *Lion City: Singapore and the invention of modern Asia.* Little Brown, **2021**

13. A. P. Raman, M. A. Anoma, L. Zhu, E. Rephaeli , S. Fan. *Nature*, **515**, 7528, 540, (**2014**)

14. J. Jaramillo-Fernandez, H. Yang, L. Schertel, G. L. Whitworth, P. D. Garcia, S. Vignolini , C. M. Sotomayor-Torres. *Adv. Sci.*, **9**, 8, 2104758, (**2022**)

15. Paint it Cool, https://www.dispersions-pigments.basf.com/portal/streamer?fid=560474 (accessed December, 2024)

16. U. G. Ugboka, J. N. Ihedioha, N. R. Ekere , F. O. Okechukwu. *Int. J. Environ. Anal. Chem.*, 1, (**2020**)

17. C. Kittas , A. Baille. *JAER*, **71**, 2, 193, (**1998**)

18. C. Berrueta, E. Heuvelink, G. Giménez , S. Dogliotti. *Sci. Hortic.*, **265**, 109250, (**2020**)

19. S. Guichard, C. Gary, J. J. Longuenesse , C. Leonardi. *Acta Hortic.*, 223, (**1999**)

20. S. Hemming, F. Kempkes, N. van der Braak, T. Dueck , N. Marissen, *Greenhouse cooling by NIR-reflection*. From ISHS Biennial Meeting, Leuven (BG), **2006**

21. Reference Air Mass 1.5 Spectra, https://www.nrel.gov/grid/solar-resource/spectra-am1.5.html (accessed December, 2024)

22. H. Khandelwal, R. C. G. M. Loonen, J. L. M. Hensen, A. P. H. J. Schenning , M. G. Debije. *J. Mater. Chem. A,* **2**, 35, 14622, (**2014**)

23. L. Zhang, A. Wang, T. Zhu, Z. Chen, Y. Wu , Y. Gao. *ACS Appl. Mater. Interfaces*, **12**, 31, 34777, (**2020**)

24. Y. Li, J. Liu, J. Liang, X. Yu , D. Li. *ACS Appl. Mater. Interfaces*, **7**, 12, 6574, (**2015**)

25. C. Nakamura, K. Manabe, M. Tenjimbayashi, Y. Tokura, K.-H. Kyung , S. Shiratori. *ACS Appl. Mater. Interfaces*, **10**, 26, 22731, (**2018**)

26. S. V. Radice, P. Sriniviasan, D. Comoretto, S. Gazzo, *One-dimensional planar photonic crystals including fluoropolymer compositions and corresponding fabrication methods*, WO 2016/087439 Al (**2016**)

27. W. Smith, *Dictionary of Greek and Roman Biography and Mythology.* Walton, UK, London, **1849**

28. H. Song, K. Singer, Y. Wu, J. Zhou, J. Lott, J. Andrews, A. Hiltner, E. Baer, C. Weder, R. Bunch, R. Lepkowicz , G. Beadie, *Layered polymeric optical systems using continuous coextrusion.* SPIE, **2009**

29. P. Lova, G. Manfredi , D. Comoretto. *Adv. Opt. Mater.*, **6**, 24, 1800730, (**2018**)

30. V. M. Menon, M. Luberto, N. V. Valappil , S. Chatterjee. *Opt. Express*, **16**, 24, 19535, (**2008**)

31. L. Frezza, M. Patrini, M. Liscidini , D. Comoretto. *J. Phys. Chem. C*, **115**, 40, 19939, (**2011**)

32. Y. Ozaki, T. Genkawa , Y. Futami, Near-Infrared Spectroscopy, in Encyclopedia of Spectroscopy and Spectrometry (Third Edition), Academic Press, Oxford, **2017**

33. J. E. Bertie , Z. Lan. *Appl. Spectrosc.*, **50**, 8, 1047, (**1996**)

34. J. Workman , L. Weyer, *Practical Guide and Spectral Atlas for Interpretive Near-Infrared Spectroscopy*. CRC Press, Boca Raton, Florida, USA, **2012**

Chapter 3 – Engineering Aegises and their Design Rationale

This chapter is partially published as Lanfranchi et al., *Chemical Engineering Science* **2024,** 283**,** 5 119377[1]

Abstract

Following up to the promising results described in the previous **Chapter 2**, I continued on the topic of using distributed Bragg reflectors as aegises, near-infrared reflectors for thermal shielding. In this regard, I developed a new rationale to optimize *a priori* the efficacy in thermal shielding of a certain structure; this rationale considers the spectrum of incident radiation, the absorption spectrum of the sample to be shielded, as well as the optical response of the aegis. Following this reasoning, I designed an optimized structure, a tandem of four distributed Bragg reflectors stacked one on top of the other. I afterwards fabricated the structure out of different polymer pairs, to test the effect of material choice on the aegises' performances. Indeed, I fabricated aegises going from commercial polymers (polystyrene and cellulose acetate) to technical, high-performance ones (the fluorinated polymer Aquivion and poly(*N*-vinylcarbazole)). The progressive increase in difference of refractive index between the building blocks (dielectric contrast) in the aegises fabricated of progressively better-performing materials, going from 0.11 to 0.27, yielded a consistent improve in the efficiency, both in calculations as well as in the experiment. Indeed, when using aegises to shield water from the heating effect of 250 W incandescent lamp, efficiencies rising from 6 to 27 % were obtained. Additionally to the possibility of improved efficiency, the use of technical materials would allow a consistent material saving.

3.1. Introduction

As stated in the previous chapter, the issue of global warming is increasingly worrying, with its main solution (air conditioning systems) being instead more part of the problem. [2-4] Therefore, there is a strong need for passive solutions able to complement air conditioning or to replace it altogether without the related energy consumption and heat and CO_2 emissions. In this regard, I demonstrated how distributed Bragg reflectors (DBRs) can perform as effective aegises, able to reflect the NIR radiation which causes the heating of indoor environments without losing transparency in the visible range;[5] this could be especially useful for buildings and cars windows, and for greenhouses in the form of removable plastic films.[6, 7] In the first chapter, I tackled the surface of the design and fabrication of aegises, focusing on the development of different structures out of easy-to-handle materials.[5] In this chapter, I will focus instead on the use of different materials for the fabrication of aegises, going from cheap, commercial polymers such as polystyrene (PS) and cellulose acetate (CA), to technical ones such as poly(*N*-vinylcarbazole) (PVK) and Aquivion (AQ). This allows to investigate the effect of dielectric contrast, the difference in refractive index between the alternating layers making up the DBR;[8-10] this parameter indeed affects the width and intensity of the high-reflectance photon bandgap.[10] This, as I will show later in the chapter, has a strong effect on the aegises' efficiency. In the same work, I present a complete model to predict the efficiency of aegises, which fully contemplates the absorption spectrum of the material to be shielded, the emission spectrum of the light source, as well as the aegises' transmittance.

3.1.1. Materials selection. Three polymer pairs for a total of four polymers were used in this work. PVK and CA were already discussed thoroughly in **Chapter 2** (**Subsection 2.2.1**, **Figure 2.3**); their refractive indices are reported again in **Figure 3.1** (black and red curves respectively). The PVK-CA pair provide a dielectric contrast around 0.2 (depending on wavelength). Since the idea was to investigate the effect of dielectric contrast on the aegises' efficiencies, I needed at least two other polymer pairs with quite different dielectric contrast. This requirement rules out many materials with refractive index close to CA, such as poly (acrylic acid) (PAA) or poly(vinylalcohol). Therefore, to provide a higher dielectric contrast, I used the fluoropolymer AQ (its structure formula reported in **Figure 3.1a**),[11] to be used in combination with PVK. On the other hand, to provide a lower dielectric contrast, I used polystyrene (structure formula in **Figure 3.1b**)[12] to be used in conjunction with CA. The refractive indices of the two materials are reported, alongside the spectra of PVK and CA, in **Figure 3.1c**. PS has a refractive index lower than PVK, around 0.1-0.05 lower depending on the wavelength.[13] It is still remarkably high for a polymer, due to the presence of the aromatic ring; this ensures a sufficient dielectric contrast to observe the emergence of PBGs with a reasonable number

of layers.[8, 9, 14] AQ, on the other hand, possesses an extremely low refractive index, being it around 1.35.[15] This very low refractive index is typical of fluorinated compounds, especially of other perfluorinated polymers such as Hyflon.[16] However, AQ can be used in conjunction with PVK without necessity of plasma treatments, as its wettability with respect to PVK's solutions in toluene is sufficient for spin coating.

These four materials could be arranged to form three polymer pairs in order of increasing dielectric contrast: PS-CA ($\Delta n = 0.11$), PVK-CA ($\Delta n = 0.18$) and PVK-AQ ($\Delta n = 0.28$). As far as processability is concerned, PS can be dissolved in toluene. AQ, instead, is commercialized as a water/ethanol dispersion; working with AQ is more difficult than other polymers due to its sensitivity to environmental conditions.[1, 15]

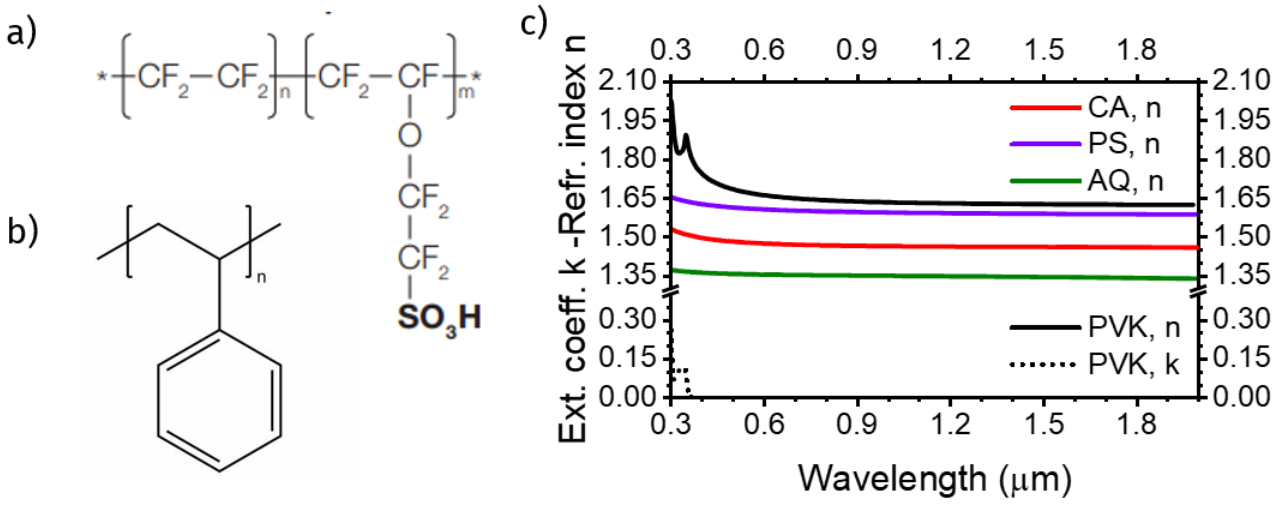

Figure 3.1. a) *Structure formula of Aquivion,* **b)** *Structure formula of polystyrene,* **c)** *Refractive indexes of cellulose acetate (red line) polystyrene (violet line), Aquivion (green line) and poly(N-vinylcarbazole) (black line). The extinction coefficient of PVK is represented by the dotted black line.*

3.2. Results & Discussion.

3.2.1. Theoretical efficiency of aegises. When working with the optical response of photonic crystals, the direct problem is always far easier than the inverse one – that means, deriving the optical response of a known structure is far easier than designing a structure with the desired optical response.[10, 17, 18] In this regard, the design rationale of aegises takes the form of an inverse problem. The first point towards an optimization of the optical response is understanding the parameter that needs optimization, that is the aegis' efficiency. In **Equation 3.4** in the previous chapter, I provided a simple definition for the intensity from the ratio of the temperature reached when the aegis or a reference are respectively used to shield the test material. The goal is therefore obtaining the theoretical value for the equilibrium temperature in the various cases.

I started by considering the energy per unit time per unit area (intensity I_{abs}, measured in [J] [s]$^{-1}$ [m]$^{-2}$) absorbed by a light-absorbing sample upon irradiation. I_{abs} can be easily derived from the Beer-Lambert law:[19]

$$I_{\text{abs}} = \int_{\lambda_1}^{\lambda_2} I_0(\lambda)(1 - e^{-\alpha(\lambda)\cdot z})d\lambda \tag{3.2}$$

Knowing the absorption coefficient $\alpha(\lambda)$, the thickness z of the material to shield from irradiation, and the irradiance spectrum energy per unit area per unit time per unit wavelength of the incident light ($I_0(\lambda)$, measured in [J] [s]$^{-1}$ [m]$^{-2}$ [nm^{-1}]). The integration range $[\lambda_1, \lambda_2]$ should ideally be $[0, \infty)$, but it is completely reasonable to limit it to where the irradiance of the light source has a nonnegligible value.

The addition of an aegis (or anything else) in front of the sample filters the spectrum of the light incident on the sample. This reduction is obtained by multiplying it by its transmittance $T_{\text{ae}}(\lambda)$, which by definition is the ratio of the intensity of the transmitted light to the incident one. Therefore, the energy per unit area absorbed by the shielded sample $I_{\text{abs, ae}}$ is:

$$I_{\text{abs, ae}} = \int_{\lambda_1}^{\lambda_2} T_{\text{ae}}(\lambda) I_0(\lambda)(1 - e^{-\alpha(\lambda)\cdot z})d\lambda \tag{3.2}$$

The energy absorbed by the sample per unit time should therefore be integrated over the whole surface exposed to irradiation, S:

$$w_{\text{abs, ae}} = \iint^{S} I_{\text{abs, ae}}\, dA \cong S\, I_{\text{abs, ae}} \tag{3.3}$$

Where the approximation yields as long as the irradiation is uniform enough over the whole surface, which is reasonable in the setup used for the experimentation. From **Equation 2.3a**, the final equilibrium temperature should be $\Delta T_\infty = \frac{w_{lamp}}{h}$, where h is the thermal exchange coefficient depending on the geometry of the system and environmental parameters.[5] w_{lamp}, the incoming power, must be replaced by $w_{\text{abs, ae}}$ when the aegis is shielding the sample. Therefore, the theoretical efficiency can be calculated as:

$$\eta_{\mathrm{t}} = 1 - \frac{\Delta T^{t}_{\infty,\ ae}}{\Delta T^{t}_{\infty,\ ref}} = 1 - \frac{\frac{w_{\mathrm{abs},\ ae}}{h_{ae}}}{\frac{w_{\mathrm{abs},\ ref}}{h_{ref}}} \cong 1 - \frac{I_{\mathrm{abs},\ ae}}{I_{\mathrm{abs},\ ref}} \frac{h_{ref}}{h_{ae}} \cong 1 - \frac{I_{\mathrm{abs},\ ae}}{I_{\mathrm{abs},\ ref}} \qquad (3.4)$$

Note that since the areas of irradiation *S* are always the same for reference and aegis due to the setup design $w_{\mathrm{abs},\ \mathrm{ae}}$ can be simplified to $I_{\mathrm{abs},\ ae}$ removing the dependency on *S*. In principle, the *h* parameters could be simplified as well since the thermal exchange with environment should not be affected by using an aegis instead of a reference, yielding a relatively simple formula for the theoretical efficiency. **Equation 3.4**, which predicts the efficiency of the aegises, allows for a complete rationale to optimize structures for the purpose of shielding a material from sunlight heating.

3.2.2. Designing the optimal structure. The efficiency calculated through **Equation 3.4** was used as an optimization parameter to design an optimal structure balancing ease of fabrication and efficiency. In principle, any optimization method is valid at this point; however, due to the many constraints and observations from the previous research, I opted for a simple brute force comparing all the viable alternatives. Based on the observations of **Chapter 2**, I opted for a tandem aegises consisting of approximately 30 bilayers (BLs), where a bilayer is a single pair of high-index and low-index layers. 30 BLs is a good compromise between noticeable effect even in case of a low dielectric contrast and ease to prepare a defects-free structure via spin-coating. Additionally, tandem aegises were chosen over the others type since:

1) Single aegises alone reflects a portion of the incident spectrum too small for to be strongly noticeable and give quantitative, low-error results; either tandem or superperiodic ones are therefore preferrable;[5]
2) Tandem aegises are intrinsically easier to fabricate than superperiodic ones. Indeed, if different structures are in tandem one on top of the others the variation of thickness is progressive instead of periodic, reducing the possibility of error;
3) There is not a decisive advantage between superperiodic structures and tandem when the total number of layers is factored in and equalized.[10]

Even when the approximate number of BLs is decided, there is still some freedom on how many DBRs put on top of the other to form the tandem structure. Indeed, 30 BLs can be achieved either by stacking 2 DBRs made up of 15 BLs each, or vice versa by 15 progressively different pairs of BLs, or by any combination in the middle. To have a complete view of the problem, I calculated the theoretical efficiency values for aegises consisting of 2, 3, 4, 5, 6, 8, and 16 stacks, with each stack containing 15, 10, 8, 6, 5, 4, and 2 BLs, respectively. A high-index material capping layer was added

to each aegis to slightly enhance reflectance. Not-in-scale schematics of the aegis structures are shown in **Figure 3.2a**, labeled as "Number of stacks × number of bilayers per stack." It can be seen how the thicknesses (which correspond to the periodicity of the layers making up each DBR) are progressively reducing for each stack, from the substrate going upward, to ensure the high-reflectance region is broad. Notably, the 3×10, 5×6, and 6×5 stacks contain 61 layers (30 BLs + high index capping layer), while the 2×16, 4×8, 8×4, and 16×2 structures contain 65 layers (32 BLs + capping layer). Note that the comparison is somewhat unbalanced in favor of the 65-layers structure as they have a slightly higher number of layers, but this is inevitable unless the total number of layers is so high that small variations do not affect the optical response, but such situation is not realistic for laboratory-made structures.

For each type of structure, different aegises were designed to exhibit reflectance peaks in multiple regions, all starting around 1200 nm, with the upper wavelength limit varying from 1300 to 1800 nm in 50 nm increments. **Figure 3.2b**, top panel, shows the water absorption spectrum with characteristic peaks at 950, 1200, 1450, and 1950 nm,[20, 21] alongside the irradiance spectrum of a T = 2700 K blackbody, calculated as per Planck's equation, where λ is the wavelength, c is the speed of light, $k_B$is Boltzmann's constant and h Planck's constant:

$$I_{bb} = \frac{2hc^2}{\lambda^5}\frac{1}{1-\exp\left(\frac{hc}{k_B T\lambda}\right)} \tag{3.5}$$

The two curves represent the irradiated sample, and the light source used in the experiments respectively (see the following sections). **Panels ii-viii** of **Figure 3.2b** compare these spectra to the calculated reflectance spectra of aegises with 2 to 16 stacks, exhibiting photonic band gaps (bandgaps) in the 1200-1700 nm range. Looking at the 2-stack tandem aegis (**panel ii**), its structure represented in **Figure 3.2a**, (2 x 16), it shows two distinct peaks, one centered on 1200 and the other centered on 1700 nm. This makes sense as the structure is very similar to TAE1 of the first chapter (Figure 2.1e), except in a different wavelength range. The bandgaps have a limited intensity and are heavily perturbed by the interference fringes of the two structures; this is more evident in (**panel iii**) where the 3x10 structure is reported. Indeed, the three peaks corresponding to the bandgaps of the three stacked DBRs are only slightly noticeable due to the perturbations. From **panel iv** onwards, increasing the number of stacks increases the number of reflectance peaks within the bandgap, causing the reflectance to transition to an oscillating plateau. Very little differences are visible amongst the 4x8, 5x6, 6x5 and 8x4 and 16x2 structures, apart from the slightly reduced overall intensity in the 5x6 and 6x5 due to the reduced number of layers.

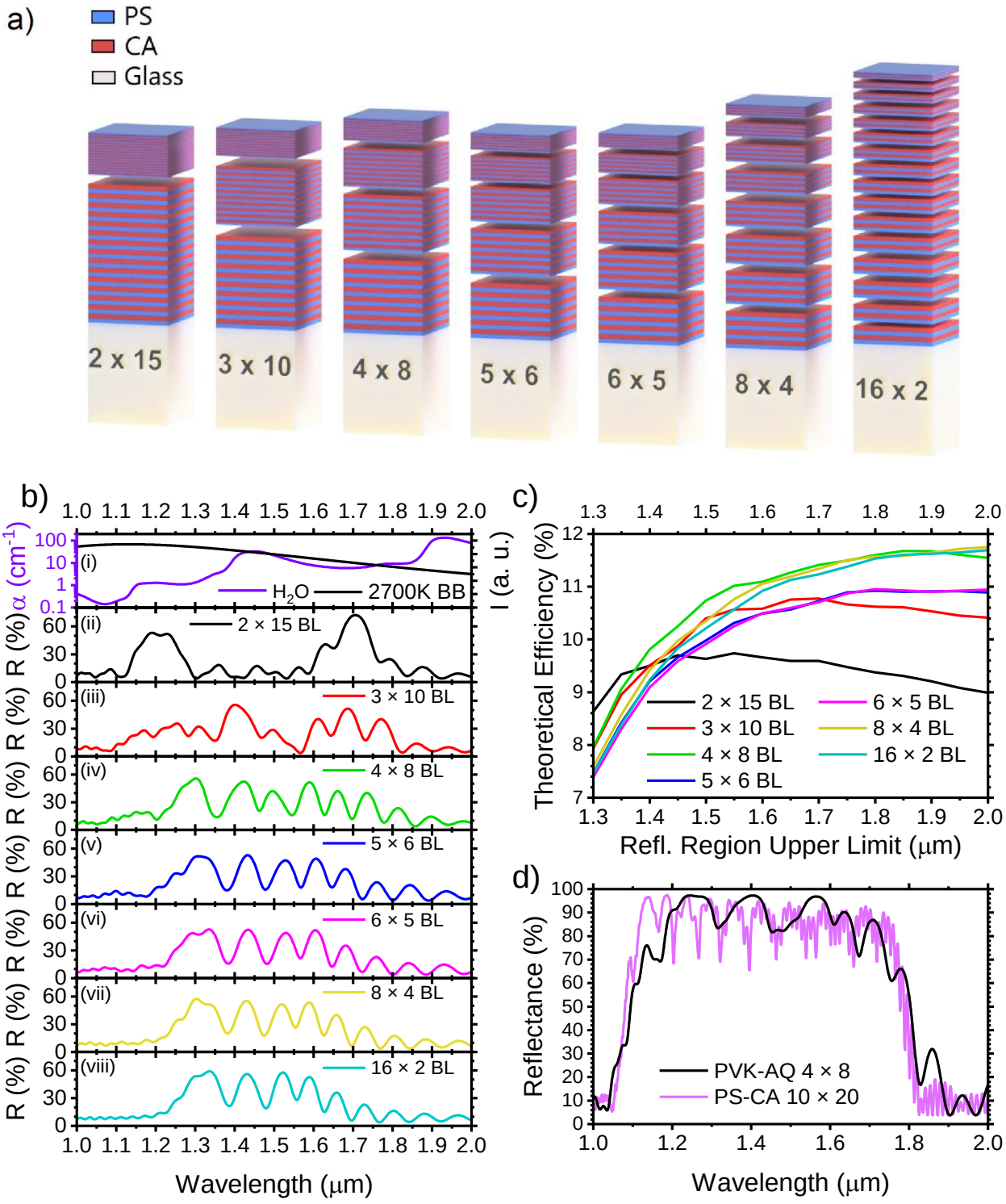

Figure 3.2. **a)** *Not-in-scale schematics of the aegises designed.* **b)** *2700 K blackbody irradiance spectrum (black line) and water absorption spectrum (magenta line) (panel 1) and calculated reflectance spectra for PS-CA aegises with different structures (lower panels). The scale of each reflectance spectrum is linear from 0 to 80 %.* **c)** *Efficiency of aegises with different structures as a function of the upper limit of the reflectance region, with 1200 nm as lower limit.* Adapted from [1]

Indeed, **Figure 3.2c** shows the shielding efficiency of the various structures as a function of the upper limit of the selected reflectance region. The results indicate that shielding efficiency increases with the extension of the bandgap region towards longer wavelengths, reaching a plateau for all structures. Only the 2×15 and 3×10 configurations showed efficiency reductions for bandgaps extending beyond 1550 and 1700 nm, respectively, likely due to reduced coverage of the lamp emission and the lower number of layers. Structures with 32 BLs generally outperformed those with 30 BLs (unsurprisingly), with the 4×8 structure demonstrating the best overall efficiency, though it was slightly surpassed by the 8×4 structure at wavelengths beyond 1900 nm. These differences are due to variations in coverage of the combination of the lamp's emission spectrum and the water absorption spectrum. The efficiency of the 4×8 structure reached 12.7% when the reflectance region spanned from 1200 nm to 1850 nm, equivalent to the 8×4 structure's efficiency from 1200 nm to 1950 nm.

From a process engineering perspective, achieving such broad bandgaps would require casting layers thicker than 300 nm, which is challenging to achieve via spin-coating. Reducing the upper limit of the 4×8 structure from 1850 nm to 1700 nm resulted in only a slight efficiency decrease of 0.3%, so the region of interest was restricted to [1200 nm – 1700 nm] to reduce layer thickness requirements. Consequently, the 4×8 structure was selected for testing as it is easier to engineer 4 DBRs for the desired thicknesses than 8. This is a choice for feasibility; with a coextrusion machine, a structure such as the magenta curve in **Figure 3.1d** could be achieved.[22] As apparent, by using a 10x20 structure the reflectance becomes essentially square-like in the wavelength range of interest.

3.2.3. Predicting aegises' efficiency. Once the optimal structure for our purposes was defined, I modeled the shielding efficiency for 4x8 aegises made out of each of the three selected material pairs. To simulate the experimental setup, I calculated the light absorption of a set path length of water (3.45 cm) shielded by either a glass reference (**Figure 3.2a**) or an aegis made out of PS-CA, PVK-CA or PVK-AQ respectively (**Figure 3.2b-d**). The resulting spectra are compared with a 2700 K blackbody spectrum (dashed line). Note that the shielding experiments are performed on water contained in a plastic bottle with non-negligible absorbance. However, it can be neglected in our calculation since an aegis must efficiently shield both materials and the absorbance profiles of water alone and water + container do not show significant differences.[5] The absorbed intensity is the quantity integrated in **Equation 3.2**: $(T(\lambda) \cdot I_0(\lambda)(1 - e^{-\alpha(\lambda)\cdot z})$. Therefore, the colored areas underneath the plots in **Figure 3.2** correspond to the absorbed intensity for each sample. Then, the ratio between each colored area in **Figure 3.2b-d** and the area in **Figure 3.2a** gives the theoretical efficiency values (**Equation 3.4**), which are 12.6 %, 20.7 % and 37.5 % for PS-CA, PVK-CA and PVK-AQ, respectively.

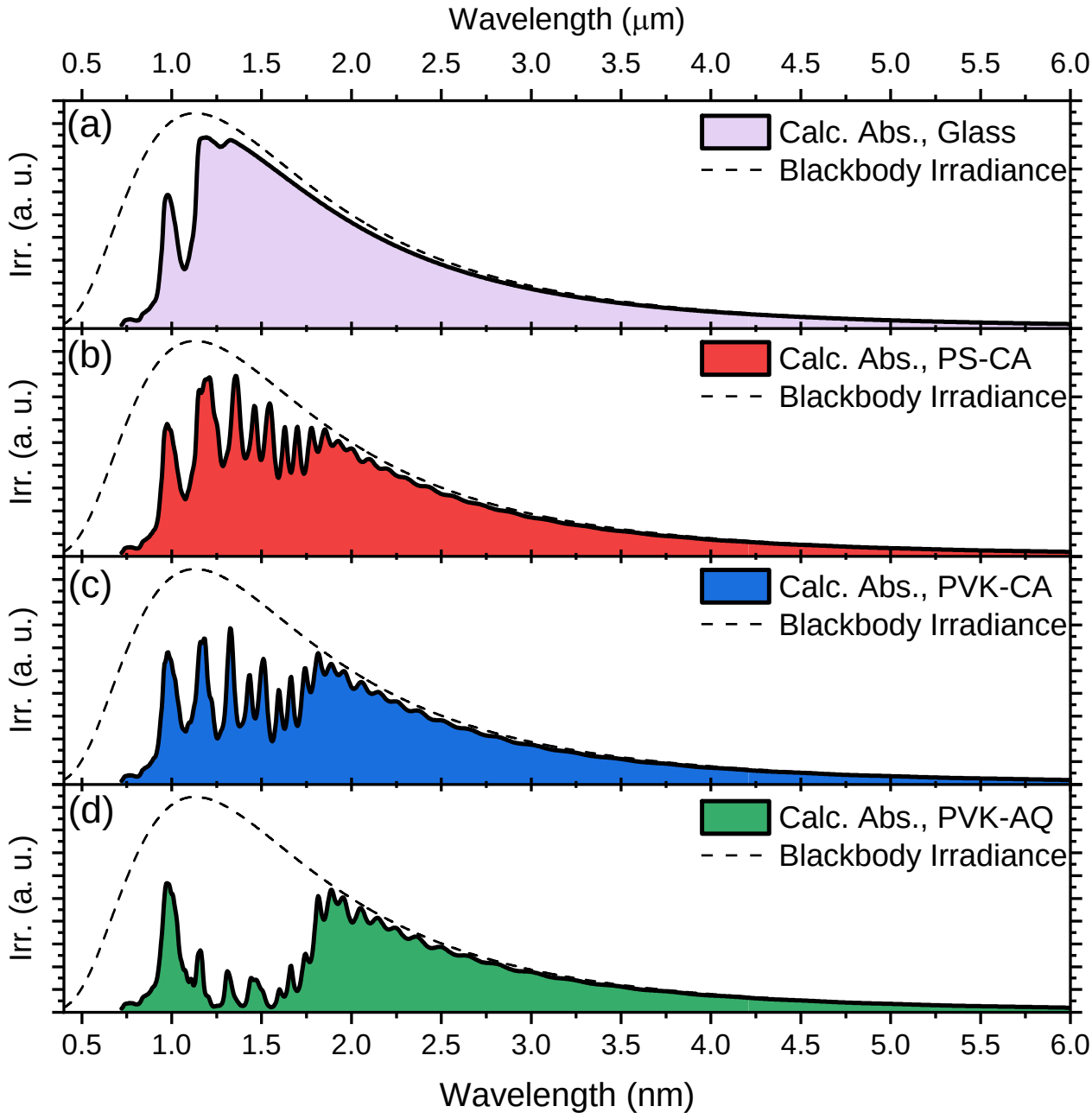

Figure 3.3. *Visual representation of the integration needed for Equation 3.2. The dashed line represents the 2700 K blackbody spectrum. The solid black lines correspond to the products* $T_{ae/ref} \cdot I_0(1 - e^{-\alpha z})$ *and the colored area is the integral of this quantity for* **(a)** *reference glass,* **(b)** *PS-CA,* **(c)** *PVK-CA, and* **(d)** *PVK-AQ aegises, respectively.* Reproduced from [1]

The obtained theoretical efficiencies are discussed and compared with experimental data below. Note that efficiencies are calculated without considering the imaginary part of the refractive index in the medium infrared (MIR) region, responsible for absorption. This is reasonable for the polymers used, as their thickness is extremely low, with the whole structures a few micrometers thick. On this scale, polymers are essentially transparent up to 3000 nm, a value which rises for perfluorinated polymers such as AQ due to the presence of fluorine atoms, emphasizing their importance in the

field.[23] In the spectral region where the incandescent lamp consistently emits light, polymers mainly show selected absorption peaks, such as the 3300 nm absorption peak of polystyrene.[24] Ignoring the absorption is instead a coarser approximation for the glass reference (which also acts as substrate for the aegises), as borosilicate glass tend to absorb light progressively more from 2500 nm onward.[25] This issue is nonexistent for the final application, as solar spectrum carries negligible energy beyond 2500 nm, therefore the materials here presented do not absorb sunlight consistently.[26]

An interesting consideration arising from the rationale is that a large amount of plastic can be saved by using high dielectric contrast building blocks. As an example, I reported in **Figure 3.2d** (black line) the PVK-AQ spectra needed for a shielding efficiency of 37.5 %. To obtain this spectrum, as stated before, a PVK-AQ ($\Delta n = 0.27$) structure made of 65 films (4 stacks, 8 BLs each plus a capping layer) was used. On the other hand, using the PS-CA ($\Delta n = 0.11$) pair requires more than 6 times the number of films, with a structure of 10 stacks, 20 BLs each for a total of 401 layers (purple curve). Even though such a high number of layers can be fabricated via coextrusion,[27] a large dielectric contrast is strategic for sustainability and technological applications as it allows higher efficiencies and a significant material saving.

3.2.4 Aegises' fabrication. Following the considerations in **Section 3.2.4**, three aegises were fabricated out of PS-CA, PVK-CA and PVK-AQ following **Appendix B.3.1**. They were tandem aegises made of 4 stacks of 8 BLs each plus a capping layer on top, as the "4 x 8" in **Figure 3.2a**, for a total of 65 layers. The aegises were fabricated via spin coating of polymer solutions/dispersions: PVK in toluene, CA in diacetone alcohol, PS in toluene and AQ as a water dispersion diluted with ethanol. To find the working conditions of concentration and spin speed, 8-layers DBRs with main bandgap at 1700 nm were fabricated out of each material pair. The $\frac{\lambda}{4}$ condition was confirmed by the absence of even-order bandgaps.[8, 10, 13] Afterwards, the whole aegis was built on top, reducing the rotational speed every other 8 layers according to the spin coating equation (**Eq. 2.1**) to obtain the four stacks with progressively thinner layers making up the structure. Pictures of the final aegises are reported in the insets of **Figure 3.4** and are commented in the following paragraph alongside their optical characterization.

3.2.5 Aegises' optical characterization. The experimental reflectance spectra were measured via the same setup described in the previous chapter,[1, 5, 15] whereas their modeling through theoretical calculations was calculated through the transfer matrix method as previously described. **Figure 3.4** compares the blackbody emission and water absorption spectra (**Figure 3.4a**) with the calculated (blue dotted lines in **Figure 3.4b-d**) and experimental (solid black lines) spectra of the three samples.

The blue line in **Figure 3.4a** shows the spectrum of water, with its multiple peaks due to the combination bands of overtones of vibrational modes,[20] chosen to test the efficiency of aegises in thermal shielding. The experimental spectra of the aegises result from an average of 9 spectra collected on the samples. The good agreement between experimental and calculated data attests to the homogeneity of the samples and the strict control of the deposition conditions. The spectrum of the PS-CA aegis (**Figure 3.4b**) shows a series of sharp reflectance peaks in the 1150-1900 nm range with an average intensity approaching 40%. As envisaged by the design, the spectrum does not show second and fourth order bandgaps, which should be observed in the 300-450 and 600-900 nm regions respectively. Conversely, the third (400-600 nm) and fifth (240- 360 nm) orders are detected. The absence of even diffraction orders shows that the structure is a "quarter wave stack" satisfying the quarter wave condition, with equal optical thicknesses for layers of both PS and CA. This condition ensures the broadest and most intense reflectance peaks. Despite the presence of reflectance peaks in the visible range, the structure is rather transparent, as its total transmittance integrated over the visible range is ~85%. Indeed, the photograph of the PS-CA aegis in the inset of **Figure 3.4b** shows the high transparency of the sample, which has only a slight orange tint assigned to the third order bandgap in the visible region.

The second sample (PVK-CA, **Figure 3.4c**) shows a series of reflectance peaks broader and more intense than PS-CA, in the 1100-1800 nm range. The intensity of the bandgap region is ~60%. The sample is a quarter wave stack, as indicated by the absence of the second order bandgaps. The third order peaks, which are more intense than those of the PS-CA aegis, make the structure less transparent in the visible range; its total transmittance in this region is ~77%. As can be seen by the photograph in the inset of **Figure 3.4c**, this aegis has a more pronounced dark yellow hue. The fourth and fifth order peaks are not present because PVK, unlike PS and CA, absorbs in the UV region, as seen from its refractive index in **Figure 2.1c**

The spectrum of the PVK-AQ aegis (**Figure 3.4d**) shows the effects of the larger dielectric contrast ($\Delta n \sim 0.28$). Although the structure is essentially the same, the peaks are so broad that they merge in a high-reflectance plateau in the 1150-1750 nm region. The overall intensity of the main bandgap region is much higher than for the other two samples, exceeding 95 % at its maximum. The third order peaks strongly reflect blue and green light, giving the structure a pronounced yellow tint, with the total reflectance of visible light increasing to 41 %. This can be observed in the picture of the aegis, in the inset of **Figure 3.4d**. Note that in this case modelled and experimental data show some minor differences. Such differences are noticeable in the interference pattern on the long wavelength side of the bandgap, in the slightly less pronounced structures within it, and in the presence of reflectance peaks in the visible range. Such differences are likely due to small thickness

inhomogeneities in the AQ layers, which require casting of highly concentrated dispersions. Note that all spectra were taken at normal incidence. However, the aegises exhibit angular dispersion, with their spectral features shifting to shorter wavelengths as the angle of incidence increases. This phenomenon strengthens the need for broadband reflection (thus wide dielectric contrasts) and is represented and commented on in the following sections.

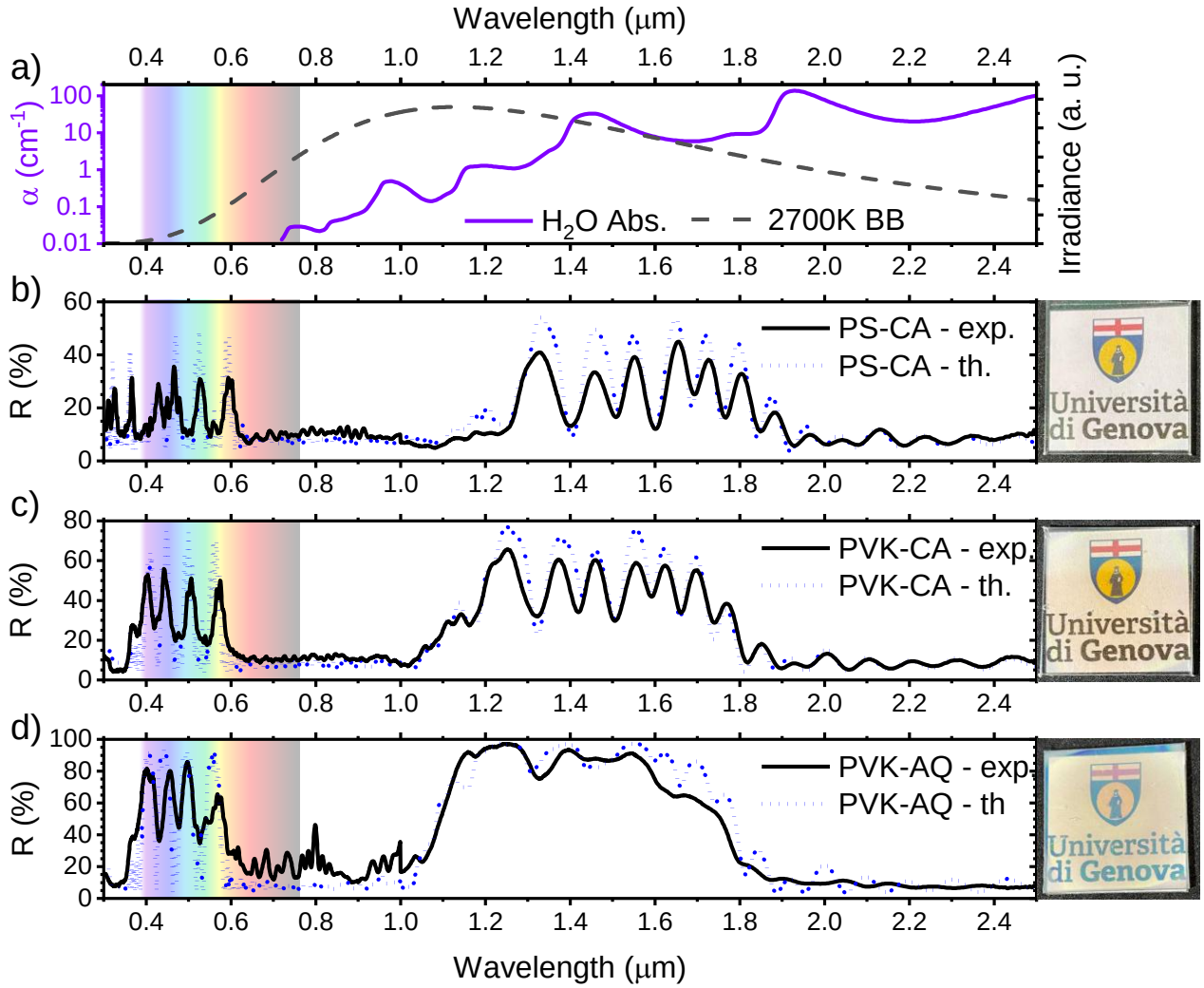

Figure 3.4. **a)** *Calculated 2700 K blackbody irradiance spectrum (black line) and water absorption spectrum (blue line).* **b, c, d)** *Measured (black lines) and calculated (red lines) reflectance spectra of aegises PS-CA, PVK-CA, PVK-AQ, respectively. In the insets, digital photographs of the aegises over a University of Genova logo.* Reproduced from [1]

The experimentally measured reflectance spectra of the three aegises (black lines in **Figure 3.4b-d**) were fitted using the transfer matrix method (dotted blue lines) to obtain the most probable thicknesses for the repeating layers, as described in previous works. Excellent agreement between measured and calculated spectra was obtained for both the PS-CA and the PVK-CA aegises, especially for the main bandgaps in the NIR region. In the Vis region, the agreement is still good and the few deviations are probably due to light scattering phenomena caused by minor local

inhomogeneities. The spectrum of the PVK-AQ aegis deviates more from the results of the calculation. As mentioned, in this case both PVK solutions and AQ dispersions are used in high concentration, leading to the formation of inhomogeneities in the films. Additionally, AQ is especially difficult to work with due to its sensitivity to environmental conditions, especially humidity, which tend to degrade the quality of the films. As the spectrum here report is the spatial average of the spectra taken in different points of the sample, it is consistent this is the less similar to its uniform, simulated counterpart.

As evidenced in **Chapter 2** (**Subsection 2.2.4** and **Figure 2.6)** direct measurements such as scanning electron microscopy on polymer DBRs are difficult, destructive and not particularly informative,[5, 15] therefore the thicknesses obtained by fitting the calculated spectra to the data are the most plausible ones and they are reported in **Figure 3.5**. The figure presents three bar plots, one for each aegis. The length of each bar (x-axis) represents the thickness of the layer of a given material in each stack composing the entire aegis. On the y-axis, the number of layers contained in the respective stack. The arrangement within the structure is given by the order of the bars, with the uppermost bar being the capping layer of high-index material, and the bottom ones being the thicknesses of the stack cast directly on the glass substrate. Note that the structures are represented by the 4 x 8 schematics in **Figure 3.1a**.

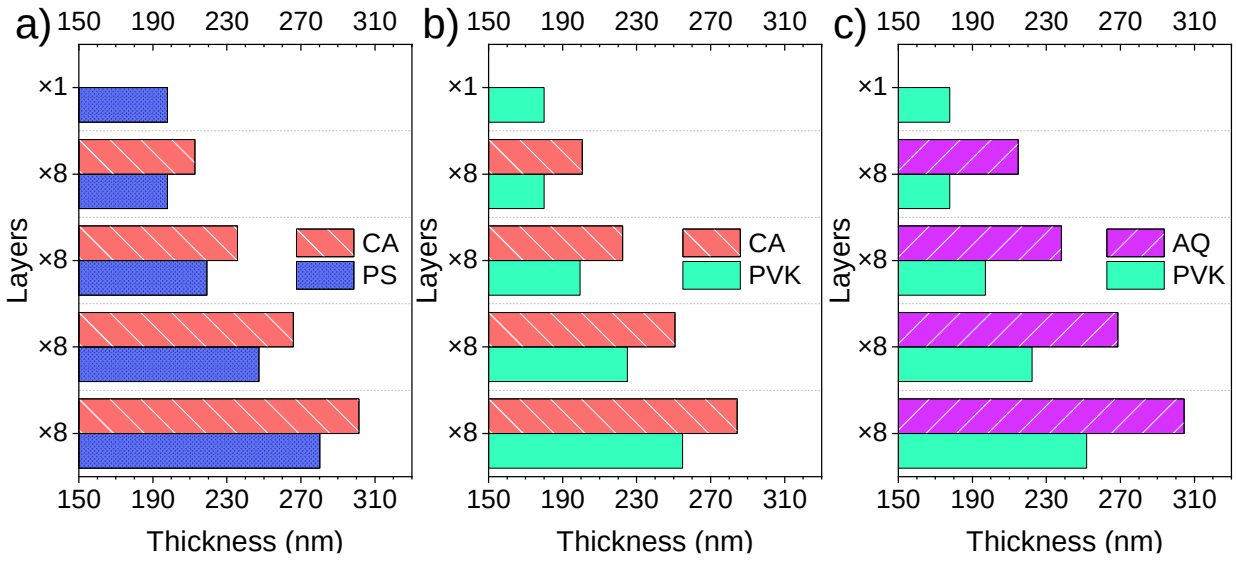

Figure 3.5. *Calculated layer thicknesses for the 4 stacks ×8 BLs aegises made out of* **a)** *PS-CA,* **b)** *PVK-CA,* **c)** *AQ-CA.* Reproduced from [1]

3.2.6. Thermal shielding experiments. The model used for the heating is the same reported in **Chapter 2**. In this chapter, to model the heating curves **Equations 2.2**, **2.3a** and **2.3b** shall be used to extrapolate the thermal equilibrium temperature, the h and τ parameters.[5]

The shielding measurements were performed with a home-made setup I designed and built *ad hoc.* It allowed heating 40 g of water contained in a plastic bottle through the reference/aegis at normal incidence. **Figure 3.6** pictures the setup used in the thermal experiments. The light from the incandescent lamp is channeled through the aluminum cone and then through the circular windows cut in the double-layer aluminum screen. This allowed the system to reach higher temperatures and observe more consistent effects than in **Chapter 2**. The aegis/reference is inserted in a single slot directly on the back of this window, so that all light passes through it. The heating water container is placed behind the aegis, with the thermistor inserted from above to monitor its temperature. In addition to the thermometer, the temperature increase was monitored with a thermal camera (not visible in the picture). The thermal camera measures the temperature through integration of thermal emission due to Planck's law between 8 and 13 μm.[19]

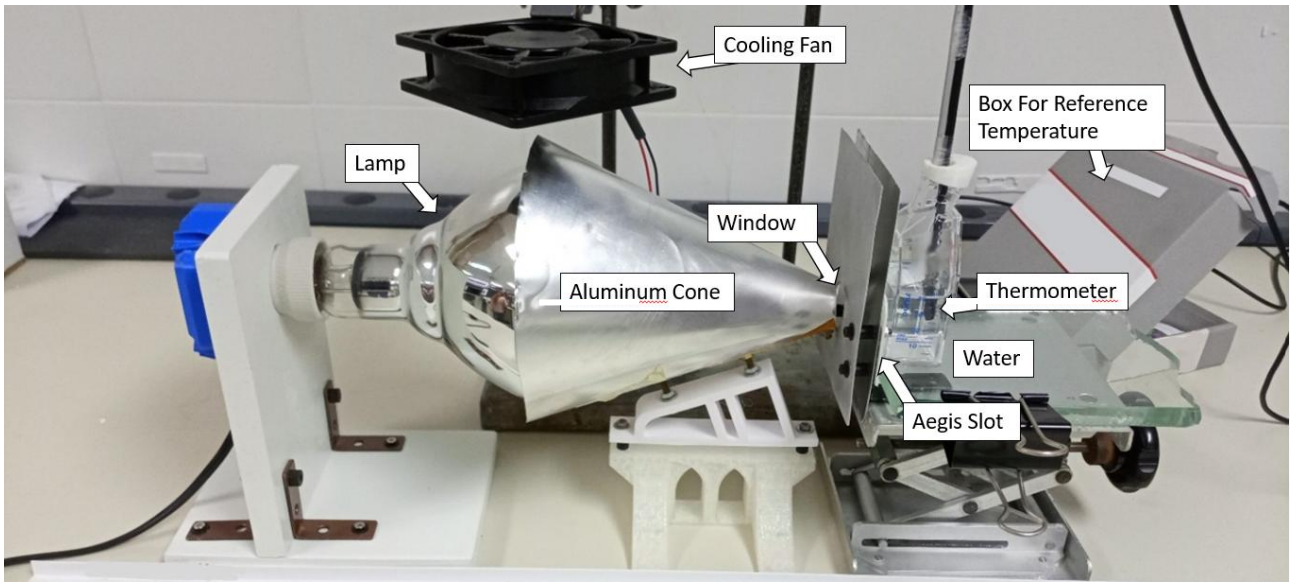

Figure 3.6. *Picture of the setup used in thermal experiments.* Reproduced from [1]

The measured heating curves for the reference and the aegis are reported in **Figure 3.7a**. Each of these curves corresponds to the average between five measurements. Environmental temperature variations due to the incandescent bulb heating up the also the surrounding environment (up to ~2.5 °C) were corrected for by subtracting a control water sample's temperature indirectly heated by the lamp (placed in the box for reference in **Figure 3.6**).

The water temperature increases, with respect to the environment, and approaches 30-50°C as shown by the heating curves reported in **Figure 3.7a**. Thanks to the improved design of the setup and the heating cone, temperature variations are much more pronounced with respect to those in **Chapter 2**. Here, the temperature variation increases asymptotically and reaches an equilibrium value approaching 48°C (100 %) for the reference and only 44 °C (94%) for the PS-CA aegis, 41 °C (86%)

for the PVK-CA aegis, and 34 °C (73%) for the PVK-AQ aegis. Thus, the aegises efficiently lower the final equilibrium temperature of the water specimen by a considerable amount. This is also confirmed by the thermal camera images of the water containers (**Figure 3.7b**). The latter show in color scale the temperature difference of the water containers after 1h of heating when the glass reference, the PS-CA, the PVK-CA, or the PVK-AQ aegis are used. The color scale was chosen to place emphasis on the heating region; white, yellow, orange and red are progressively colder. The measured temperatures, averaged over the entire container, are also shown as circles in **Figure 3.7b**. In addition to showing clearly the different effect of each aegis on the final temperature reached, the images prove the uniformity of temperature indicating that the shielding effect occurs over the entire area covered by the aegises and not just on the position of the thermistor.

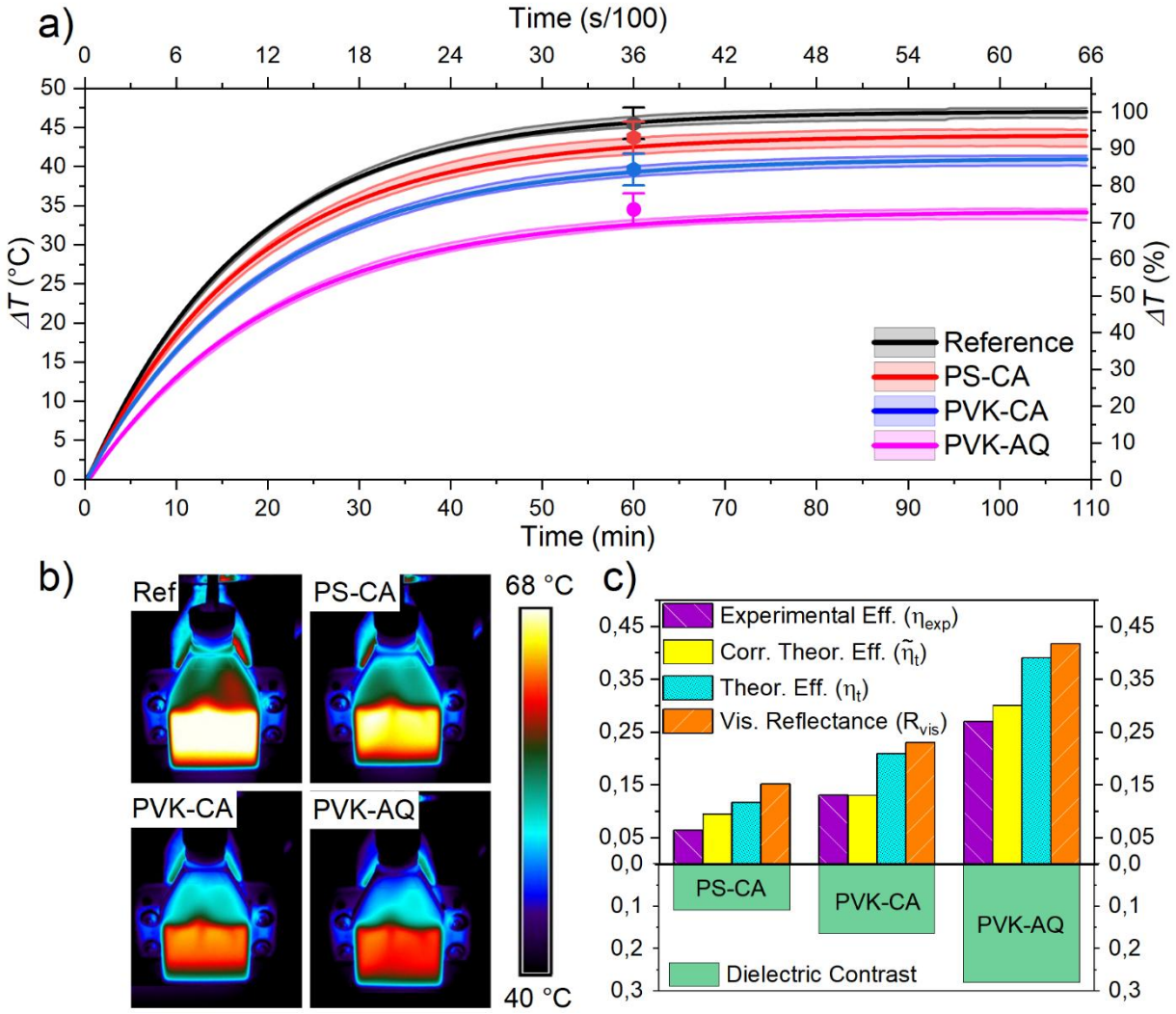

Figure 3.7. a) *Heating curves obtained with the reference and the various aegises. The shaded areas represent the experimental data with the associated error, while the thick continuous lines are fittings.* **b)** *Thermal images of the water sample after 1 h being shielded with the reference and the various aegises. Corresponding average temperatures are reported as circles in* ***a****.* **c)** *Bar plots representing the trend of efficiency (measured, corrected and calculated), integrated reflected light in the visible region, and dielectric contrast for the three aegises*. Reproduced from [1]

To quantify the shielding effect, the curves in **Figure 3.7a** were fitted with **Equation 2.2** to obtain ΔT_∞ for each aegis and the reference, and consequently their shielding efficiency η_{exp}, as well as the characteristic times of heating τ. Fitting results are reported in **Table 3.1**. Aegises' shielding efficiency increases with the characteristic time τ of the process, meaning the heating kinetics is affected by the aegises. This effect, albeit to a limited extent, changes the value of *h* (i.e. the rate at which the system loses heat to the environment). Regarding the equilibrium behavior, **Figure 3.7c** reports the experimental efficiencies η_{exp} calculated via **Equation 2.4** for each aegis as purple bars. The same figure shows the theoretical efficiencies η_{t}, as calculated via **Equation 3.4** when the *h* coefficients for aegis and references are simplified as assumed equal as yellow bars. When experimental *h* coefficients are included, the corrected theoretical efficiencies $\tilde{\eta}_t$ are obtained (cyan bars). The integrated reflectance of Vis light (R_{Vis}, orange bars) and the dielectric contrast for each aegis (green bars) are also reported. R_{Vis} complements the integrated transmittance in the Vis range; the higher R_{Vis}, the less Vis light is overall transmitted through the aegis:

$$R_{\text{Vis}} = \int_{400nm}^{700nm} R_{\text{ae}} d\lambda \;\cong\; 1 - \int_{400nm}^{700nm} T_{\text{ae}} d\lambda \qquad (3.6)$$

Where the effect of absorption has been ignored as aegises are nonabsorbent in the Vis range.

Increasing the aegises' dielectric contrast increases their efficiency, from only 6.6 % for the PS-CA aegis (Δn = 0.11), to the intermediate 13 % of the PVK-CA one (Δn = 0.17), up to 27 % for the AQ-PVK one (Δn = 0.28). The latter exceeds the previously obtained values but uses much fewer layers and a simpler structure. Indeed, in a previous report, 21% efficiency was achieved in the same situation, but using two superperiodic aegises 91-layers each against the 65-layers tandem aegis here reported, with a 2/3 reduction of the number of layers.

Due to minor inhomogeneities and fabrication defects, I assume that the aegises will not reach their theoretical shielding efficiencies. Indeed, theoretical values are ~0.4 times larger than the experimental values were observed for all aegises. After correction with the heat exchange factors *h*, the two values are comparable, even though, as stated before, the adequacy of this correction is debatable. Note that the efficiency values retrieved cannot be compared in any case to commercial methods as ours are calculated with a different light source (an incandescent lamp against sunlight) and with a precise amount of material. Changing one of the two would change efficiency. Calculations suggest the efficiency would be much higher using sunlight as a light source. I retrieved the theoretical efficiency values for the aegises in case the light source is sunlight; the efficiency values increase slight for PS-CA, doubles for PVK-CA and increases by half for PVK-AQ (see the Supporting

Material of the reference paper). Henceforth, our efficiency values are to be intended as a proof-of-concept demonstrating the efficacy of the rationale presented. Nonetheless, I demonstrated the efficiency rises with dielectric contrast; along with it, the total Vis light reflected from the structure also increases from 12% for PS-CA, to 23% for PVK-CA and finally to 41 % for the PVK-AQ aegis. The third diffraction order of the dielectric lattices, which ranges from the UV up to 600 nm for all the aegises, causes the Vis light reflectance. These highly reflective regions, spectrally located at 1/3 of the main bandgap's wavelength, are intrinsic to the structure and are avoidable only designing shields with bandgap in the 800-1200 nm spectral region. In that case, the third-order bandgaps appear in the 250-400 nm range instead of the Vis region, thus maintaining film transparency. In this case, though, the shielding effect can be heavily reduced due to the low absorption coefficients of materials in this spectral region. Therefore, shielding longer wavelengths such as those reported in this work promises much higher efficiency. This coming with the added characteristic of bright, iridescent structural colors with a tunable, colored metallic sheen can be an upside in some applications. For example, these are already highly desirable in next generation buildings, such as the iridescent plastic films that were installed at the Louvre museum. Using colored aegises would join the aesthetics with a functional purpose for buildings as well as other applications, such as high-end automotive. Furthermore, engineering aegises reflecting in both the NIR and green spectral regions could improve the crop yield of greenhouses in summer. Indeed, green light is absorbed by the earth to warm up the greenhouse but not by the plants to achieve photosynthesis. Additionally, tinted films applied on windows would not be dissimilar from solar concentrators, which are usually see-through but strongly orange- or yellow-colored.

Table 3.1. Values of equilibrium temperature (ΔT_∞), measured shielding efficiency (η_{exp}), characteristic time (τ), delay (t_0), heat exchange coefficient (h), theoretical efficiency (η_{t}) and corrected theoretical efficiency ($\tilde{\eta}_{\mathrm{t}}$) obtained for shielding with the reference and aegises by fitting the plots in Figure 5a, c and d.

Aegis	ΔT_∞ (°C)	τ (s)	t_0 (s)	h (mW K^{-1})	η_{exp} (%)	η_{t} (%)	$\tilde{\eta}_{\mathrm{t}}$ (%)
Reference	47.1	1031	23	[a] 0.162	0	0	[b] 0
PS-CA	44.0	1064	20	[a] 0.158	6.6	12.6	[b] 9.4
PVK-CA	41.0	1137	15	[a] 0.147	13	20.7	[b] 13
PVK-AQ	34.3	1192	29	[a] 0.141	27	37.5	[b] 30

[a]h is calculated as per Equation 4b, known water mass to be 40,0 g and its specific heat 4.196 J g-1 K-1; [b] $\tilde{\eta}_t$ is calculated as per Equation 5 from the theoretical efficiencies ηt and h coefficients here reported.

3.2.7. Irradiation at non normal incidence. All these efficiencies and considerations commented so far were obtained nominally at normal incidence, as the aegis was perpendicular to the focusing cone's axis (see **Figure 3.6**). Calculations based on **Equation 3.4** suggest that, for unpolarized light, aegises' theoretical efficiency at an angle is only slightly reduced with respect to the normal when light rays impinge at angles between 20° and 60°, then rises sharply after 60° (**Figure 3.8f,** black curve). This follows the behavior of Fresnel's coefficients, with p-polarized reflectance dropping down with angle (pink curve) and s-polarized reflectance steadily growing (green curve).[10, 17, 18]

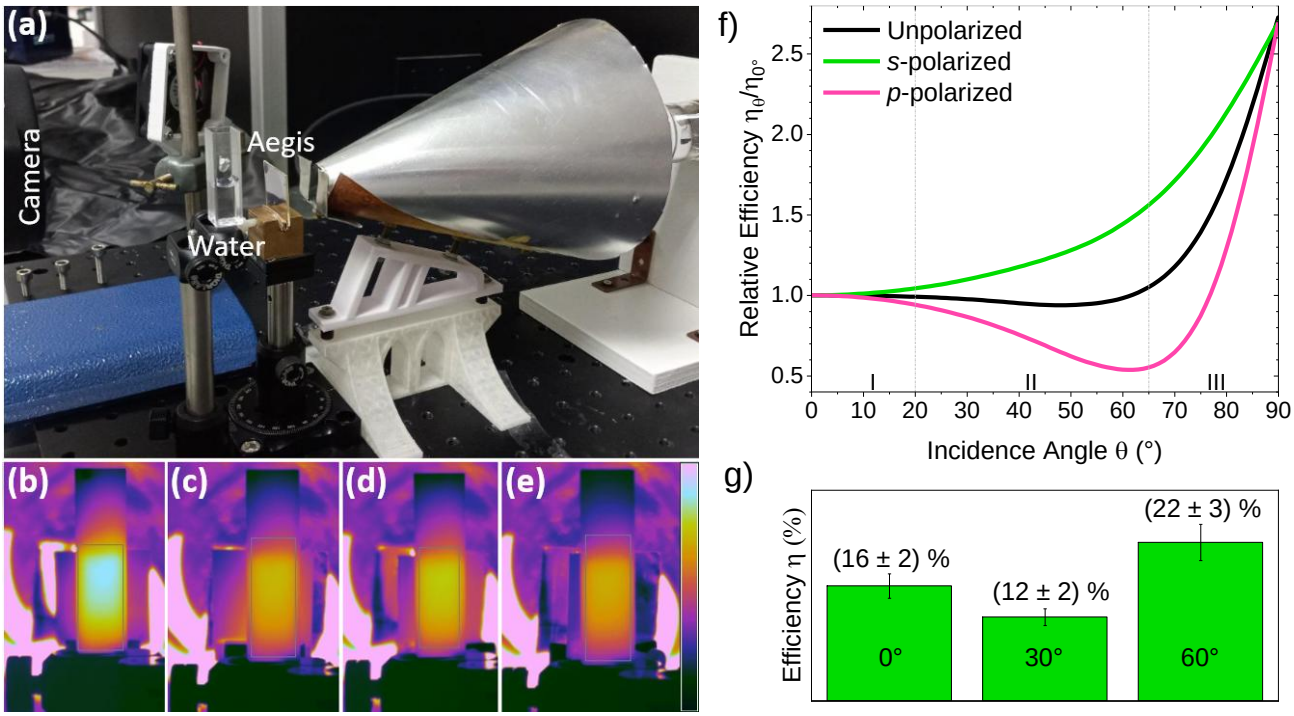

Figure 3.8. **a)** *Picture of the setup used to test aegises' angular dispersion.* **b, c, d, e)** *Thermal images after 20 min of heating when the water is shielded by the glass reference (b) or the PVK-CA aegis tilted by 0° (c), 30° (d) or 60° (e) respectively. Color scale is 25 to 55 °C.* **f)** *calculated relative efficiency of the PVK-CA aegis for incidence angles between 0 and 90°, divided in three main sections (I, II and III).* **g)** *Measured efficiencies for PVK-CA aegis as derived from c, d and e, for angle of 0, 30 and 60° respectively.* Reproduced from [1]

Experimentally, I modified the setup allowing for the aegis to be rotated slightly to study the effect of non normal incidence, as represented in **Figure 3.8a**. The temperature at various angles were recorded with the thermal camera, as reported in Figure 3.8b-e; Figure 3.8b represent the reference, whereas c-e represent the aegis rotated by 0, 30 and 60 °C respectively. From the thermal cameras by naked eye differences are not obvious, but extracting the efficiency in each case yields the values

represented in the bar plot of **Figure 3.8g**. In this regard, I only observed a limited decrease between 0° and 30°, and a consistent rise in efficiency at 60° (**Figure 3.8g**). This is probably due to the light exiting focusing cone at different angles, altering the effective angle of incidence from the nominal one.

3.3. Conclusion

Together with the results reported in **Chapter 2**, the use of all-polymer DBRs (aegises) for thermal shielding has been studied in-depth, investigating both the effect of structures and materials on their efficiency in reducing heating from irradiation. In the first chapter, I presented the preliminary results and the study of different structures, alongside the shielding of different materials; in this second work, I provided more insight into polymer aegises, especially on the modeling and theoretical prediction of their efficiency as well as on the influence of material composition on the aegises' efficiency. An improved design rationale for aegises was defined to optimally reflect NIR light for the desired application. This rationale considers the spectrum of the incident light, the absorption spectrum of the material to shield and the aegises' optical response, being it more quantitative with respect to the spectral coverage initially defined. As a proof-of-concept, three identical spin-coated multilayer structures, formed by sixty-five layers each, were fabricated out of different polymer pairs bearing increasing dielectric contrast, ranging from 0.11 up to 0.27. This way, I demonstrated how switching the building blocks of the same, simple structure from commodity polymers like PS and CA ($\Delta n = 0.11$) to more specialized ones like PVK and AQ ($\Delta n = 0.28$) can rise the efficiency from 6.6 % up to 27 % in shielding water. I demonstrate that in the NIR region beyond 1200 nm, it is not possible to obtain aegises with both high shielding efficiency and perfect visible range transparency. A colored metallic sheen is indeed unavoidable, even though this can be an upside in certain applications joining aesthetics and functionality. As I shown how the use of specialty polymers adds to the increase of efficiency in passive thermal shielding yields a consistent material saving, I believe the research on aegises could lead to improvements in our energy efficiency and towards the goal of a sustainable human presence on Earth. From this point forward, the focus of the work about thermal management shifted towards the application of another principle, thoroughly described in the next chapter – radiative cooling.

Bibliography

1. A. Lanfranchi, H. Megahd, P. Lova , D. Comoretto. *Chem. Eng. Sci.*, **283**, 5, 119377, (**2024**)

2. E. Akpinar-Ferrand , A. Singh. *Environ. Sci. Policy*, **13**, 8, 702, (**2010**)

3. K. L. Kownacki, E. D. Hornyanszky, T. A. Chu, J. A. Olsson , P. Becker. *Int. J. Biometeorol.*, **62**, 3, 401, (**2017**)

4. M. E. Hossain, S. Rej, S. M. Saha, J. C. Onwe, N. Nwulu, F. V. Bekun , A. Taha. *Sustainability*, **14**, 13, 7537, (**2022**)

5. A. Lanfranchi, H. Megahd, P. Lova , D. Comoretto. *ACS Appl. Mater. Interfaces*, **14**, 12, 14550, (**2022**)

6. Z. Zhang, C. Liu, X. Chen, C. Zhang , J. Chen. *Appl. Thermal Eng.*, **125**, 567, (**2017**)

7. S. Hemming, F. Kempkes, N. van der Braak, T. Dueck , N. Marissen. *Acta Hortic.*, 97, (**2006**)

8. P. Lova, G. Manfredi , D. Comoretto. *Adv. Opt. Mater.*, **6**, 24, 1800730, (**2018**)

9. P. Lova, V. Grande, G. Manfredi, M. Patrini, S. Herbst, F. Würthner , D. Comoretto. *Adv. Opt. Mater.*, **5**, 21, 1700523, (**2017**)

10. H. A. MacLeod, *Thin-Film Optical Filters.* CRC Press, Boca Raton, FL, USA, **2018**

11. Solvay, Aquivion, https://www.solvay.com/sites/g/files/srpend221/files/2018-08/Aquivion-PFSA-Solid-Perfluorinated-Superacid-Catalysts_EN-v1.1_0.pdf (accessed December, 2024)

12. K. Matyjaszewski, *Encyclopedia of Polymer Science and Technology.* John Wiley & Sons, Inc., **2002**

13. P. Lova, H. Megahd, P. Stagnaro, M. Alloisio, M. Patrini , D. Comoretto. *Appl. Sci*, **10**, 12, 4122, (**2020**)

14. G. Manfredi, P. Lova, F. Di Stasio, R. Krahne , D. Comoretto. *ACS Photonics*, **4**, 7, 1761, (**2017**)

15. H. Megahd, C. Oldani, S. Radice, A. Lanfranchi, M. Patrini, P. Lova , D. Comoretto. *Adv. Opt. Mater.*, **9**, 5, 2002006, (**2021**)

16. S. V. Radice, P. Sriniviasan, D. Comoretto, S. Gazzo, *One-dimensional planar photonic crystals including fluoropolymer compositions and corresponding fabrication methods.* WO 2016/087439 Al (**2016**)

17. G. Giusfredi, *Mauale di Ottica.* Springer, Milano, **2015**

18. M. C. T. Bahaa E. A. Saleh, *Fundamentals of Photonics.* John Wiley & Sons Inc., **2019**

19. F. P. Incropera, D. P. DeWitt, T. L. Bergman , A. S. Lavine, *Fundamentals of Heat and Mass Transfer.* John Wiley & Sons, Hoboken, NJ, USA, **2006**

20. J. E. Bertie , Z. Lan. *Appl. Spectrosc.*, **50**, 8, 1047, (**1996**)

21. H. W. Siesler, Y. Ozaki, S. Kawata , H. M. Heise, *Near-Infrared Spectroscopy: Principles, Instruments, Applications.* Wiley-VCH, **2001**

22. H. Song, K. Singer, Y. Wu, J. Zhou, J. Lott, J. Andrews, A. Hiltner, E. Baer, C. Weder, R. Bunch, R. Lepkowicz , G. Beadie, *Layered polymeric optical systems using continuous coextrusion*. From SPIE Optical Engineering + Applications, San Diego, CA, USA, **2009**

23. A. Aili, Z. Y. Wei, Y. Z. Chen, D. L. Zhao, R. G. Yang , X. B. Yin. *Mater. Today Phys.*, **10**, 100127, (**2019**)

24. J. Workman , L. Weyer, *Practical Guide and Spectral Atlas for Interpretive Near-Infrared Spectroscopy.* CRC Press, Boca Raton, Florida, USA, **2012**

25. E. M. A. Khalil, F. H. ElBatal, Y. M. Hamdy, H. M. Zidan, M. S. Aziz , A. M. Abdelghany. *Physica B: Condensed Matter*, **405**, 5, 1294, (**2010**)

26. Reference Air Mass 1.5 Spectra, https://www.nrel.gov/grid/solar-resource/spectra-am1.5.html (accessed December, 2024)

27. K. D. Singer, T. Kazmierczak, J. Lott, H. Song, Y. Wu, J. Andrews, E. Baer, A. Hiltner , C. Weder. *Opt. Express*, **16**, 14, 10358, (**2008**)

Chapter 4 – Polymer Photonics for Radiative Cooling

Abstract

Radiative cooling fits in the general frame of thermal management, being a passive option of cooling down bodies even below ambient temperature in certain situations. The phenomenon exploits the thermal radiation spontaneously emitted by bodies in the atmospheric transparency region, the 8-13 μm wavelength range where the Earth's atmosphere is relatively transparent. Electromagnetic radiation emitted in this region will pass through the atmosphere and be lost in the void of space, effectively granting a net cooling flow in a completely energy-free manner.

In this Chapter, after a general introduction, I report the modeling of the phenomenon, going from equations to the Matlab code I wrote to predict the effect for different materials. I also present some general considerations upon the calculations as far as the different types of ideal radiative coolers (narrowband and broadband) are concerned. Afterwards, I report on the challenges of building the necessary setup to observe the phenomenon, investigating the nuances of the measurements. I then introduce the nonsolvent-induced phase separation method for the fabrication of white polymer diffusers, in my case made of either cellulose acetate or recycled poly(vinyl chloride). Preliminary results on poly(vinyl chloride samples) are presented, attaining sub-ambient cooling. The samples of cellulose acetate are instead fully characterized optically and their performances in radiative cooling applications evaluated and comparing with the theoretical values, obtaining good results; follow-up to this research would be integrating aegises reflecting in the Visible-Near Infrared range to enhance the cooling efficiency.

4.1. Introduction

As stated in the previous chapters, the issue of global warming is increasingly worrying, with its main solution (air conditioning systems) being instead more part of the problem. [1-3] Therefore, there is a strong need for passive solutions able to complement air conditioning or to replace it altogether without the related energy consumption and heat and CO_2 emissions.[1, 3] In this regard, I demonstrated how distributed Bragg reflectors (DBRs) made out of polymer materials can perform as effective aegises, able to reflect the NIR radiation which causes the heating of indoor environments without losing transparency in the visible range; this could be especially useful for buildings and cars windows, and for greenhouses in the form of removable plastic films. I investigated the effect of both structures using single aegises, tandem and superperiodic ones,[4] as well as the effect of materials and dielectric contrast using cheap polymers such as polystyrene and cellulose acetate (CA) as well as technical ones such as poly(*N*-vinylcarbazole) and Aquivion.[5]

However, as briefly mentioned in the introduction to **Chapter 2**, there is another promising method which can be associated to thermal shielding to reduce the need for energy-inefficient air conditioning: radiative cooling (RC).[6, 7]

Imagine a schematic situation such as that represented in **Figure 4.1a**; a body, for example a *Tyrannosaurus Rex,* is placed in a field, under the clear sky. The body will exchange energy with its surroundings.[8] Let us neglect the absorption of sunlight (yellow arrow) for the moment. Convection and conduction (black arrow) will either cool down the body or heat it up, depending on its temperature with respect to the surrounding air. The body will then emit electromagnetic radiation due to Planck's Law (**Chapter 3**, **Equation 3.5**), irradiating heat towards the outside (blue arrow). On the other hand, the surroundings will emit thermal radiation according to their temperature, part of which will be absorbed back by the body (red arrow). Were the atmosphere a blackbody, this exchange of thermal radiation would bring the body at the same equilibrium temperature. However, the atmosphere is not a blackbody; indeed, radiation emitted by the body between 8 and 13 μm is transmitted through it and lost in the cold emptiness of space (2.7 K). This way the body effectively loses heat, cooling down to a temperature lower than surrounding air ("subambient cooling").[9-11] Typical atmospheric transmittance spectra are reported in **Figure 4.1b** for different climate regions of Earth, with the atmospheric transparency window highlighted in light blue. The curves were obtained with the software MODTRAN (see **Appendix B.4.1** for more details). Climate region and seasons have a great effect on the transparency of the atmosphere due to the amount of water vapor, with tropical regions and mid latitudes during summer (red and blue curves respectively) being less transparent than mid latitudes during winter (green curve) and sub-arctic deserts being extremely

transparent. In this chapter I will use the mid-latitude summer model, more representative of the conditions of Genoa.

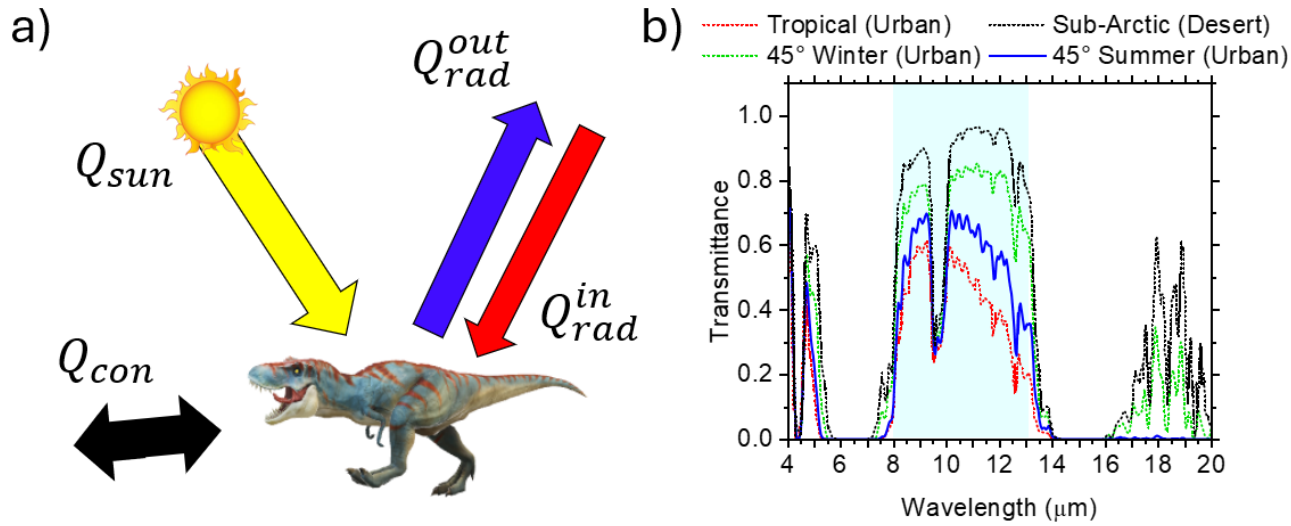

Figure 4.1 a) *Schematics of the energy balance of a body during the process of radiative cooling.* **b)** *Atmospheric transmittance spectra for different climatic models. 45° Summer (Urban) is the model used in the calculations presented in the chapter.*

4.1.1. Modeling radiative cooling. A first step towards the understanding of the phenomenon is implementing a complete model to describe it. There are mainly three different approaches to radiative cooling modeling; for the full description and comparison of the three I recommend the review by Zhao et al., *Appl. Energy* 2019,[8] on which the following description is based. In my case, I adopted the so called spectral dependent, directional dependent model.

Referring to the schematics represented in **Figure 4.1a**, the equation regulating the power balance of the body is the following:

$$Q_{tot} = Q_{rad}^{out} + Q_{rad}^{in} + Q_{con} + Q_{sun} \tag{4.1}$$

There, Q_{tot} is the total power absorbed (or emitted) by the body per unit time, Q_{con} is the heat per unit time exchanged via conduction and convection, Q_{sun} is the absorption of sunlight. $Q_{R,out}$ and $Q_{R,in}$ are respectively the heat radiated from the body to its surroundings and vice versa. The term Q_{con} is directly proportional to the exchange area A_c and the temperature difference between RC (T_{RC}) and surroundings (T_{atm}):

$$Q_{con} = Q_{conv} + Q_{cond} = A_c h_c \, (T_{RC} - T_{atm}) \tag{4.2}$$

Note that the proportionality factor h_c is not the same reported in Chapter 2 as here radiation is excluded and only conduction and convection are included.

The sunlight absorbed by the RC, Q_{sun}, can be obtained through a simple integral, known the surface exposed to sunlight A_r and the spectral irradiance (energy per unit time, per unit area and per unit wavelength) coming from sunlight I_{sun} at an angle ψ from the surface normal:[11]

$$Q_{sun} = \cos\psi \, A_r \int_0^{\infty} I_{sun}(\lambda) \, \alpha_{RC}(\psi, \lambda) \, d\lambda \tag{4.3}$$

Note that the areas for conduction/convection and radiation are $A_c \cong A_r$, hypothesizing the cooler is flat, thin and its back insulated. How much of I_{sun} gets absorbed at each wavelength depends on the body's absorptivity, a dimensionless parameter, wavelength-dependent and angle-dependent (though angle dependency can be neglected as first approximation).[12] Absorptivity's value is $0 < \alpha_{RC} < 1$, a value of 1 meaning the body is a perfect absorber, a value of 0 meaning no light is absorbed. This is related to the RC's reflectance R_{RC} and transmittance τ_{RC} by conservation of energy:

$$R_{RC}(\lambda) + \tau_{RC}(\lambda) + \, a_{RC}(\lambda) = 1 \qquad \forall\lambda \tag{4.4}$$

Which holds immediate significance in real-life scenarios: metals with their high reflectance and low transmittance are poor absorbers of radiation, whereas a piece of black paper, which reflects only slightly and has a low transmittance, is a very good absorber. The absorptivity a_{RC} can be related to the absorption coefficient α of the material making up the RC; including Beer-Lambert's law for the transmittance of a body with thickness d, the relationship is:

$$a_{RC}(\lambda) = 1 - R_{RC}(\lambda) - e^{-\alpha(\lambda)d} \tag{4.5}$$

Therefore, the absorptivity of a body closely mimics its absorption spectrum, and the final value of absorptivity depends on the thickness of material considered.

Now, the thermal emission relative to the RC is slightly more complex than **Equation 3.2**:

$$\begin{aligned} Q_{rad}^{out} &= A_r \int_0^{\infty} \int_0^{2\pi} \int_0^{\frac{\pi}{2}} \varepsilon_{RC}(\lambda, \vartheta, \varphi, T_{RC}) \, B_{RC}(\lambda, T_{RC}) \cos\vartheta \sin\vartheta \, d\varphi \, d\vartheta \, d\lambda \\ &\cong A_r 2\pi \int_0^{\infty} \int_0^{\frac{\pi}{2}} \varepsilon_{RC}(\lambda) \, B_{RC}(\lambda, T_{RC}) \cos\vartheta \sin\vartheta \, d\vartheta \, d\lambda \end{aligned} \tag{4.6}$$

$B_{RC}(\lambda, T_{RC})$ is the spectral radiance emitted by the body as per Planck's law. ε_{RC} is a dimensionless parameter $0 < \varepsilon_{RC} < 1$, called the emissivity; it stands as the ratio between the RC's emission with respect to that of a blackbody. This parameter is in principle dependent on angles, wavelength and temperature; however, the dependence on azimuthal angle can usually be neglected leading to a 2π coefficient, as well as the dependence on temperature. Assuming the RC is a Lambertian emitter (which is the most severe approximation) uniform in all directions, its angular dependence can be ignored as well.[12]

Even though this may sound odd, this emissivity parameter is none other than the absorptivity; the two parameters are the same for each wavelength, as stated by Kirchoff's law of thermal radiation:

$$\varepsilon_{RC}(\lambda) = \ a_{RC}(\lambda) \qquad \forall\lambda \qquad (4.7)$$

This stems from the theory about blackbody emission and holds true for any wavelength;[6, 12, 13] since thermal emission for bodies at ambient temperature is peaked around 10 μm (or 1000 cm^{-1}), efficient IR absorbers are good emitters of thermal radiation, and each absorption peak seen in a typical FTIR spectrum of a substance will be a preferential wavelength for its thermal emission.[12, 14] This may seem counterintuitive, especially since the demonstration involves the use of a box filled with a photon gas in thermal equilibrium with the walls, which is not easily translated to a real-life case.[13, 15]

The energy the RC receives through radiation is instead:

$$Q_{rad}^{in} = A_r \pi \int_0^{\infty} \int_0^{\frac{\pi}{2}} \varepsilon_{atm}(\lambda, \vartheta)\ a_{RC}(\lambda)\ B_{atm}(\lambda, T_{atm})\ sin\, 2\vartheta\ \ d\vartheta\ d\lambda \qquad (4.8)$$

This is essentially **Equation 3.6** calculated with respect to the atmosphere; it contains atmospheric emissivity and Planck's spectral irradiance calculated for atmosphere temperature. Additionally, since it represents the radiation absorbed by the RC, it includes its absorptivity (which, as we have discussed, is equal to its emissivity $\varepsilon_{RC}(\lambda)$). The directional emissivity of the atmosphere can be interpreted in different ways, but following Raman et al. *Nature* 2014:[6]

$$\varepsilon_{atm}(\theta, \lambda) = 1 - (\tau_{atm}(\lambda, 0))^{1/\cos\theta} \qquad (4.9)$$

Where τ_{atm} is the transmittance of the atmosphere at normal incidence.

In principle, plugging **Equations 4.8**, **4.6**, **4.3** and **4.2** into **4.1** yields the thermal balance of the RC. In practice, the integrations of **Equation 4.8**, **4.6** and **4.3** must be numerically performed; doing so and letting $Q_{tot} = 0$ yields the final equilibrium temperature of the RC.

4.2. Results & Discussion

4.2.1. Implementation of the model and example cases. The model described so far was integrated into a MatLab code to predict the radiative cooling performances of samples. As the first steps for the project, I made thorough calculations using the model to calculate the cooling performances of RCs with different characteristics in different conditions. Indeed, considerations along these lines are quite limited and information is fragmented in literature, therefore I needed to implement the model to have a complete understanding of the problem.

Consider an ideal RC with an emissivity represented by the orange line of **Figure 4.2a**. This emission is a square wave-like plateau centered at 10.9 μm, 0.8 μm bandwidth. It takes value 0.96 on top and 0 everywhere else; this RC is an ultra-narrowband emitter. The emissivity is then increased progressively until the plateau fits the 8-13.2 μm spectral region (narrowband emitter, magenta line) and then increased again until it reaches 4-50 μm (broadband emitter, green line). Comparing these emissivities with the ideal transmittance of the atmosphere at normal incidence (**Figure 4.2a**, blue line),[16] the difference between the various ideal situations; the ultra-narrow emitter is centered in the point of lowest emissivity (highest transmittance) of the atmospheric transparency window, the narrow one exactly covers the whole window, whereas the broadband one covers the transparency window and extends further beyond. Intuitively, the ultra-narrowband and narrowband emitter should exchange less energy with the atmosphere, dissipating almost all their emitted heat into the void of space and receiving none in return. Broadband has a greater gross output of heat, but most of it is exchanged directly with the atmosphere. Let us neglect sunlight as in all three conditions **Equation 4.3** yields, $Q_{\text{sun}} = 0$since $\varepsilon_{\text{RC}} = a_{\text{RC}} = 0$ for the wavelength range containing 99 % of solar radiation on Earth (300-2500 nm).[7, 17, 18]

To give a better understanding of the quantities Q_{rad}^{in} and Q_{rad}^{out}, **Figures 4.2b-c** report their calculations. Q_{rad}^{out} for a broadband emitter (at normal incidence, neglecting angular integration) is represented by the red area under the curve in **Figure 4.2b**. The curve itself is the quantity $\varepsilon_{RC}(\lambda)\, B_{RC}(\lambda, T_r)$ calculated for a body at $T_{RC} = 300$ K. The whole representation, enclosed in dotted lines, is relative to a broadband RC; narrowband and ultra-narrowband ones would need to truncate both **Figures 4.2b-c** in correspondence to the dashed-dotted and the solid line respectively.

Q_{rad}^{in} is instead represented by the blue area in **Figure 4.2c**, that is $\varepsilon_{RC}(\lambda)\varepsilon_{atm}(\lambda)B_{atm}(\lambda, T_{atm})$. The temperature of the atmosphere is assumed to be $T_{atm} = 300\,\mathrm{K}$. There, the effect of the atmospheric transparency window is apparent, as a noticeable dip in the curve due to the reduced atmospheric emission in that spectral region.

The difference between the two curves is, at normal incidence, the absolute value of the difference $Q_{rad}^{out} - Q_{rad}^{in}$; since $Q_{rad}^{out} > Q_{rad}^{in}$ the radiative balance of the body would lead to a net cooling with respect to the atmosphere. The heat difference is dissipated through the atmosphere into space and lost forever.[2]

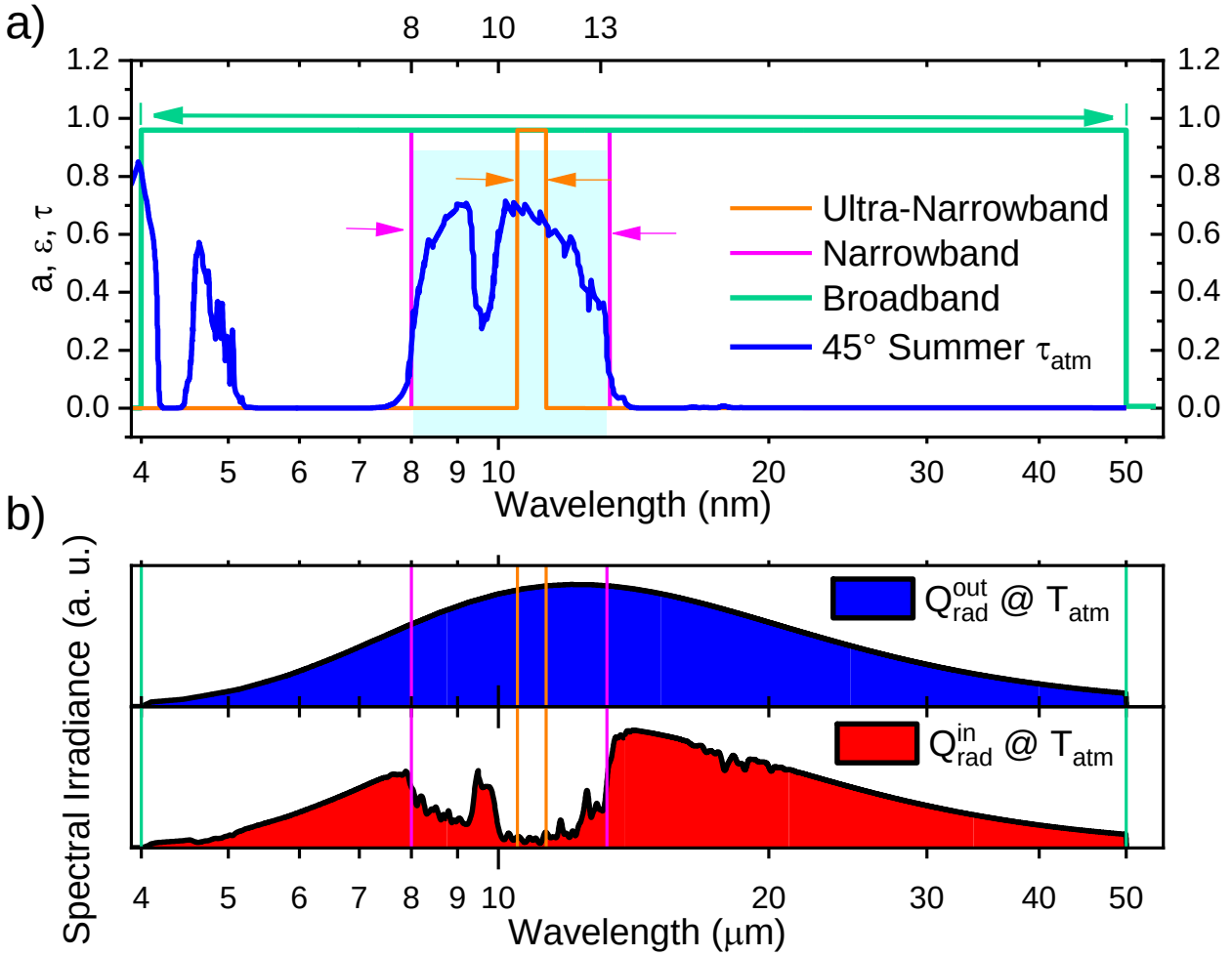

Figure 4.2. **a)** *Atmospheric transmittance for mid-latitudes summer in an urban environment (blue line), superimposed to the emissivity/absorptivity of three ideal RCs: broadband (green line, bandwidth 4-50 μm indicated by the green arrow), narrowband 8-13.2 μm (magenta line, magenta arrows), ultra-narrowband 10.1-11.7 μm (orange line, orange arrows);* **b)** *Heat emitted by the RC (red area) and heat received back from the atmosphere (blue area) at normal incidence.*

[2] This easily explains the effect of greenhouse gases on Earth's temperature (the "radiative forcing"). Indeed, they improve the absorptivity/emissivity of the atmosphere and reduce its transmittance, leading to a less pronounced dip in the atmospheric emission (**Fig. 4.2c**). Overall, the Earth dissipates less energy into space and heats up more.

Equation 4.1 was calculated for different values of temperature of the RC and the three main emission bandwidths (ultra-narrowband, narrowband and broadband), as well as any intermediate emission bandwidth. The net power outputs are reported in **Figure 4.3a** as a 3D plot. On the X axis, the difference between the current temperature of the RC and the temperature of the atmosphere is reported. On the Y axis, the width of the emissivity plateau (that is, for example, 0.8 µm for the ultra-narrowband, 5 µm for the narrowband and 55 µm for the broadband RCs respectively). On the Z axes, the net power output of a determined RC set at a certain temperature. The plot must be interpreted this way: where $Q_{tot} < 0$ (cyan region) the body tends to cool down ("climbing" the slope along the X axis); vice versa, where $Q_{tot} > 0$ (orange region) the body heats up ("falling" down the slope along the X axis). This continues until equilibrium is reached ($Q_{tot} = 0$, black line centered in the white region). Figure 4.3b reports the equilibrium values reached by each emitter (it is effectively the intersection of the surface of **Figure 4.3a** with the XY plane). Here, the difference between the profiles is apparent; the equilibrium temperature reached is progressively lower for broadband, narrowband and ultra-narrowband emitter. This happens because the body can reach a lower temperature the lower is its radiative exchange with the atmosphere (a proportionally greater amount of the RC's thermal emission is dissipated into space). The solid, dashed-dotted and dotted line mark the three ideal situations of ultra-narrowband, narrowband and broadband RCs. This situation seems to strongly favor ultra-narrow and narrowband emitters, with temperature reaching as low as -40 °C/-32°C with respect to ambient in the two cases, compared to -10 °C for the broadband one.

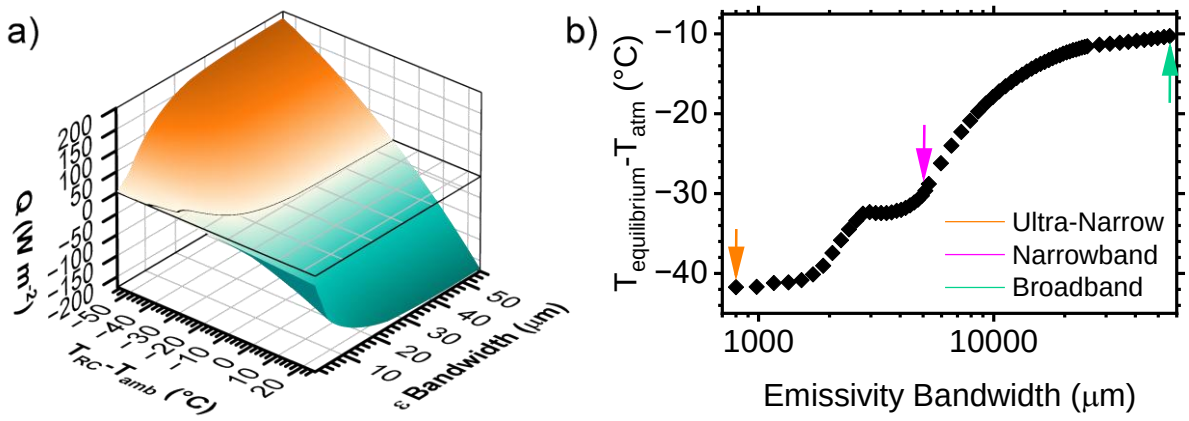

Figure 4.3. a) *3D plot representing the net power emitted by an RC with emissivity 0.96 in an interval λ_2 - λ_1 centered on the transparency window at each temperature. Cyan color indicates the body would cool down, orange color that the body would heat up, until reaching the net zero (white section, black line). b) equilibrium temperature reached by RCs with progressively larger high-emissivity plateaus. Arrows indicate the main modeling situations (orange, ultra-narrowband emitter; magenta, narrowband emitter; green, broadband emitter).*

However, it must be noticed from **Figure 4.3a** that the net power emitted for temperatures out of equilibrium is progressively greater. This means that additional heat sources will affect proportionally more the narrowband ultra-narrowband emitters with respect to the broadband one.

This comes into play if any other source of energy is added –sunlight, conduction or convection from ambient air. Even adding a moderate convection from ambient air, equivalent to $h = 5\ W\ m^{-2}K^{-1}$ (see **Equation 4.2)**, the cooling phenomenon is completely different. Indeed, **Figure 4.4a** reports the equilibrium temperature reached by coolers with different emissivity bandwidths. The difference with respect to **Figure 4.3b** is apparent; the ultra-narrowband RC is no longer the best option to sustain sub-ambient cooling, getting replaced by the narrow one. On the other hand, the difference between the narrowband and broadband profiles is relatively low, passing from around -8 °C to -5 °C degrees with respect to the atmosphere.

The effect of sunlight is simpler but striking; since Q_{sun} does not depend on ambient temperature, its addition shifts the surface in **Figure 4.3a** upward by the corresponding amount. Notice the Z scale of **Figure 4.3a**; considering sunlight yields around 1000 W m^{-2}, five times the highest output value, it is apparent that even relatively low absorption will profoundly influence the equilibrium temperature. Indeed, adding an absorption of 5 % of sunlight (which corresponds to setting the absorptivity/emissivity of the RC to 0.05 in the 300-4000 nm wavelength range) to the *h* coefficient of 5 W K^{-1} m^{-2} yields the result represented in **Figure 4.4b**. In this case, the ultra-narrowband RC completely fails to achieve sub-ambient cooling. On the other hand, the effect of narrowband remains greater, but the difference with respect to the broadband one is very low, a few fractions of degrees. An obvious implication of these data is that the radiative cooling performance will inevitably depend on the season of the year and the precise amount of sunlight the RC is getting.

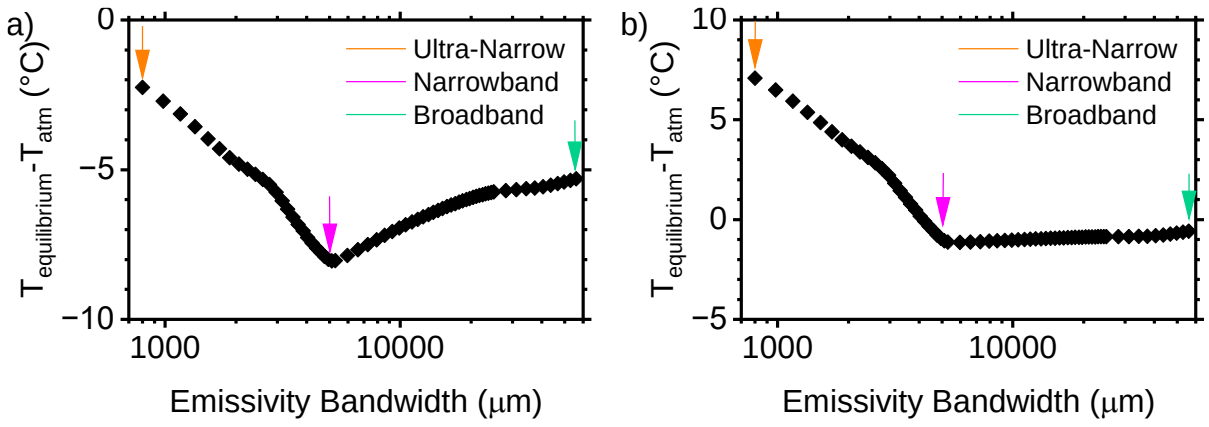

Figure 4.4. *Equilibrium temperature reached by RCs with progressively larger high-emissivity plateaus.* **a)** *Convection h = 5 W K^{-1} m^{-2}, solar absorptivity = 0;* **b)** *Convection h = 5 W K^{-1} m^{-2}, solar absorptivity = 0.05 (5 %). Arrows indicate the main modeling situations (orange, ultra-narrowband emitter; magenta, narrowband emitter; green, broadband emitter).*

From this, some general considerations can be pulled out. Indeed, depending on the exact needs of the application, the broadband RC may be preferrable to the narrowband one. Whenever an external energy source is heating the system above ambient temperature, the broadband RC lowers the temperature more efficiently due to greater power output. This is important for example in solar cells, that reach a temperature well above ambient due to their absorption of sunlight (necessary to their functioning); in this case broadband reflectors are more effective. Where narrowband (or even ultra-narrowband) emitters really shine is situations where the RC is perfectly insulated and completely reflective; this allows them to reach temperatures well below those attainable by a broadband RC. Of course, the more sunlight is reflected, the better each cooler perform; over 6-7 % absorption of sunlight in AM1.5G conditions, sub-ambient cooling is no longer observable.

The main problem for narrowband emitters in widespread, common applications such as roofing is that they do not really exist – often, substances either have an optical response halfway between narrowband and ultra-narrowband, or a mixed emissivity partly covering the transparency window while having additional peaks outside it.[14] However, every bit of emission lost in the transparency window decreases the effectiveness of the RC, so much so that in non-ideal conditions with consistent convection/conduction and greater-than-zero absorption of sunlight, broadband emitters are generally preferred.

In these regards, polymers are well suited to radiative cooling, as most of them do not present important absorptions in the visible range and only show minor ones in the near-infrared range. Hence, they are poor absorbers of sunlight. As far as emission is concerned, they are diverse and versatile; they can be poor or excellent emitters thanks to the variety of bonds and vibrational modes and the possibility of loading them with charges. C-Cl and especially C-F moieties are emitting in the atmosphere transparency region, making halopolymers such as poly(vinyl chloride) or poly (vinyl denefluoride) good choices as narrowband emitters.[19, 20] Other polymers such as cellulose acetate tend to perform as broadband emitters.[10, 21] Polymers are easy to load with inorganic charges as well, which can emit in the atmosphere transparency region or increasing the reflectance, making extremely selective reflectors when choosing polymers which are poor emitters by themselves such as polyethylene.[8, 9, 19, 20]

4.2.2. Assembling an experimental setup. Before following up with the design and fabrication of polymer structures for radiative cooling, I will report on the challenges of building a reliable measurement apparatus. Following results reported in literature,[6, 8, 11, 21, 22] the first setup was quite simple – two chambers carved out of polystyrene foam, covered by a polyethylene film acting as

convection field. In principle, cutting off as much as possible the h_C coefficient of **Equation 4.2** is beneficial to radiative cooling, hence the insulation from conduction and convection. The same PC-linked thermometer reported in Chapters 2-3 was used to measure the temperature of the samples inside the chambers through a small opening in the walls.

The tests performed outside, in shadow, resulted in the test materials achieving sub-ambient cooling. However, the tests under sunlight yielded very high temperatures – an order of magnitude more than what could be predicted using the model presented in this Chapter. Presumably, the chambers of this first setup were too big with respect to the sample size, offering too much inner surface to heat up under sunlight. As seen in **Figure 4.3a**, the cooling power of the RC is relatively low in any case. Therefore, it cannot counterbalance the greater surface absorbing sunlight and heating up. Following these considerations, the design was revised and improved as represented in **Figure 4.5a**. To do so, I designed and 3d-printed a small chamber out of an acrylate resin which I painted with a brilliant white finish, fit to size to hold the sample. The chamber had a hole for the thermistor, and it was fitted in an expanded polystyrene cube covered in aluminum foil on top. The polyethylene shield was used also in this case. **Figure 4.5b** reports the curve measured with the setup, using a white cellulose acetate sample (see **Subsection 4.2.4**). Under sunlight the temperature reached is still one order of magnitude greater than expected.

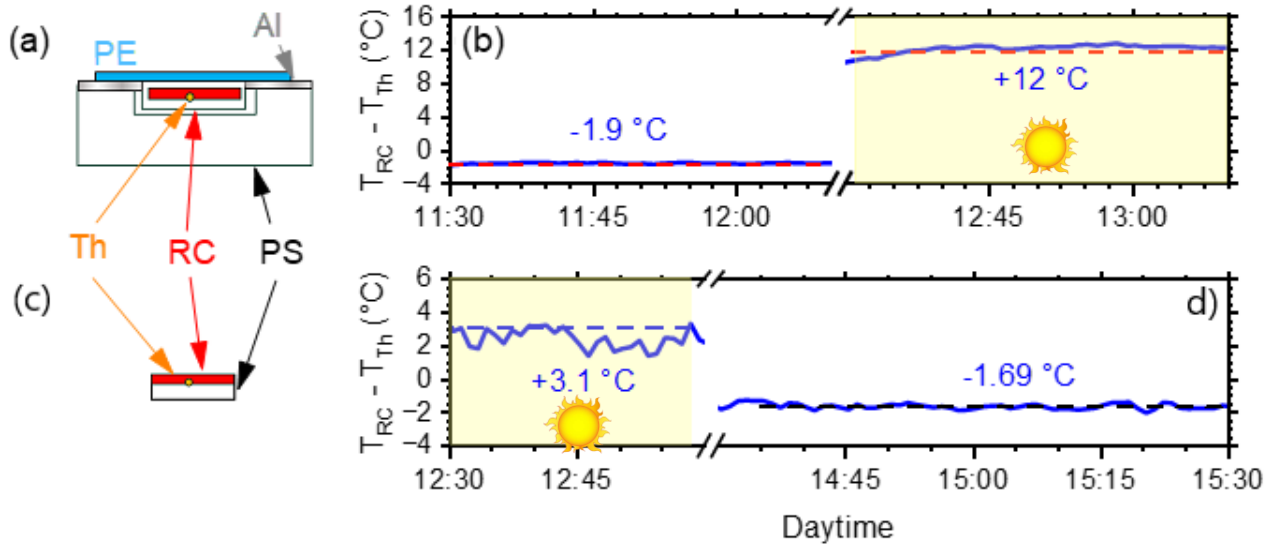

Figure 4.5. **a)** *Schematic representation of the enclosed setup to observe radiative cooling.* **b)** *Equilibrium temperature reached by a cellulose acetate sample in the shadow and under sunlight with the setup in* **(a)**. **c)** *Schematic representation of the front-open, back-insulated setup.* **d)** *Equilibrium temperature reached by a cellulose acetate sample in the shadow and under sunlight with the setup in* **(c)**.

At this point, it was apparent that the approach was not viable. Indeed, either the materials making up the setup are completely nonabsorbent, but in that case it they would be better candidates for

radiative cooling than the actual samples, or all the surfaces available should be covered with the sample. The latter approach was chosen as remarkably similar to the final application conditions. Indeed, roofing materials cannot be insulated from convection and conduction happening on the outside surface and our idea was not to develop an ultra-narrow RC. As represented in **Figure 4.5c**, I attached the sample on top a polystyrene block, leaving room to measure its temperature with the thermistor. This way, the setup is free to exchange energy from the front, whereas it is insulated from the back to insulate the thermistor from direct conduction/convection. The results are reported in **Figure 4.5d**, both under direct sunlight and in the shadow. The difference with the box-setup case is striking, as the temperature reached by the sample under sunlight is almost 10 °C lower.

The first iterations of the setup were cumbersome and required the use of a PC using the application of the thermometers. This was strict and impeded making the measurements for prolonged time away from the power grid or outside in non-ideal weather conditions. I therefore designed an integrated platform to easily perform the measurements.

The final form of the setup I designed and assembled is represented in **Figure 4.6a** and schematized in **Figure 4.6b**.

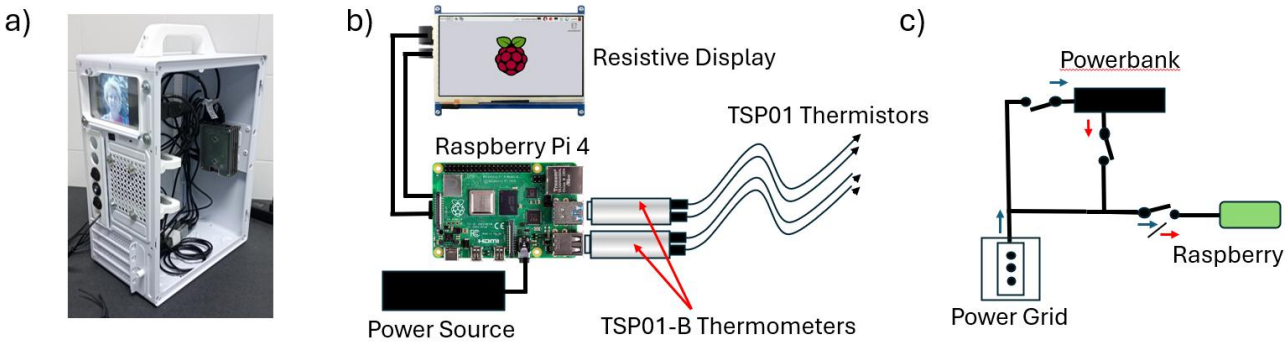

Figure 4.6. a) *Picture and* **b)** *schematic of the final setup for radiative cooling measurements;* **c)** *schematic of the electrical connections for powering up the systems (blue arrows, current from the power grid; red arrows, current from the power bank).*

A portable, small size microcomputer replaces the PC used for the first measurements. Since the new device works better in Linux based environments whereas the thermometers do not by default, it was necessary to install the appropriate libraries and drivers and I programmed a Python3 code to extract data from the thermometers through standard USB communication. The setup is encased in the case of a mini-PC integrated with CAD-assisted designed and 3d-printed parts for the attachment of the other parts. The main bodies of the thermometers and the microcomputer were attached inside. A touch screen is added to the system to provide visual output and measurement control as well as input. The touch screen is resistive to avoid its interaction with humidity and water ruining the

responsivity – in principle, this is enough to perform the measurements, but a keyboard can be added to the system if needed. Additionally, the microcomputer can be remotely operated via a PC through the use of an SSH server connection. Additional details are reported in **Appendix B.4.2**.

The setup was cabled as represented in **Figure 4.6c**, to allow for the microcomputer to be powered either by attaching it to the power grid via its adapter, or by a powerbank for remote operation far from the power grid, ensuring around 20 hours of continuous operation at minimal consumption. The cable disposition allows to charge the powerbank via the power grid without removing it, with or without powering the microcomputer simultaneously.

4.2.3. Nonsolvent Induced Phase Separation (NIPS). A good method to obtain white samples using polymer materials is nonsolvent induced phase separation (NIPS).[23] The method is schematically represented in **Figure 4.7**: a polymer is dissolved in a chosen solvent, usually to a consistent concentration (typically around 10-20 % w/w).[24] Afterwards, the solution is coated on a flat surface using a doctor blade or a similar instrument. Before the solvent can evaporate, the whole piece is immersed in a bath of a liquid, typically miscible with the solvent, but that is a nonsolvent for the polymer.[25] At that point, diffusion starts to occur progressively between the two liquids; when the local concentration of the nonsolvent in the ternary system polymer/solvent/nonsolvent goes over the cloud point, the polymer starts to precipitate. The precipitation leads inevitably to a porous, disordered structure. The precise morphology depends on many factors; the miscibility between solvent and nonsolvent, their viscosities, temperature, and the solubility parameters of solvent and nonsolvent both with respect to each other and with the polymer.[26] Pore dimensions can be tuned as well as the connections between them, leading to membranes with connected pores or separated ones or even pass-through channels with a finger-like morphology.[23, 25, 26] The aim is not for the membrane to perform as such but to show consistent scattering in the ultraviolet/visible/near infrared range, therefore closed pores of a reasonable size distribution, between 100 and 1000 nm is ideal.

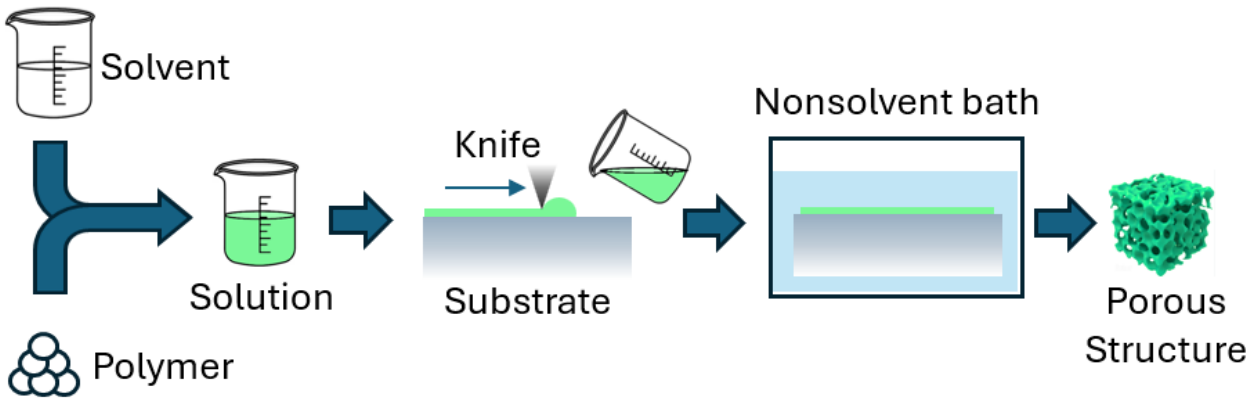

Figure 4.7. *Schematical representation of NIPS process. Colors are only for better visualization.*

4.2.4. White cellulose acetate samples fabrication & characterization. The first samples were fabricated out of cellulose acetate. The chosen solvent for cellulose acetate was acetone, which can dissolve the polymer in consistent concentrations greater than 20 % in weight.[21] Cellulose acetate dissolved in acetone forming a glue-like solution which was transferred on a woven-nonwoven PET textile hold firm onto a glass substrate and afterwards immersed in tap water. Over the course of two hours, this formed whitish samples around half a millimeter thick. The samples were then dried of excess water by placing them in an oven at 50 °C and glued to aluminum foil. The final result – which will be named Al:pCA – is a porous brilliant white thick film, as reported in the inset of **Figure 4.8a**. The film was optically characterized in the UV-Vis-NIR and in the medium infrared (MIR) range. Its characterization in the UV-Vis-NIR range is reported in **Figure 4.8b**; its characterization in the MIR range is reported in **Figure 4.8c**.

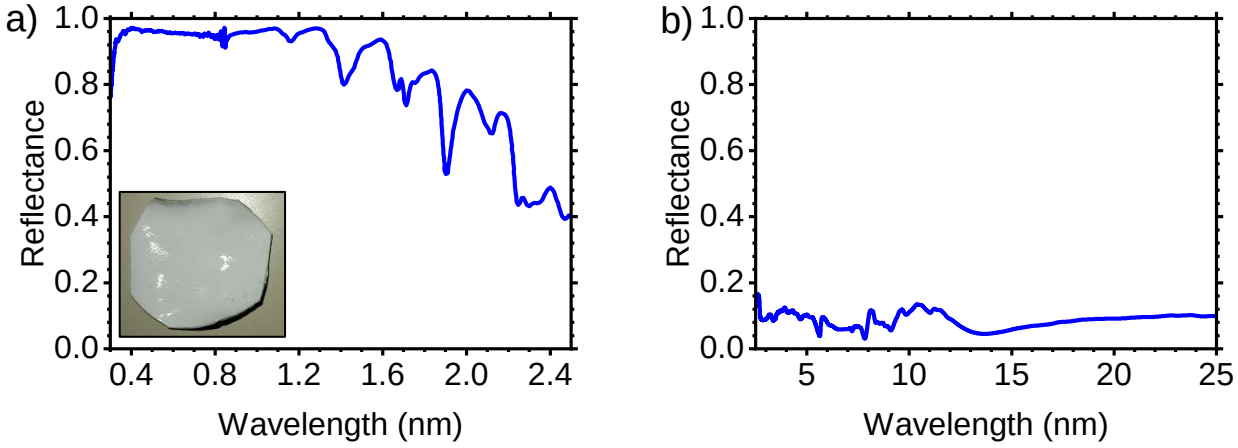

Figure 4.8. a) *Reflectance of the Al:pCA sample in the UV-Vis-NIR range. In the inset, a picture of the sample. b) Reflectance of the same sample in the MIR range.*

In each case, the sample's reflectance was measured. In the first case, an integrating sphere was used, and the reflectance is calculated with respect to a white reference. In the second case, the reflectance was calculated in drift mode, using an aluminum-coated integrating hemisphere (see **Appendix B.4.3-B.4.4** for additional details). There is a mismatch in the reflectance values measured in the common region around 2.5 µm. This may be due to both setups being close to their actual measurement limits, as well as for the low reliability of data acquired with the drift FTIR measurement. Future plans for this analysis are to acquire a gold-coated integrating sphere for the FTIR instrument. The absorptivity was extracted from the reflectance measurements solving **Equation 4.4** for $\tau_{RC} = 0$ since no light is passing through the aluminum foil. The inclusion of aluminum foil is needed in this case as it would be impossible to extrapolate a with nonzero unknown transmittance.

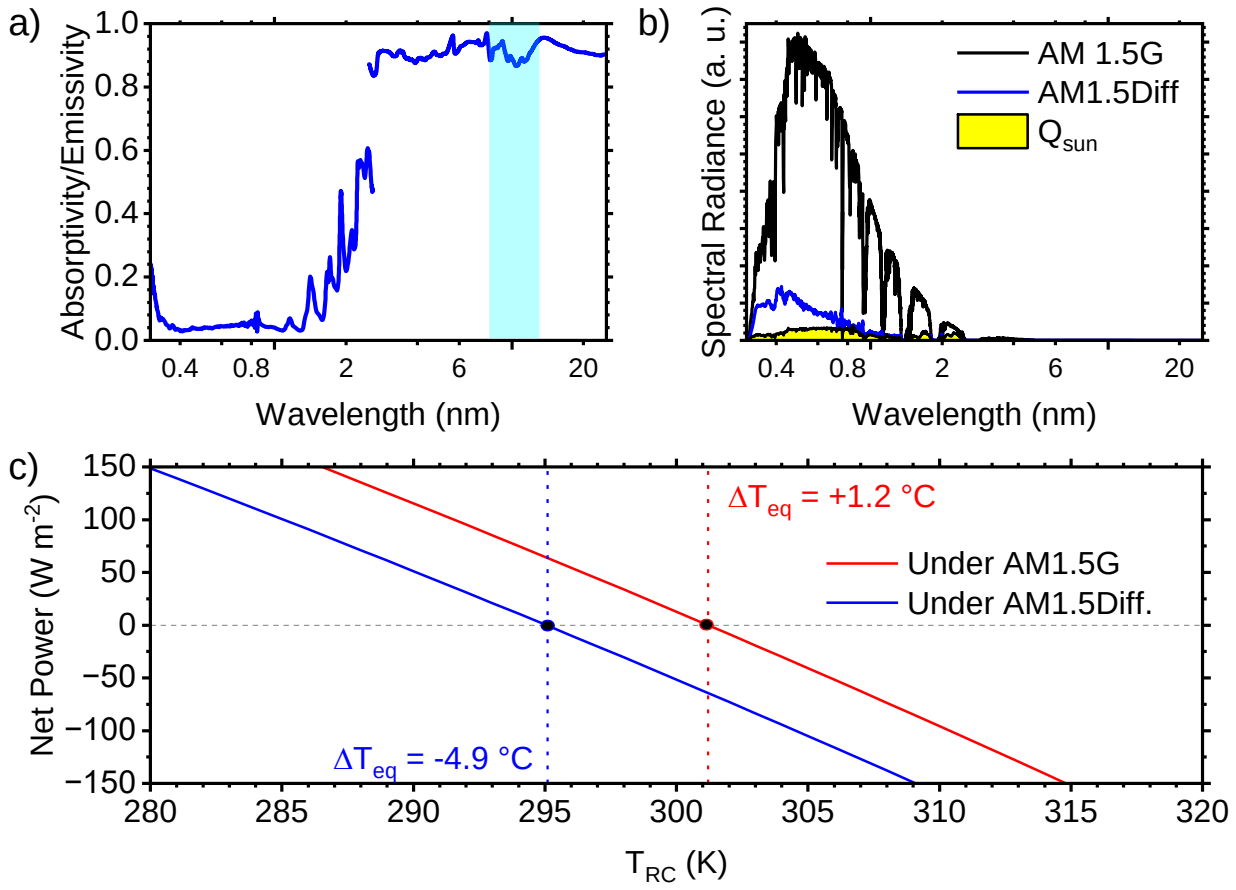

Figure 4.9. a) *Absorptivity/Emissivity of the sample Al:pCA.* **b)** *Sunlight spectrum AM 1.5G (black curve) and absorption of sunlight by the sample (yellow area).* **c)** *Net heat flow at various temperatures of the cooler under direct sunlight (red curve) and under diffuse sunlight (blue curve) as calculated via the model presented in the chapter. Equilibrium temperatures are marked with circles; ambient temperature is 300 K.*

The calculated absorptivity/emissivity of the sample is thus reported in **Figure 4.9a**. The atmospheric transparency region is highlighted with the light blue rectangle. The RC emissivity is around 0.85/0.90 in the atmospheric transparency window, with broadband characteristics. On the other hand, the absorption of sunlight as reported by the yellow area in **Figure 4.9b** is relatively low.[18] There is a consistent absorption in the NIR range due to the overtones and combination bands of CA vibrational modes, which is compensated by the reduced intensity of sunlight around those wavelengths. Still, the material is absorbing around 7 % of total sunlight intensity. Performing the calculations based on the model of **Subsection 4.1.2** allows to predict the temperature reached by the cooler in realistic conditions, as reported in **Figure 4.9c**. The red curve represents the net energy flow for various temperatures of the RC under direct sunlight (black curve of **Figure 4.9b**), whereas the blue curve is under diffuse sunlight (blue curve in **Figure 4.9b**). As diffuse sunlight is around 10 % than direct one, the equilibrium temperature corresponding to 0 net energy flow in this case is lower, predicted as -4.9 °C against the +1.2 °C under direct sunlight. The body is therefore not expected to

achieve sub-ambient cooling under direct sunlight, inevitable due to its relatively high absorption of sunlight.

The radiative cooling measurements of the sample, performed with the setup described in **Subsection 4.2.2**. The results of the measurement are reported in **Figure 4.10**. During the day, the temperature reached is around +3.1 °C with respect to ambient temperature, whereas during the night the temperature is -1.7 °C. Both performances are inferior to what expected by the model. The performance under direct sunlight is around 2 °C higher, whereas under diffuse sunlight is around 3 °C higher. The results obtained are the same order of magnitude of experimental values, but apparently some issues are affecting the measurement. In this case, I suppose there were two main issues. One was due to location; measurements were performed at ground level, in a garden at the bottom of a valley – meaning ambient humidity was consistently high, around 80-90 %. Since water vapor is an excellent absorber of thermal IR, this probably caused the effective transmittance of the atmosphere to be lower than expected. It may be the actual transmittance is closer to the tropical one of **Figure 4.1b** than the mid-latitude summer. Additionally, the sample was surrounded by buildings around five meters away in two out of four directions, which in first place impedes radiative exchange with the atmosphere in the full hemisphere. Moreover, since the buildings walls are painted white, the diffuse reflection impinging on the sample from the surrounding walls is probably affecting the measurement as well. Lastly, the measurements were performing in the central part of the day, where sunlight may be more intense than AM 1.5G. Further investigation regarding this will be conducted in the future.

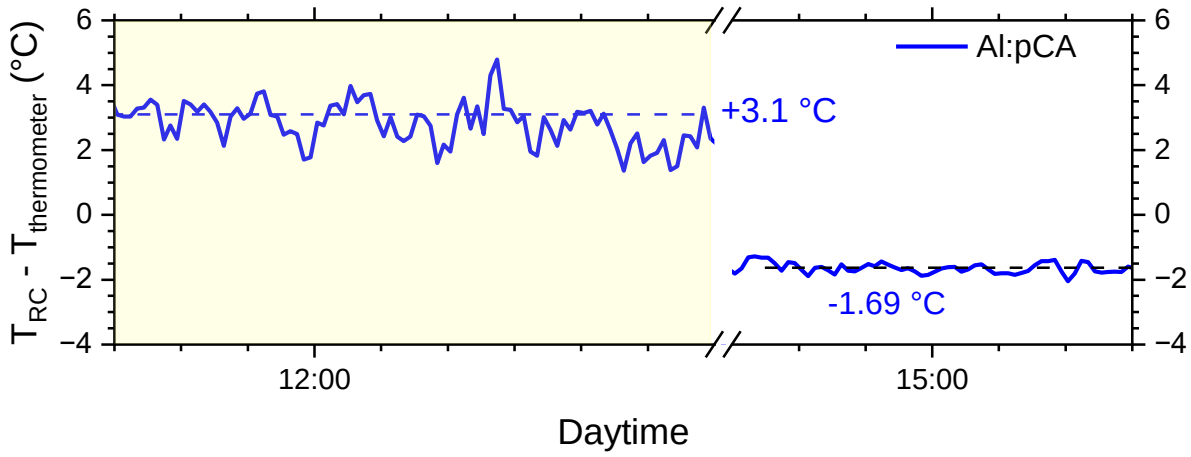

Figure 4.10. *Temperature reached by the Al:pCA sample under direct sunlight (yellow background) and under diffuse sunlight (second part).*

4.2.5. Integration of Aegises with Al:pCA. A further development of this work will also be joining the DBRs presented in **Chapters 1-3** with diffuse white reflectors such as Al:pCA. Indeed, **Figure 4.9a** and **Figure 4.9b** highlight the low but nonzero absorption of sunlight in the Vis and NIR region,

which causes the impossibility for the structure to achieve sub-ambient cooling under direct sunlight. In this regard, DBRs would come in handy; their reduced thickness does not introduce considerable absorptions in the Vis-NIR range, whereas their consistent reflectance could be used to further reduce impinging sunlight leading to a lower equilibrium temperature.

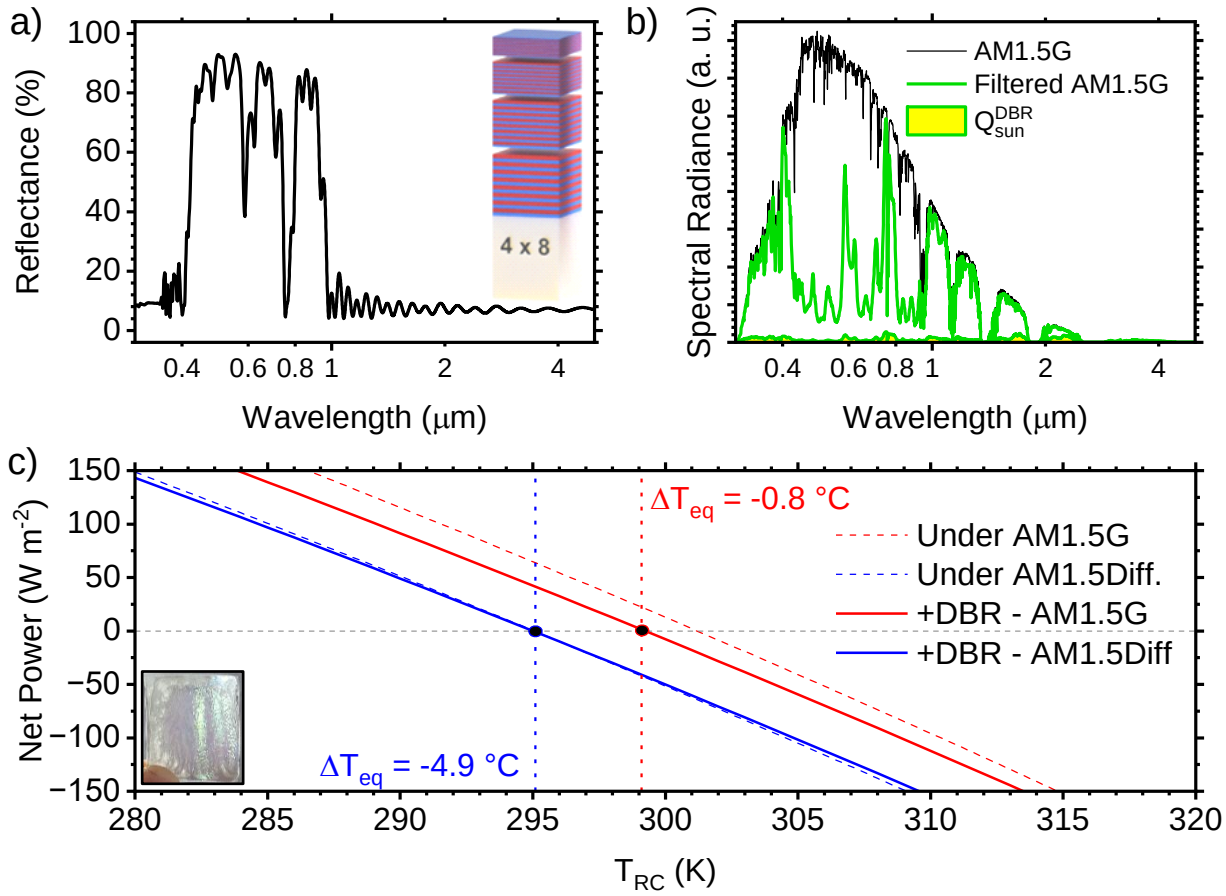

Figure 4.11. a) *Calculated reflectance of the 4x8 DBR designed V-AQPVK. In the inset, a schematic of the structure.* **b)** *Sunlight spectrum AM 1.5G (black curve) and the same spectrum filtered by V-AQPVK (green curve). Absorption of sunlight by the sample (yellow area under lower green curve) is reported.* **c)** *Net heat flow at various temperatures of the Al:pCA+V-AQPVK sample under direct sunlight (solid red curve) and under diffuse sunlight (solid blue curve) as calculated via the model presented in the chapter. Equilibrium temperatures are marked with circles. Dashed lines are the curves of* ***Figure 4.9c****. In the inset, an example of DBR cast on Al:pCA.*

To this goal, I designed a DBR with the principle reported in **Chapter 3**, consisting of a stack of 4 DBRs 8 bilayers each of poly(*N*-vinylcarbazole) (PVK) and Aquivion (AQ), for a total of 32 layer pairs. The schematic of the structure is reported in the inset of **Figure 4.11a**. The DBR is engineered to reflect Vis light (hence the code name AQ-PVK) in correspondence to the spectral range 400-900 nm, as apparent from its calculated reflectance spectrum reported in **Figure 4.11a**. The four structures correspond to four bandgaps/reflectance peaks, each achieving a reflectance around 90 % in the spectral region of interest; a background with interference fringes and an average reflectance 10 % is

observed outside the bandgap region. **Figure 4.11b** reports AM1.5G solar spectrum (black curve) and the same spectrum filtered by AQ-PVK (green curve). The presence of AQ-PVK drastically reduces the sunlight absorbed by the sample (yellow area under the lower green curve). This reduction leads to a lower equilibrium temperature, as seen in **Figure 4.11c**. With respect to Al:pCA (dashed red curve) the addition of the DBR to Al:pCA (solid red curve) yields an equilibrium temperature that is around 2.2 °C lower than Al:pCA alone, achieving a net cooling with respect to surrounding air equal to -0.8 °C. In the case I reported, the DBR is reflecting light in the whole Vis range, yielding a silver-like color. However, the aegises could be engineered to reflect only specific wavelengths of Vis light, to give a colorful hue to the white reflectors; the reduced reflection could be compensated for by reflecting NIR light instead. This could be extremely interesting for a commercial application to give aesthetic variety. Even though I did not fabricate the calculated sample yet, I report a preliminary result of integration in the inset of **Figure 4.11c**, where the iridescence due to the DBR over the white background can be appreciated.

4.2.6. Preliminary result on upcycling poly(vinyl chloride). In parallel to the application of DBRs on Al:pCA samples, I started working on a project of upcycling polymer waste. I will only scratch the surface of the topic, as it is extremely preliminary.

In this case, I used poly(vinyl chloride) (PVC) from recycled drug blisters. PVC is a widespread plastic, very used thanks to its resistance to weathering, antiflame properties and cheap cost. For example, it is used in tubes, electrical plants and drug blisters.[27-29] The latter pose a problem for recycling due to their multilayer composition including glues, other polymers such as poly(vinyl dene fluoride or PVDC) as well as an aluminum foil. A back reflector, a white scatterer / emitter is the ideal structure for an RC, leading us to the idea of upcycling blisters for RC applications. Following the procedure for NIPS described in **Subsection 4.2.3**, I dissolved the salvaged PVC in a 50:50 solution of tetrahydrofuran and *N,N*-dimethylformamide. This ensured solubilization up to 10 % concentration by weight with a reasonable viscosity of the final solution, allowing it to be easily cast directly on a glass substrate and spread using a 0.5 mm knife. Afterwards, the sample was placed in a refrigerated bath of tap water for around 8 hours. The process is difficult due to the fast dissolution of tetrahyrofuran into water, which leads to a fast and violent initial formation of the membrane. Nonetheless, a sample was effectively prepared, as reported in the inset of **Figure 4.12a**.

The appearance is white, slightly translucent, brilliant in the part exposed to sunlight. Some bubbles and macroscopical defects are encountered due to the violent formation process. The samples were then glued onto aluminum foil forming Al:pPVC samples. The sample's temperature was measured over time with the setup described in **Figure 4.5c** and **4.6a,** yielding the results reported in **Figure**

4.12a. Where the original drug blister heats up under sunlight by around +4 °C, the Al:pPVC sample does not, cooling down by around -2 °C instead. Note however that sunlight irradiance in November is 50-75 % that measured in July, hence the temperature reached are not representative of what could be achieved under summer Sun. However, the result reported here is very promising in the upcycling of PVC for radiative cooling applications.

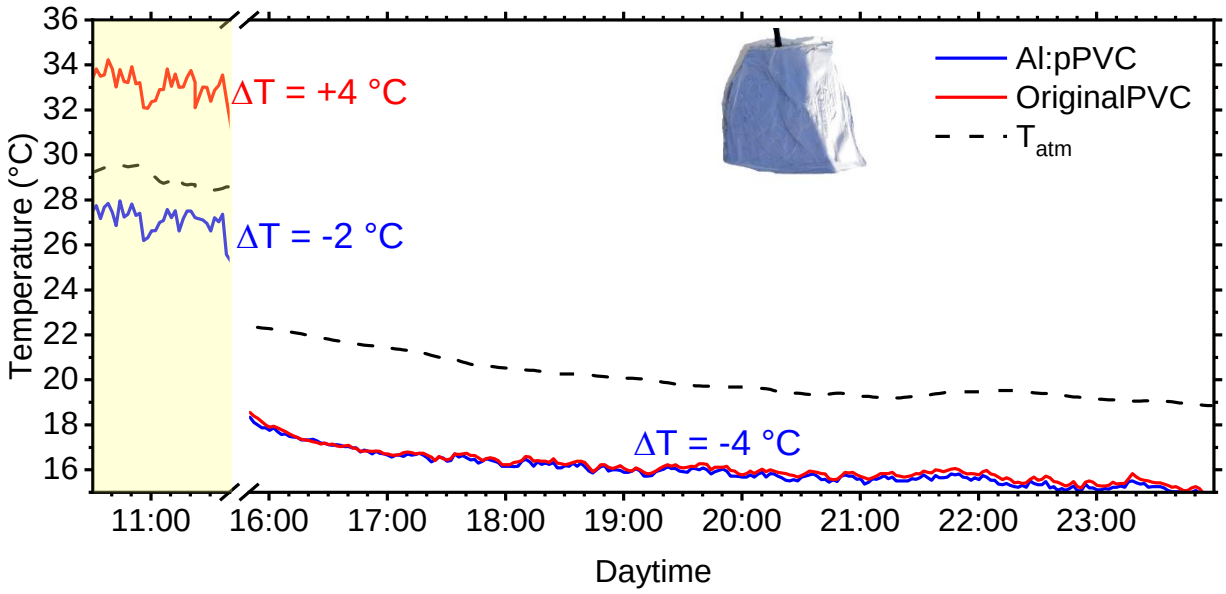

Figure 4.12. *Temperature reached by the Al:pPVC sample (blue line), the original PVC material (red line) and ambient temperature under direct sunlight (highlighted portion) and in the shadow (other portion). In the inset, a picture of the sample half-exposed to sunlight.*

4.3. Conclusion.

In this Chapter, I presented the introductory work I performed regarding the fascinating field of radiative cooling. I presented a thorough model based on the spectral-dependent, directional-dependent approach, to predict the efficacy of samples with known emissivity. Implemented in MatLab, this model allowed to calculate the equilibrium temperature reached by bodies with ideal emissivity profiles going from ultra-narrow to broadband. The results proved the superiority of broadband emitters in roofing-like applications and of narrowband ones in specialistic, record-breaking highly insulated ones.

On the experimental side, I presented the challenges of building a correct setup, following the iterations of improvement that lead to a portable, microcomputer-powered design. The latter allows to perform measurements anywhere for prolonged periods of time, granting an edge in in future measurements of the phenomenon.

Using nonsolvent induced phase separation, a solution processing technique, I fabricated highly reflective white porous scatterers out of CA and recycled PVC. The pCA samples, joined with an aluminum back reflector, were able to achieve -1.7 °C subambient cooling under diffuse sunlight, and only heating up by +3.1 °C even under direct sunlight. The model, applied to the measured optical response of the pCA samples, predicted reasonably well the temperature reached, although with some deviations. The latter are probably due to environmental factors like the underestimate of sunlight intensity, the overestimate of atmospheric transparency and the neglected sunlight diffused by the surroundings – all of which will be further investigated in the future. Alongside the latter, investigation will also focus on the integration of DBRs with pCA samples, as the model predicts subambient cooling should be attainable this way even under direct sunlight.

Recycled PVC samples attained subambient cooling even under direct sunlight, but measurements were performed under less intense November Sun and will need to be repeated and compared directly.

In general, the results obtained so far are quite promising, both for the upcycling of ubiquitous polymer waste such as PVC, but also for the integration of DBR/aegises to join radiative cooling and thermal shielding for high-performance thermal management applications.

Bibliography

1. E. Akpinar-Ferrand , A. Singh. *Environ. Sci. Policy*, **13**, 8, 702, (**2010**)

2. K. L. Kownacki, E. D. Hornyanszky, T. A. Chu, J. A. Olsson , P. Becker. *Int. J. Biometeorol.*, **62**, 3, 401, (**2017**)

3. M. E. Hossain, S. Rej, S. M. Saha, J. C. Onwe, N. Nwulu, F. V. Bekun , A. Taha. *Sustainability*, **14**, 13, 7537, (**2022**)

4. A. Lanfranchi, H. Megahd, P. Lova , D. Comoretto. *ACS Appl. Mater. Interfaces*, **14**, 12, 14550, (**2022**)

5. A. Lanfranchi, H. Megahd, P. Lova , D. Comoretto. *Chem. Eng. Sci.*, **283**, 5, 119377, (**2024**)

6. A. P. Raman, M. A. Anoma, L. Zhu, E. Rephaeli , S. Fan. *Nature*, **515**, 7528, 540, (**2014**)

7. L. Zhu, A. Raman, K. X. Wang, M. A. Anoma , S. Fan. *Optica*, **1**, 1, 32, (**2014**)

8. B. Zhao, M. Hu, X. Ao, N. Chen , G. Pei. *Appl. Energy*, **236**, 489, (**2019**)

9. J. Liu, Z. Zhou, J. Zhang, W. Feng , J. Zuo. *Mater. Today Phys.*, **11**, 100161, (**2019**)

10. M. Liao, D. Banerjee, T. Hallberg, C. Åkerlind, M. M. Alam, Q. Zhang, H. Kariis, D. Zhao , M. P. Jonsson. *Adv. Sci.*, **10**, 8, 2206510, (**2023**)

11. Z. Li, Q. Chen, Y. Song, B. Zhu , J. Zhu. *Adv. Mater. Technology*, **5**, 5, 1901007, (**2020**)

12. F. P. Incropera, *Fundamentals of Heat and Mass Transfer*. John Wiley & Sons, Inc., Hoboken, NJ (USA), **2007**

13. V. Sapritsky , A. Prokhorov, *Blackbody Radiometry - Volume 1: Fundamentals*. Springer, New York, NY (USA), **2020**

14. P. R. Griffiths, Introduction to Vibrational Spectroscopy, in Handbook of Vibrational Spectroscopy, **2001**

15. M. Kardar, *Statistical Phyisics of Particles.* Cambridge University Press, Cambridge (UK), **2007**

16. MODTRAN, http://modtran.spectral.com/ (accessed December, 2024)

17. J. Nelson, *The physics of solar cells.* **2013**

18. Solar Spectra AM1.5G and Direct+Circumsolar, https://www.nrel.gov/grid/solar-resource/spectra.html (accessed December, 2024)

19. X. Yu, J. Chan , C. Chen. *Nano Energy*, **88**, 106259, (**2021**)

20. A. Aili, Z. Y. Wei, Y. Z. Chen, D. L. Zhao, R. G. Yang , X. B. Yin. *Mater. Today Phys.*, **10**, 100127, (**2019**)

21. J. Jaramillo-Fernandez, H. Yang, L. Schertel, G. L. Whitworth, P. D. Garcia, S. Vignolini , C. M. Sotomayor-Torres. *Adv. Sci.*, **9**, 8, 2104758, (**2022**)

22. W. Zhu, B. Droguet, Q. Shen, Y. Zhang, T. G. Parton, X. Shan, R. M. Parker, M. F. L. De Volder, T. Deng, S. Vignolini , T. Li. *Adv. Sci.*, **9**, 26, 2202061, (**2022**)

23. D.-M. Wang, A. Venault , J.-Y. Lai, Chapter 2 - Fundamentals of nonsolvent-induced phase separation, in Hollow Fiber Membranes, Elsevier, **2021**

24. A. H. Arundati, C. R. Ratri, M. Chalid, H. Aqoma , A. F. Nugraha. *Ionics*, **30**, 1, 123, (**2024**)

25. G. R. Guillen, Y. Pan, M. Li , E. M. V. Hoek. *Industrial & Engineering Chemistry Research*, **50**, 7, (**2011**)

26. D.-M. Wang , J.-Y. Lai. *Current Opinion in Chemical Engineering*, **2**, 2, (**2013**)

27. P. Lieberzeit, D. Bekchanov , M. Mukhamediev. *Polymers for Advanced Technologies*, **33**, 6, 1809, (**2022**)

28. D. Pedrosa de Oliveira, J. S. R. Costa , L. Oliveira-Nascimento. *Sustainable Chemistry and Pharmacy*, **21**, 100423, (**2021**)

29. K. Lewandowski , K. Skórczewska, *Polymers*, 14, **2022**

Chapter 5 – Assembly of an External Cavity Laser Setup

Work performed at the Hybrid Photonics Laboratory (HyLab)
École Polytechnique Fédérale de Lausanne (EPFL), Switzerland

Abstract

This chapter is mostly standalone with respect to the main research topic, being the motivation for it more of personal growth than following up on photonic structures for thermal management. Nonetheless, there is a connection – **Chapter 2-3** evidenced how distributed Bragg reflectors can perform as full-fledged reflectors of near-infrared radiation, lossless and easy to fabricate and tune. Therefore, they can be used for heavily photonics-oriented applications requiring high-performance mirrors. In this chapter, I will report on the assembly of a 1550 nm external cavity laser setup which uses the same distributed Bragg reflectors reported in **Chapter 3** (the "aegises") as outcoupling mirrors. The external cavity setup is assembled using an antireflection coated laser diode as a light source; the feedback is provided properly aligning the distributed Bragg reflectors to reflect the diode's light back into it. The laser diode is characterized thoroughly, and then included into an external cavity setup with different mirrors, both distributed Bragg reflectors as well as metallic mirrors, are used as outcouplers. The external cavity laser assembled this way is characterized both in spectrum and in power; although no interesting effect is observed in the spectra, due to the extreme difficulty in aligning the setup properly, the influence of the external cavity on the light output-current intensity curve is apparent. The results show that using mirrors with different reflectance values allow to tune the slope of the light output-current intensity curve, the amount of spontaneous emission channeled in lasing modes, as well as the final light output. In this regard, the aegises performed better than gold-chromium mirrors with same reflectance value, due to the absence of absorption losses in the former. The results obtained here are interesting for future applications of polymer distributed Bragg reflectors in external cavity laser applications.

5.1. Introduction.

The thematic of this chapter is diverging from the common theme of thermal management, focusing instead on a more physics-reliant, photonics-heavy application for near-infrared (NIR) reflecting DBRs such as those discussed in **Chapter 3**. Indeed, I will present in this chapter how they can perform as outcoupling mirrors for an external cavity laser (ECL) system. There is far more theory on the topic than what is needed for the discussion of the chapter and far more than what is possible to squeeze inside a short introduction. Hence, I will only report the needed background.

5.1.1. Basic laser theory. **LASER** is a famous acronym which stands for **L**ight **A**mplification via **S**timulated **E**mission of **R**adiation. Stimulated emission is a photon-electron interaction alternative to absorption, where a photon is absorbed to promote an electron to an upper level (represented in **Figure 5.1a**) and spontaneous emission, where an electron decays on its own to a lower level emitting a photon (**Figure 5.1b**). In stimulated emission, as schematically represented in **Figure 5.1c,** an electron at a higher-than-fundamental electronic level absorbs a photon, causing it to be downgraded to a lower level while emitting two photons that are identical clones of the absorbed one. The absorption of a single photon produces two photons, thus achieving light amplification.[1-3]

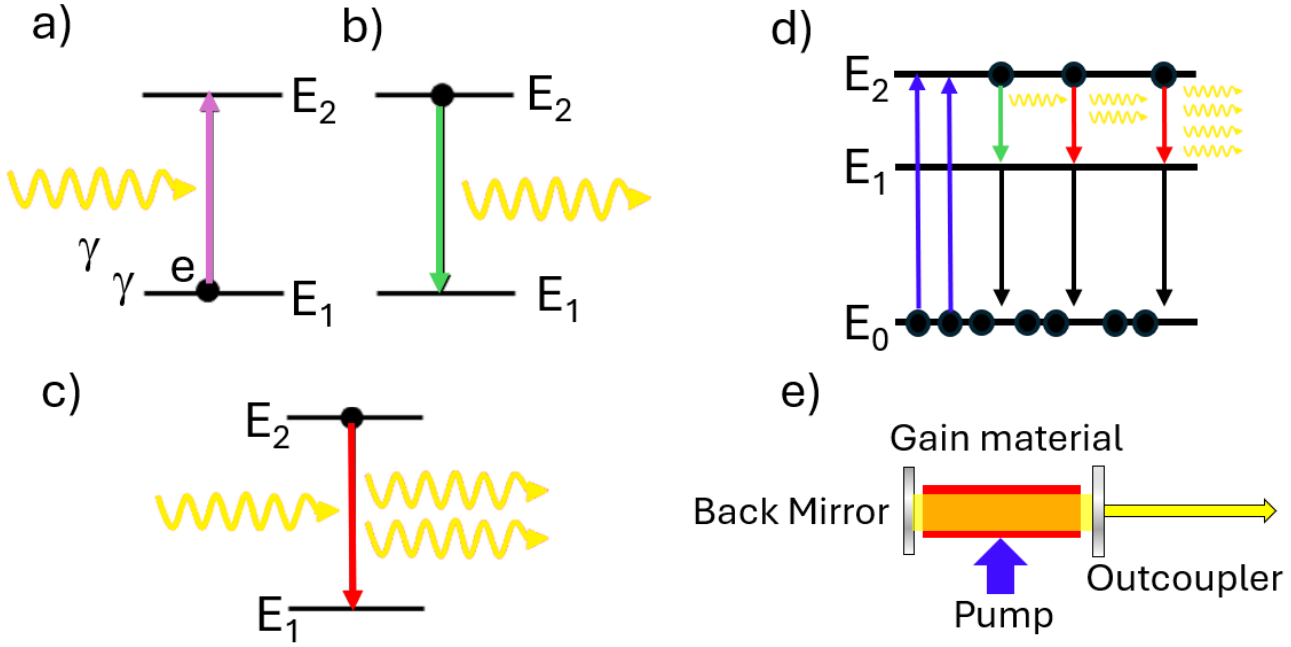

Figure 5.1. a, b, c) *Schematics of the processes respectively of absorption, spontaneous emission and stimulated emission;* **d)** *Schematics of the lasing process in a 3-levels system: blue is the pump, green and red are spontaneous and stimulated emission respectively, black is any fast nonradiative de-excitation pathway.* **e)** *Schematic of a laser apparatus*.

For a material to function as a laser, this stimulated emission must be the predominant result of the interaction between photons and electrons – which is possible if the two levels at which lasing is

observed are in a situation of *population inversion*, with the upper level having a higher population than the lower level. A simple schematization of the lasing process, for example in a three-level system, is presented in **Figure 5.1d**. A "pump", represented by the blue arrow in the figure, promotes continuously electrons from the first to the relatively long-lived third level ($E_0 \rightarrow E_2$) achieving population inversion between third and second level. Then, after a minor amount of spontaneous emission kickstarts the photon production (green arrow) stimulated emission occurs in mass from the third to the short-lived second level ($E_2 \rightarrow E_1$). A very rapid decay must then take place between the second and first levels ($E_1 \rightarrow E_0$).

In its simplest form, a laser is schematically represented in **Figure 5.1e**. A gain material, able to reach population inversion upon adequate stimulation through the pump (whether it is an electric current or a light source), inserted between two mirrors. The two mirrors ensure that stimulated emission is predominant in the outcoupled light. Indeed, they form a Fabry-Pérot optical cavity, forcing light to bounce back and forth providing "feedback" to the active material. The only wavelengths able to exit the cavity must satisfy the phase condition:

$$2\pi m = \frac{2nd}{\lambda_m} + 2\varphi d \qquad m = 0, 1, 2 \ldots \tag{5.1}$$

Which simply states that the total phase change upon a round-trip of light back and forth must be an integer number of 2π to achieve constructive interference. n and d are respectively the refractive index and thickness of the cavity, λ_m the wavelength, and φ is the phase change dependent on the photon flux inside the active material (negligible when lasing is not occurring). Since spontaneously emitted photons are incoherent with random phases, whereas stimulated emitted photons are coherent and in phase with each other, the phase condition strongly favors the latter which will be predominant in the output beam. Stimulated emitted photons which satisfy the lasing condition, indeed, will keep generating other identical photons, which will also satisfy the phase condition and stimulate others, and so on and so forth providing feedback to the system.

Of course, this amplification of stimulated emitted light will occur only if the gain condition is satisfied as well:

$$G - \alpha_L - \alpha_M > 0 \tag{5.2}$$

Which means that the photons gained through stimulated emission per unit length must surpass the losses due to scattering & absorption as well as those due to the mirrors. The G parameter is usually

a bell-shaped curve whose spectral position depends on the material; increasing the pump increases the values of *G*, allowing the lasing action to take place at selected modes according to both conditions.

5.1.1. External cavity lasers. ECLs allow to achieve an extremely reduced bandwidth and single-mode emission while allowing for a range of tunability of the lasing wavelength.[4, 5] The fundamental structure of an external cavity laser is quite simple, consisting essentially in a) a semiconductor laser diode (LD), b) and an outcoupling element.[5] LDs are essentially semiconductor junctions engineered properly to achieve population inversion, stimulated emission and therefore lasing action. The emission wavelength is dependent on the materials making up the junction and the emission occurs upon the passage of current, due to the formation and subsequent recombination of electron-hole pairs.[6, 7] Usually, the emissive material has a high refractive index (such as InGaAsP in the telecom region around 1550 nm, $n_{1550\text{nm}} = 3{,}24$)[8] which is enough to allow for a consistent amount of internal reflection of the produced light at the output facets. This creates the internal Fabry-Pérot cavity needed for the phase condition to be applied, the reflected light providing enough feedback to start the lasing action.[1] LDs are relatively cheap and easy to access on the market. However, their spectral output has a fixed bandwidth, depending on the gain curve, and their emission hops in frequency going randomly from one mode of the cavity to the other (mode hopping).[9] Their tunability is limited to eventual changes in the spectral shape of the gain function of the active material with temperature. However, changing temperature to an operating LD is ill-advised, as it reduces the diode's lifespan.[6]

Nonetheless, there is a strong need for tunable lasers in spectroscopy, especially for nonlinear applications as well as other fields such as terahertz generation. To solve the issue, the diode is coupled with another element to create the ECL.[7] This would correspond to moving further away from the gain material the outcoupler mirror in **Figure 5.1e**. In this configuration, the feedback to the LD is provided from an external element placed at a fixed distance. To allow this, one facet of the LD is usually antireflection (AR) coated to strongly reduce the influence of the internal cavity on lasing action and effectively extending the cavity up to the reflecting element.[10, 11] For the latter, some kind of wavelength selector is usually used to provide selective feedback at certain wavelength and govern the laser's emission spectrum.

Typically, this element is a diffraction grating, positioned at a few centimeters distance from the LD, engineered to provide back diffraction at the right angle for the right wavelength. Rotating and moving the grating gives feedback to a single laser mode tuning the laser output. The final goal of *HyLab* was using a novel metasurface[12] instead of a diffraction grating, to be able to tune the laser output electrically instead than mechanically (by rotating the grating). Another interesting approach

could be using all-polymer wavelength selectors, for example DBRs with a tunable optical response (see **Chapter 6**, **Subsection 6.5**) or rotating optical microcavities (**Chapter 6**, **Subsection 6.2-6.3**).

Of course the latter could be a future development, as my project started from actually designing, purchasing the parts, assembling and characterizing the elements making up the ECL. Only in the last part of the project I was able to assemble the whole ECL setup and test various outcoupling elements. Amongst the latter, I used the DBRs (aegises) of **Chapter 3.** They are perfect candidates to prove the suitability of all-polymer DBRs to the task as they provide different values of reflection at the telecom wavelength (1550 nm) and are fabricated out of various polymer materials. This way, I report on the first use, to my knowledge, of polymer mirrors in a telecom-wavelength ECL, proving all-polymer structures can effectively perform of outcoupling elements.

5.2. Results & Discussion.

5.2.1. Preliminary Measurements –LD Characterization. The schematic of the setup used for LD characterization is represented in **Figure 4.1a.** The LD was mounted on a specific mount which integrates a heat sink with thermoelectric cooling and thermistor as well as the wiring to control the current flowing through the LD. To provide current and temperature control to the LD, a current controller was used in conjunction with a temperature controller (see **Appendix B.5.1** for the experimental details).

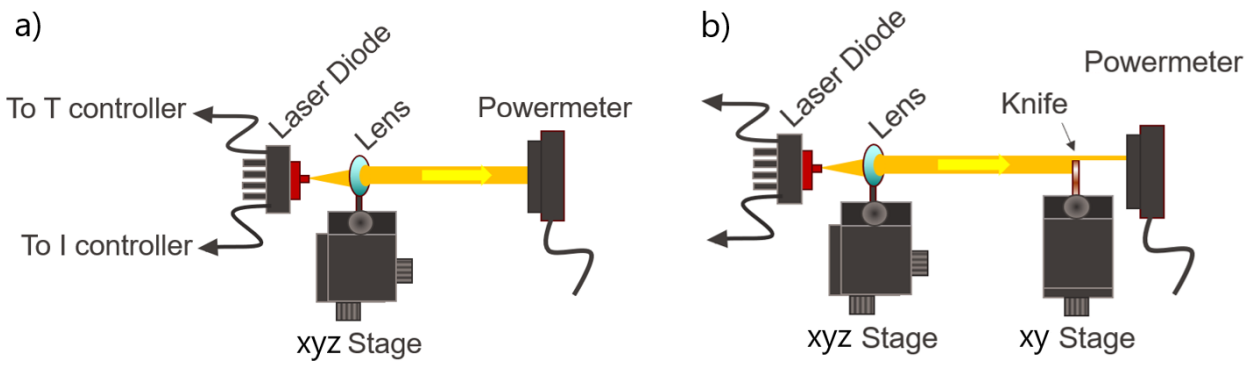

Figure 5.2. a) *Schematics of the setup used for the preliminary measurements and the characterization of the laser diode.* **b)** *Schematics of the setup used for knife's edge measurements.*

Light from the laser diode was collimated through an aspheric AR-coated lens (2.75 mm focal length for characterization and preliminary measurements, 1.45 mm focal length for the final configuration). To center the lens exactly in front of the emissive facet of the LD and tune the distance between them, the lens was attached to an ensemble of moving stages allowing for precise 3d-movimentation. A powermeter was placed along the beam path, 10 cm away from the LD. The

powermeter was replaced with a free space-to-fiber coupler, and the signal analyzed via an optical spectrum analyzer (an accurate, high-resolution spectrophotometer).

To build an external cavity laser the feedback must come predominantly from the outcoupling element and not from the diode's facet. Therefore, an LD covered on one side with an antireflection (AR) coating and on the other with a high reflection coating was used. The latter should provide the back facet with around 90 % reflectance, whereas the manufacturer's website promises values lower than 0.01 % for the AR-coated one.[10, 13, 14] The diode is made of indium phosphide (InP), with the active region most probably made of indium gallium arsenide phosphide (InGaAsP). This material provides an emission wavelength around 1550 nm, hence precisely in the center of the high-reflectance regions of the DBRs presented in **Chapter 3** (**Figure 3.4b-d**).

This AR-coated LD was mounted on the setup of **Figure 5.1a** and characterized. **Figure 5.3a** reports the comparison between the L-I curves of the AR-coated LD (red circles) with an uncoated one (black squares). Note that the comparison is only qualitative since the diodes are neither the same model nor manufacturer. The behavior of the uncoated diode is the typical one of an LD; a flat part which transition abruptly to a linear behavior.[4-6] The physical explanation is quite simple: in the flat part increasing the injected current only creates more charge carriers (electron-hole pairs). Referring (inaccurately) to **Figure 5.1d**, the pump is populating the third level; the emission, however, is still extremely low, due only to the small amount of spontaneous emission caused by the recombination of carriers statistically occurring. The losses are overall too great to satisfy the gain condition (**Equation 5.2**). Once the population of electrons and holes per unit volume reaches a critical value (corresponding to a "threshold current"), stimulated emission become dominant. Carriers recombine emitting spontaneous photons, which stimulate the emission of photons from other electron-hole pairs, which in turn stimulates more emission, and so on. Light is reflected back and forth from the LD's facets, forcing the emission to be channeled in the modes corresponding to the Fabry-Pérot cavity formed this way. Once the threshold value of current is reached any more injected carriers immediately recombine, hence the linear increase of light output upon increasing the current.[6, 7]

Whereas the uncoated diode shows a sharp transition to the linear regime upon reaching the lasing threshold, the transition for the coated LD is more gradual, with a greater contribution of spontaneous emission which smooths out the curve. A fitting of the linear part of the L-I curve (red line) allows to calculate the threshold current, which results I_{th} = 25.6 mA.

The polarization of the LD was measured rotating gradually a polarizer placed in front of the Powermeter and reading the corresponding power output. The results are reported in **Figure 5.3b**. The power is steadily reduced rotating the polarizer; the ratio between the power when the polarizer plane is perpendicular to the optical table is 1/1000th of the parallel one. Therefore, the light output is

essentially polarized parallel to the optical table. Light tends to exit LDs parallel to the junction plane, due to the very reduced thickness of the emissive material with respect to its width;[5, 7] since the junction plane is apparently parallel to the optical table, this result is consistent.

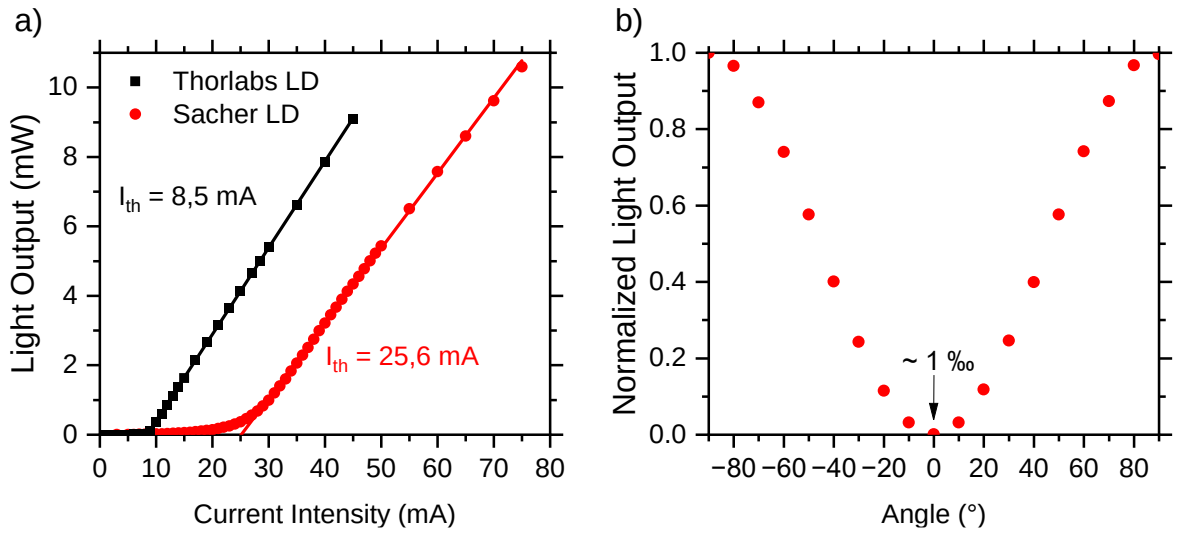

Figure 5.3. **a)** *L-I curves relative to the uncoated LD (orange curve) and to the AR-coated one (blue curve).* **b)** *Power of the beam relative to different rotation angle of the polarizer. The angle is relative to the normal to the optical table.*

The spectrum of the AR-coated LD was measured via the optical spectrum analyzer with respect to different current intensities as reported in **Figure 5.4a**. Notwithstanding the AR-coating, the emission is confined in lasing modes, centered on 1540 nm, starting from around 18 mA. Increasing the current intensity causes more lasing modes to activate, mostly towards shorter wavelengths; the overall emission of the LD is clearly multimode in nature.

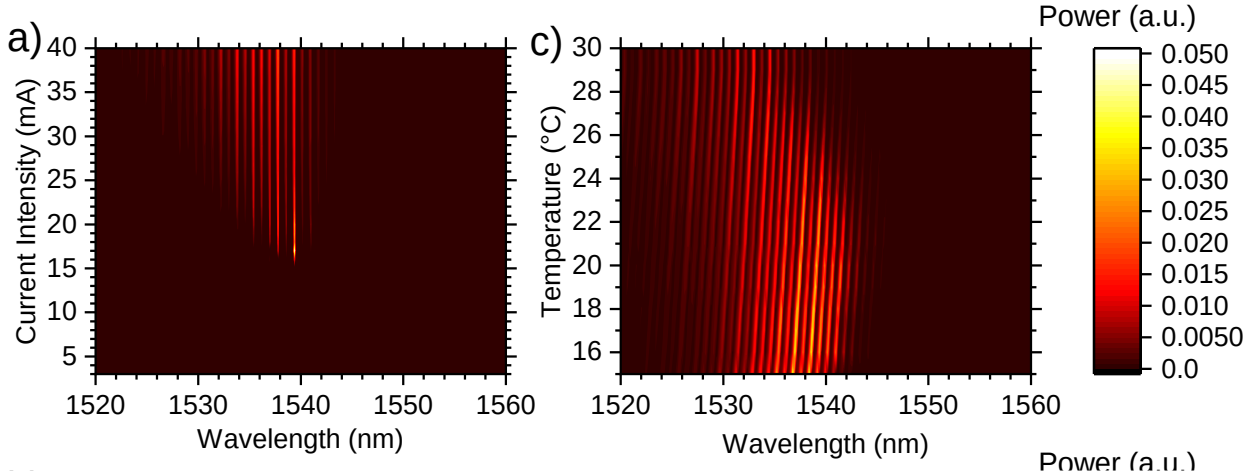

Figure 5.4. a) *Contour plot representing the measured emission spectrum of the LD, when injected current is varied.* **b)** *Contour plot representing the measured emission spectrum of the LD when operating temperature is varied. Color codes the radiation intensity measured by the OSA.*

Figure 5.4b represent the spectra of the LD when its temperature is varied between 15 and 29 °C. Two different phenomena can be simultaneously followed. Indeed, every single mode tends to shift towards longer wavelengths, following the change in refractive index due to the temperature. At the same time, the active lasing modes (which mimic the gain curve of the active material)[1] have an initial tendency to follow the same trend, but their wavelengths start decreasing after 21 °C. Since the exact spectrum is not particularly of interest, the operating temperature was be kept at 22°C, the same at which the company testing was performed.

The length of the LD cavity was not shared from the company, therefore it was obtained from the spectrum itself. Indeed, as the laser cavity is a Fabry-Pérot resonator, it is known that the wavelength distance between fringes (free-space range, FSR) depend on the length *d* and refractive index *n* of the cavity as per **Equation 5.3**:[15]

$$nd = \frac{cN_f}{2(\upsilon_2 - \upsilon_1)} \tag{5.3}$$

Where *c* is the speed of light and N_f is the number of interference fringes fully contained between frequencies υ_2 and υ_1. When N_f equals 1, $\upsilon_2 - \upsilon_1$ is the FSR.[1, 16] Via a MatLab code, the free spectral range for spectra from 3 to 75 mA was extracted via a peak search and plotted in **Figure 5.5a** against frequency. The black squares are the mean extracted FSR for each spectrum, whereas the grey band is the error obtained as standard deviation on the same data. The FSR is around 100 GHz; applying **Equation 5.3** to the FSR curve in **Figure 5.5a** yields a series of values for the product *nd*, called optical thickness, reported in **Figure 5.5b**. As the FSR varies with the current intensity, so do the optical density – this is due to the change in refractive index of the active medium as the carrier density changes and the photon flux is increased. To extrapolate the most likely optical thickness when no carriers are injected (that is, 0 mA), the first part of the plot undergoes a linear fitting. The resulting optical thickness at 0 mA is 1.53 µm. Using the refractive index of InGaAsP (the material of which the diode is fabricated out of), that is n_{1550nm} = 3.24,[8] the physical length of the cavity is obtained as *d* = 472 nm, which is compatible with the size of most commonly used diode laser cavities.

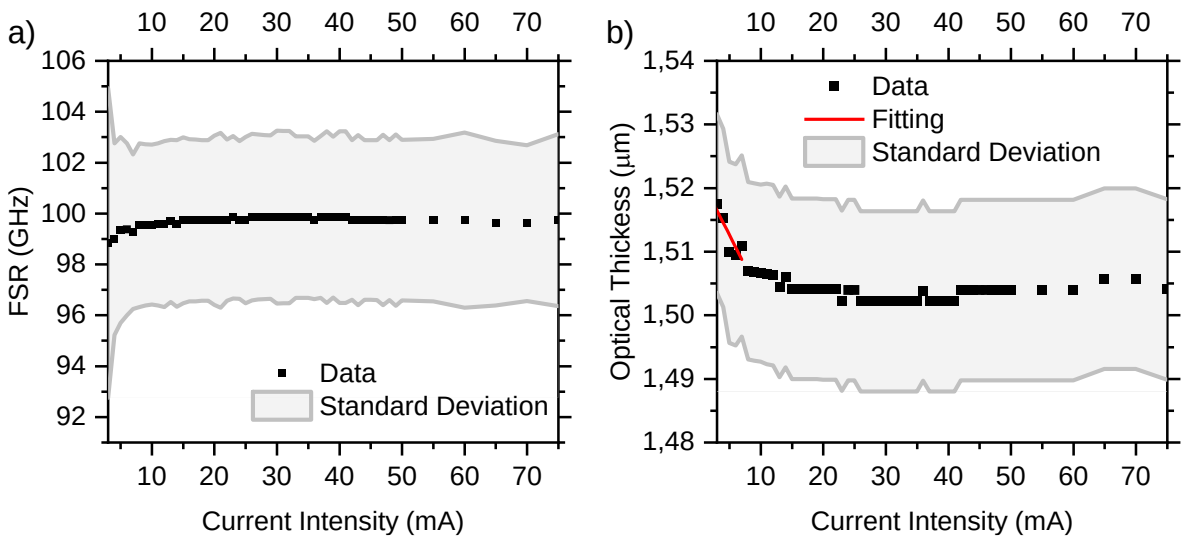

Figure 5.5. **a)** *Extrapolated FSR from different current intensities passing through the diode.* **b)** *Optical thickness of the laser cavity as calculated from the FSR. Red line is a linear fitting of the first three data points.*

The setup represented in **Figure 5.2b** was used to perform knife's edge measurements on the collimated beam. The core of the setup is identical to **Figure 5.2a**, including the LD on its mount and the lens on its moving stage. Directly in front of the powermeter, a thin copper slab is used as knife. The latter is attached to an xy moving stage and can be finely moved to cut the beam progressively along the left-right direction or the up-down one respectively. Measuring the power with respect to the knife position yields the integral of the beam shape in the directions parallel and perpendicular to the optical table. The beam size and divergence were extrapolated via knife's edge measurements as described in the experimental section, using the setup reported in **Figure 5.2b**. The derivative of power with respect to knife's edge position yields the results reported in **Figure 5.6a-b**, cutting in the direction parallel to the optical table (red circles) or in the direction perpendicular to the optical table (black squares). The measurement yields a different value when performed 2 cm far from the LD (**Figure 5.6a**) or 96 cm far (**Figure 5.6b**), suggesting some amount of divergence of the beam.

As the profile of the beam is gaussian, fittings of the data yield gaussian curves whose full width at half maximum (FWHM) can be taken as the nominal size of the gaussian beam. The fitting estimate for the laser beam 2 cm from the LD a size of 1.66 × 1.76 mm^2, which after 94 cm becomes 1.78 × 1.55 mm^2. This means that the divergence angles can be calculated from basic trigonometry, yielding (-0,013°) and (0,007°) in the directions perpendicular and parallel to the optical plane respectively. Since the beam is diverging in one plane and converging in the perpendicular one, the LD must be slightly astigmatic. This means the ideal point source for the light emitted by the LD parallel to the optical table is at a different distance from the lens than the point source for light emitted

perpendicularly to it. This means that perfect collimation of light from the LD is impossible. However, since the divergence is extremely low, this configuration was used anyway for the following experiments.

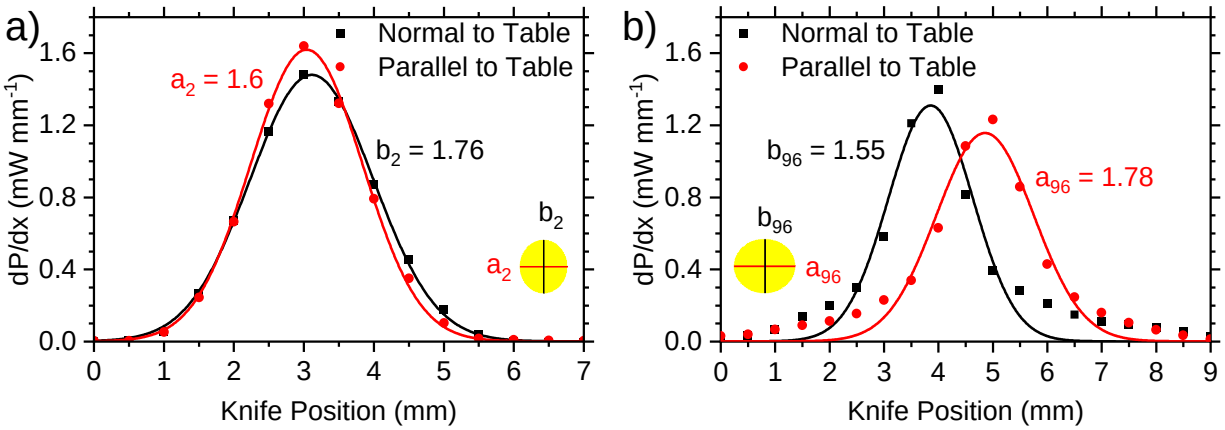

Figure 5.6. **a,b)** *Derivatives of power, fitted with gaussian curves (solid lines). Reported against knife position at 2 cm distance from the LD (a) and 94 cm further (b). Normal and perpendicular refer to the direction of movement of the knife. In the inset, a section of the beam in scale.*

5.2.3. ECL Configuration - setup. The final iteration of the setup is represented schematically in **Figure 5.7**. To the core of the setup, a custom-designed mount was added to allow for placement of the outcoupler mirror on the beam path (the latter represented by the yellow arrows, orange beam). The mount, attached to a 3d-moving stage and able to 2-axis tilt, allows the outcoupler to reflect light back in the LD (green arrow). The output portion of the beam is reflected by two adequately tilted gold mirror to ensure it is parallel to the optical table. A 50/50 plate beamsplitter is then placed in the beam path. This way, the laser beam's power can be measured via the powermeter simultaneously to the measurement of the spectrum via the optical spectrum analyzer. Although the lens used for coupling to the optical spectrum analyzer is AR-coated, the fiber facet is not. Thus, when the system is properly aligned the light reflected from it manages to be reflected all the way back to the LD and provide unwanted feedback (red arrow). Thus, an optical isolator was placed immediately after the outcoupling mirror, allowing output light and blocking unwanted additional feedback (see **Appendix B.5.1**).

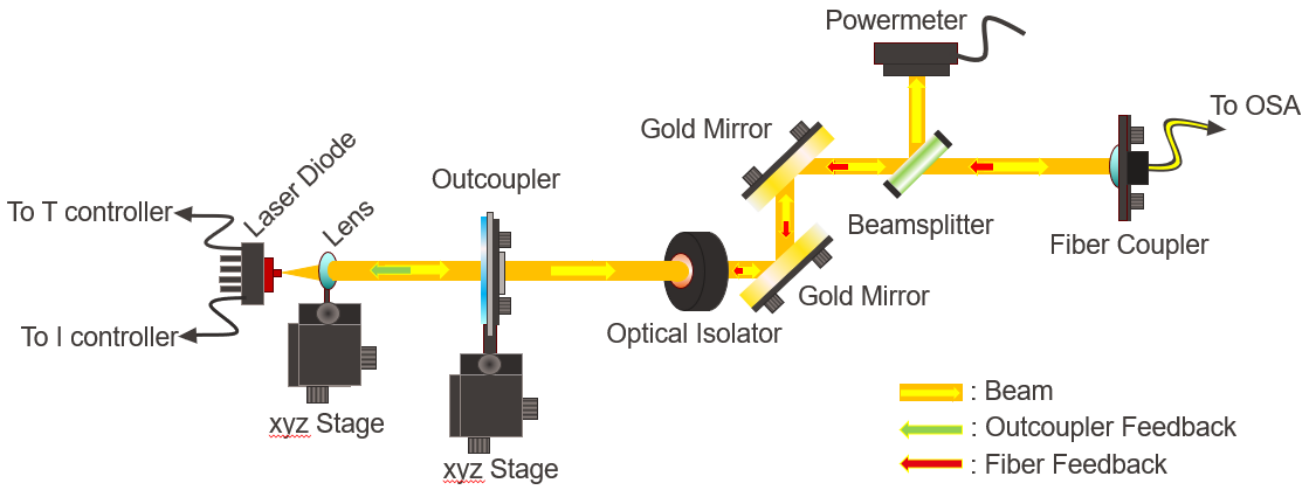

Figure 5.7. *Schematics of the setup used for the final measurements. Yellow arrow indicates the net direction of the beam propagation, green arrow represents the feedback given by the outcoupler to the LD (necessary), red arrow is the feedback due to the optical fiber connecting to the OSA (unwanted).*

The following step was to find a way to reflect the emitted light back to the AR-coated LD, which would qualify the setup as an ECL. This is needed to provide feedback to the laser from an external element, to initiate the lasing action. In our case, the choice was to use mirrors with different reflectance intensities. Different mirrors were fabricated and measured as per the experimental section. Their reflectance spectra with respect to a thick gold mirror are reported as a function of wavelength in **Figure 5.8**. The metal mirrors are made out by a thin layer of 2 nm of chromium on a half-millimeter thick fused silica substrate, on which 10 and 5 nm of gold were deposited respectively for samples Au10Cr2 and Au5Cr2. The metallic mirrors used as outcouplers in the experiments here described were designed via a custom python code based on the transfer matrix method (TMM). This allows to calculate the optical response in terms of both reflectance and transmittance of an ensemble of films, known the refractive index dispersion. The code was validated through comparison with already validated MatLab codes developed by the Rely Photonics group at the University of Genoa across the years.[15] After their fabrication via evaporation in EPFL's clean room, the mirrors were characterized at EPFL with a tunable laser (Menlo) measuring their transmittance as reported in **Appendix B.5.2**.

The spectra of the substrate alone and of the two mirrors are reported in **Figure 5.8a**, **5.10b** and **5.10c** respectively. Of course, the substrate shows an extremely low reflectance due to the low refractive index of SiO_2, around 5 %. The reflectance is characterized by an oscillating pattern of interference fringes due to the Fabry-Perot effect of the two interfaces.[1]

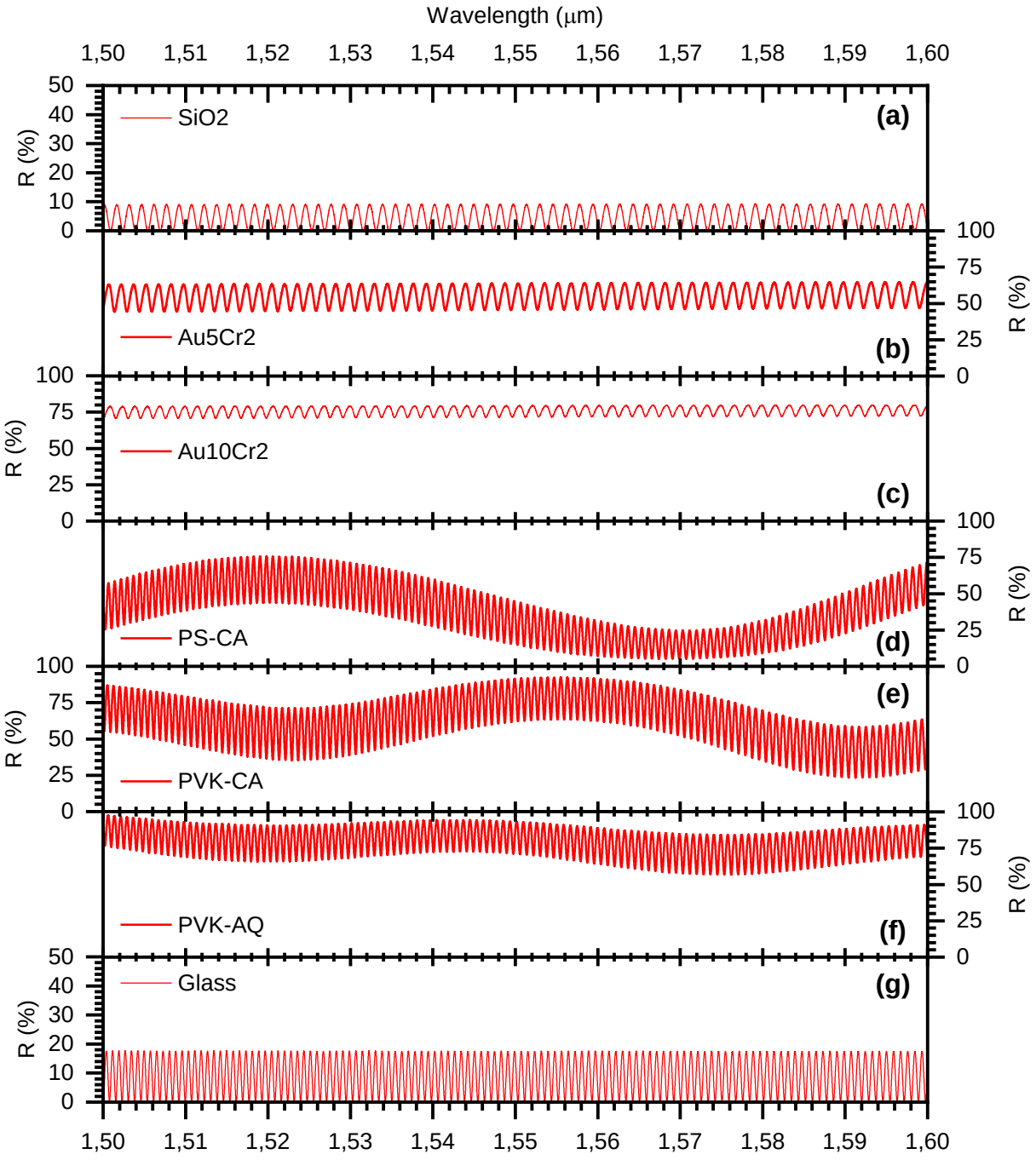

Figure 5.8. *Reflectance spectra, measured with the tunable laser, relative to* **a)** *SiO_2 substrate*, **b)** *metal mirror Au5Cr2,* **c)** *metal mirror Au10Cr2,* **d)**, **e)**, **f)** *dielectric mirrors PVK-AQ, PVK-CA and PS-CA respectively, and* **f)** *bare glass.*

The same pattern is well visible in the spectra of the metal mirrors grown on it (**Figure 5.8b** and **5.10c**), which is consistent as the periodicity of the interference fringes depends on thickness and the metal layers are negligibly thin. However, the reflectance of the mirrors is much higher, 55 % for Au5Cr2 and 75% for Au10Cr2. The values are essentially constant with a trend of slight increase with the wavelength, a standard behavior for metals. The spectra of the dielectric mirrors are reported in

Figure 5.8d, e, f (for the white light measurements, see **Figure 3.4b-d**) on the other hand, are less homogeneous, presenting the typical peaks and minima due to the presence of complex band gaps generated by the structures.[17] As expected, PVK-AQ provides the maximum reflectance, generally around 80-90%. The other structures are less homogeneous, with PVK-CA varying in reflectance from 60 to 75 % depending on the spectral region and PS-CA varying from 20 to 60 %. Note that in every structure the interference fringes pattern is well apparent due to the presence of the glass substrate. Its periodicity is roughly double that of the metallic mirrors, as the substrate is twice as thick. The reflectance spectrum of the glass substrate alone shows the same interference fringes, as shown in **Figure 5.8g**. Overall, the pattern is more intense and the reflectance of the glass is greater (around 10 %) than fused silica, which means the refractive index of the glass is greater than that of the fused silica, as expected.[18, 19] Note that in **Figure 3.4b-d** no interference fringes due to substrate were visible due to the reduced coherence length of the white light used for the measurement (see also **Appendix A.2.1**).

After placing the holder and mirror in position, the system was finely tuned; to provide the necessary feedback from the outcoupler to the LD and achieve the ECL configuration, a first rough alignment is performed using an upconversion revealing card making sure to superimpose the beam with its reflection. Then, the fine tuning is performed by scanning the possible positions of the outcoupler's tilting axis until the output increases drastically. Upon reaching the maximum output, the ECL condition is achieved.

When feedback is given by mirror Au5Cr2 (reflectance in **Figure 5.8b)** the spectrum obtained is reported as a function of wavelength in **Figure 5.9a**. A perturbation appears as a full-fledged interference fringes pattern, superimposed to the modes of the internal cavity. These additional fringes appear only in the ECL configuration, when mirror is aligned, and feedback is given (red line). Only the internal cavity modes, instead, are seen when feedback is not given (black line). The additional modes should correspond to the external cavity. To double check the correspondence between FSR of these new fringes and length of the external cavity, the distance was gradually increased from 19 to 32 mm, while the corresponding spectra were measured and reported as a function of frequency in **Figure 5.9b**. The FSR for each spectrum was then extracted via a MatLab algorithm and plotted in **Figure 5.9c** with its standard deviation (grey shade). The FSR is decreasing with the distance, qualitatively following an inverse proportionality trend. Indeed, when **Equation 5.3** is applied to the FSR to extrapolate the optical length of the cavity generating the fringes **Figure 5.9e** is obtained. In the latter plot, the increase in length measured directly with the moving stage micrometer is reported on the x axis, whereas the increase in length obtained from the FSR is reported on the y axis. A linear fitting to the curve confirms a 1:1 proportionality between the two quantities, with intercept

compatible with 0 and slope compatible with 1. These results confirm that the modes are effectively correspondent to the external cavity. The intensity of these modes seems to decrease as their number and density increases. This may be explained as the energy associated to the fringes remains the same, but as their number increases it is divided amongst them.

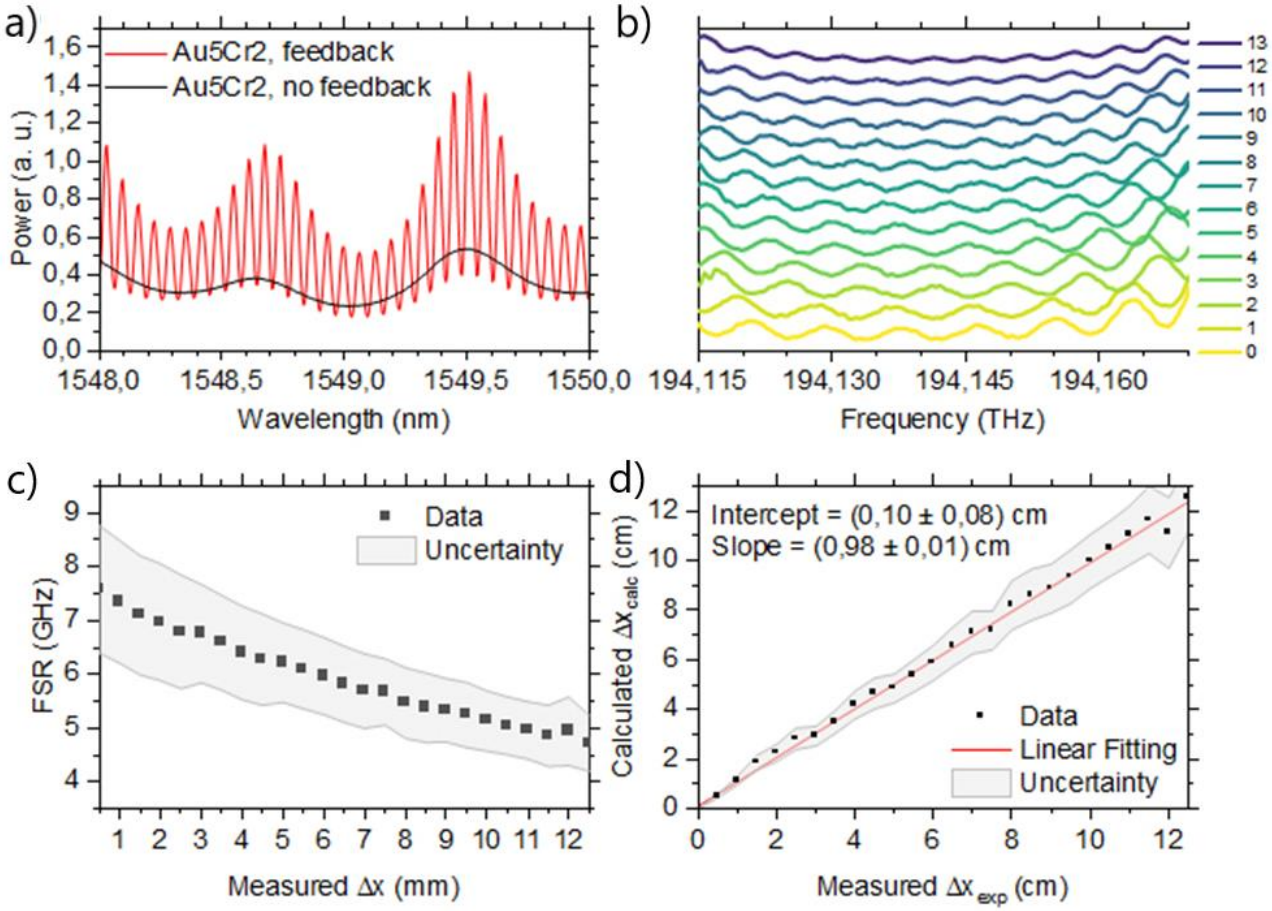

Figure 5.9. a) *Spectra of ECL-Au5Cr2 (red curve) and when the misaligned Au5Cr2 does not provide feedback (black curve).* **b)** *Spectra of ECL-Au10Cr2 when mirror is placed at increasing distance (19 mm plus the value reported in the legend, in mm).* **c)** *FSR obtained by the curves in (d).* **d)** *Increase in length of the external cavity as measured (x axis) against as derived from the variation in FSR (y axis).*

5.2.4. ECL Configuration – 1.45 mm focal length lens. The metasurface which was *HyLab*'s final goal for this project is a patterned surface of a reduced size (2 mm by 2 mm in the final iteration). Therefore, the aspheric lens was replaced, reducing its focal length from 2.75 mm to 1.45 mm to have a smaller beam. This makes the design in ECL configuration more sensitive to the exact mirror's position and the alignment more difficult, hence why it was tested only in second instance. A knife's edge measurement on the setup yielded the result reported in **Figure 5.10**. The derivative of power against knife position plot is directly reported, at a 10 cm distance between LD and powermeter (**Figure 5.10a**) and at a 105 cm distance (**Figure 5.10b**). The results are beams with a gaussian shape, as expected. From **Figure 5.10a** it can be seen how the beam is much smaller than before (see **Figure**

5.6 for the setup using 2.75 mm focal length lens). Indeed, at a 10 cm distance from the LD the beam size is (0.62 × 0.88) mm^2 (yellow ellipse in **Figure 5.10a**) whereas 95 cm later is (1.21 × 0.62) mm^2 (yellow ellipse in **Figure 5.10b**). Considering the nominal width of the beam is $\sqrt{3}$ times the values reported, at short distances it fits nicely in the 2 mm x 2 mm area of the metasurface. The beam is converging with a -0.02° angle in the direction normal to the table, whereas in the parallel one it is diverging with a 0.04° angle. This is evidently due to the diode's astigmatism; the effect is more pronounced that before, due to the reduced focal length of the lens. The latter indeed magnifies the slight differences in the positions for the point sources of the LD in the two perpendicular directions.

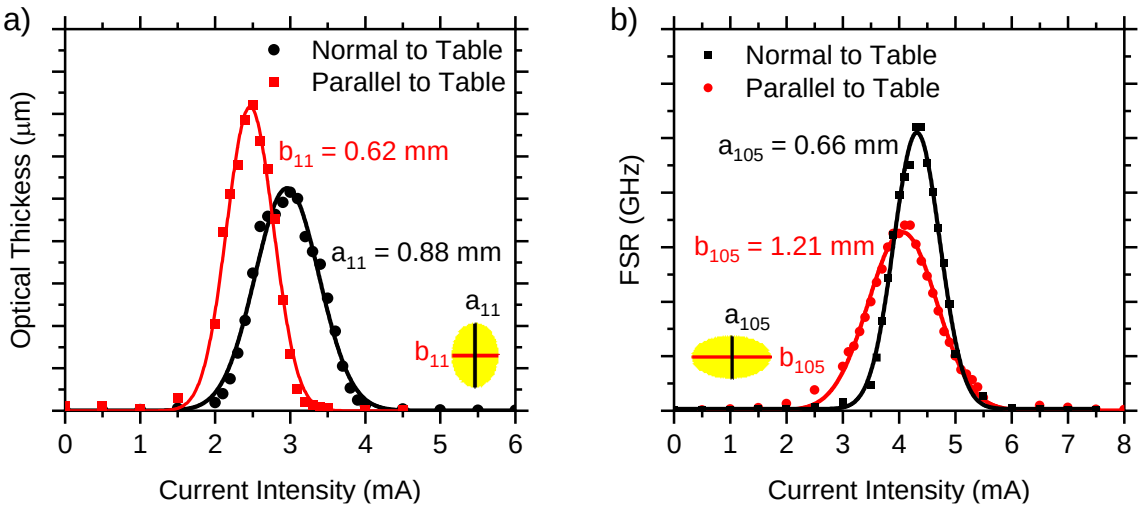

Figure 5.10. a) *Derivative of power against knife position in the horizontal (red lines) and vertical (black lines) planes of the laser beam when the 1.45 mm focal length aspheric lens is used to collimate it.* **b)** *Correspondent curves measured after 95 cm. A beam section in scale is represented in yellow.*

The final measurements were performed with the setup in **Figure 5.7**, providing feedback to the laser diode with each mirror at disposal. Most of the measurements are reported, with an estimated sensitivity error, in **Figure 5.11a**. Indeed, increasing the reflectance of the mirror, the light output gradually decreases and the threshold current decreases as well. The two metallic mirrors are outliers in this case, as their threshold currents are slightly lower than their DBR counterparts, but their light output is far lower with respect to their dielectric counterparts with similar reflectance. This may be explained as metallic mirrors absorb around 10 % of the light for each round trip, whereas dielectric mirrors do not. In theory, the threshold current for a lone diode is function of a lot of different parameters:[20]

$$\eta_i I_{th} = \frac{etw_{eff}^E}{A_0 \Gamma_x^E}\left[\frac{1}{2}\ln\left(\frac{1}{R_1 R_2}\right) + (\alpha_l + \Gamma_x^E B_0)L\right] \qquad (5.4a)$$

Where η_i is the spontaneous emission factor, e is the electron charge, t is the thickness of the active region, w_{eff}^{E} its effective width, Γ_x^E the confinement factor (between 0 and 1, identify how much of the electric field of each lasing mode is effectively contained within the active region), α_l are the round-trip losses due to absorption and scattering, L is the length of the laser diode internal cavity, A_0 and B_0 are parameters related to the active material's gain curve. R_1 and R_2 are the reflectance of the front and back facet of the diode, respectively. All the parameters, however, can be grouped to rewrite **Equation 5.4a** in a much simpler form:

$$I_{th} = a[-\ln(R_1) + b], \qquad a = \frac{etw_{eff}^{E}}{\eta_i 2A_0\Gamma_x^E} \qquad b = -\ln(R_2) + 2(\alpha_l + \Gamma_x^E B_0)L \qquad (5.4b)$$

From **Equation 5.4b** is apparent that the threshold intensity should be proportional to the cologarithm of the front facet reflectivity.

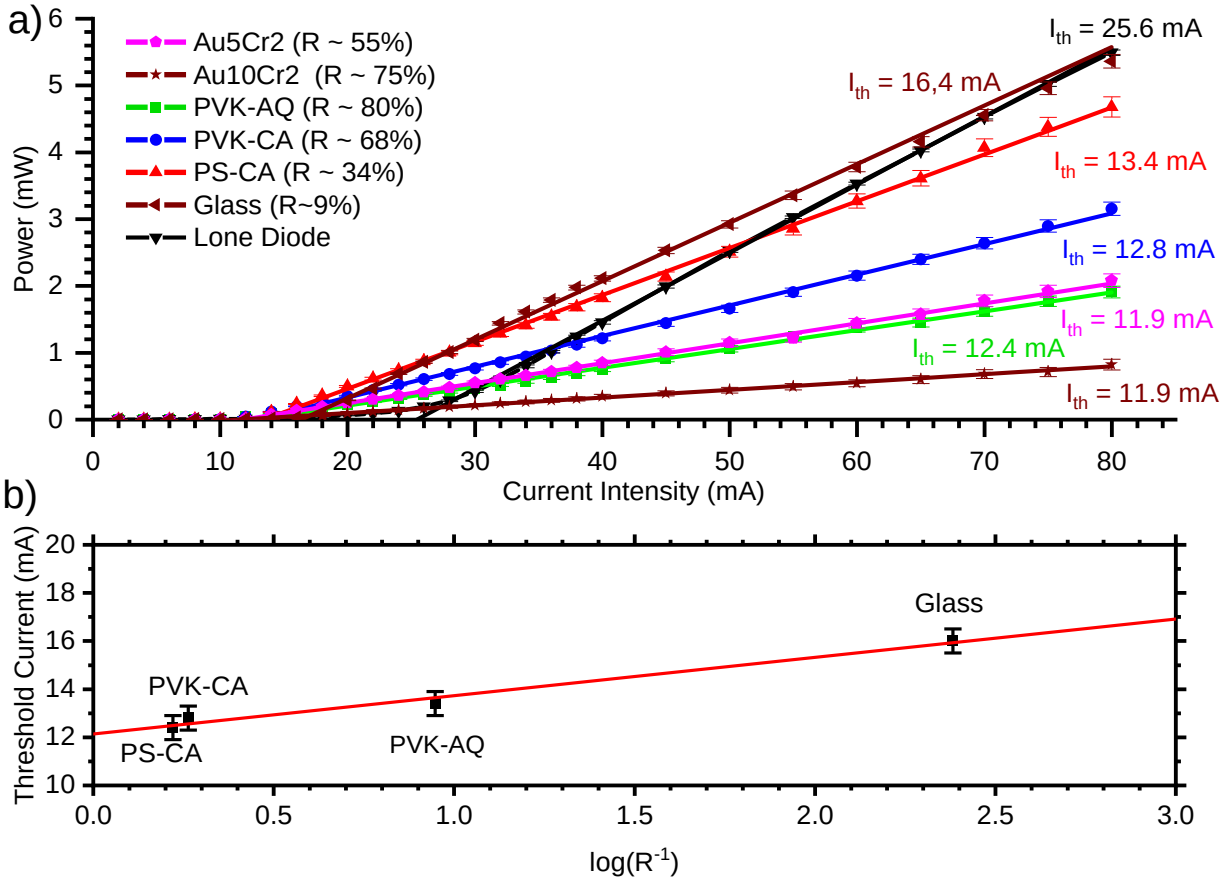

Figure 5.11. a) *L-I curves for the lone diode (black curve) and when feedback is provided to the diode with the various mirrors: the metallic ones Au10Cr2 and Au5Cr2 (magenta and light brown respectively) and the dielectric ones PS-CA (red curve), PVK-CA (blue curve), PVK-AQ (green curve) and bare glass (wine curve).* **b)** *Threshold current against logarithm of mirror reflectivity for glass and the dielectric mirrors.*

In the case of the ECL configuration, it is a decent approximation to consider the external mirror as a replacement to the AR-coated facet, since its reflectance is much greater. Threshold currents with respect to each mirror's cologarithm of reflectance are reported in **Figure 5.11b**. Due to its derivation, **Eq. 5.4b** can only be applied to compare mirrors with the same α_l; therefore, the metallic mirrors are not included in the plot. A linear fitting can reasonably be performed on the data, which are roughly aligned. From the fitting, the reflectance of the AR-coated facet can be extrapolated and results R ~ 0,03%, which is comparable to the typical values cited in the company's website. These results assess the functioning of the setup, which this way results the first report of a laser in ECL configuration using all-polymer mirrors as outcouplers.

The spectra of the light emitted by the diode in the ECL configurations were recorded using the different outcouplers that best satisfy **Equation 5.4b**. The measured data are reported in **Figure 5.12** as contour plots, with the current intensity passing through the diode as the y-axis, the wavelength as x-axis and the light output in logarithmic scale color coded as the colorbar. The spectra of the lone diode was reported in **Figure 5.3** and is not repeated. The spectra of the ECL with the dielectric mirrors (**Figure 5.12b, c, d**) shows a trend. Indeed, the central lasing mode is shifting towards longer wavelengths as the reflectance of the mirror gets higher, from PS-CA to PVK-CA and PVK-AQ. Overall, it seems that providing feedback narrows the span of active modes with respect to the lone diode, and causes an activation of more modes towards the shorter wavelengths region when the current passing through the diode increases. However, the effect of the glass substrate alone is essentially opposite (**Figure 5.12a**), as the central lasing wavelength starts in a very similar of the PS-CA mirror, but then shifts towards longer lasing wavelengths instead of shorter ones.

This behavior epitomizes the difficulty in consistently measuring the spectrum of the laser diode when in the external cavity configuration. Indeed, minimal changes in alignment of the outcoupling mirror, in the position of the lens or even changes in the current intensity passing through the diode change the final spectrum. Therefore, it is hard to extrapolate information from the spectra, apart from these general trends.

This happens probably as **Equation 5.4** implies that all the light reflected by the outcoupling mirror is effectively channeled back into the active region which is not the case with the current setup. Indeed, a slight change in the lens position (since the lens has 1.45 mm focal length, even micrometric changes due to vibrations) lead to a slightly different divergence of the collimated beam, which in turn cause the "effective reflectance" of the mirror to change. The same happens with the alignment of the mirror, which is finely regulated but limited by the size and pace of the ball-point screws and the friction between its components; additionally, the spectra itself may slightly influence the result as the collimating lens may suffer from chromatic aberration.

Notwithstanding these final considerations, the results here presented are significant, and promising in the application of all-polymer structures as outcoupling elements for lasers in ECL configuration. Additionally, the ECL assembly is performing overall remarkably well, which was the main goal of the project.

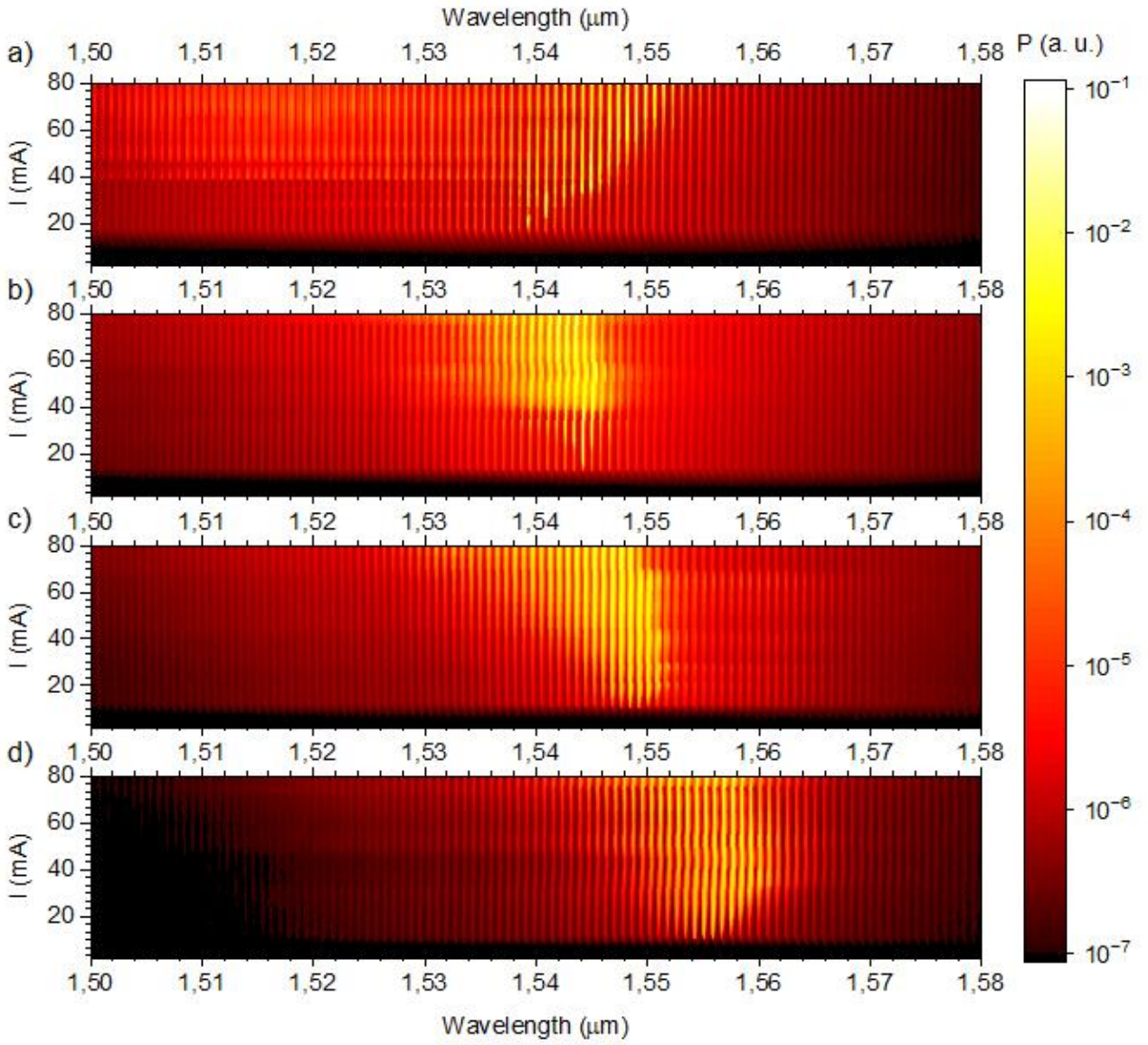

Figure 5.13. *Spectra measured at different current intensities when feedback is provided with bare glass* **(a)**, *or dielectric mirrors PS-CA* **(b)**, *PVK-CA* **(c)**, *PVK-AQ* **(d)**.

5.3 Conclusion.

Throughout the months of the project, I successfully laid the basis for a setup able to perform as an ECL. The setup can control temperature and current flowing through an AR-coated LD, collimating

it with a lens whose position is finely tunable. The lens can be changed to change the beam size and divergence. The setup integrates a custom-designed holder I designed, to hold any outcoupling element providing normal incidence feedback. Additionally, the holder could be easily modified to allow for feedback from an element acting out-of-normal incidence, such as a diffraction grating, just by introducing a rotating stage below the sample holder. The feedback is attainable even with low-reflectance optical elements such as bare glass, proving the fine alignment of the system. Notwithstanding the astigmatism of the diode and the challenge of attaining the aforementioned fine alignment, the DBRs presented in **Chapter 3** were effectively used as all-polymer NIR-reflecting outcouplers. This provided what is to my knowledge the first example of all-polymer photonic structures used in an ECL. A confirmation of the goodness of the apparatus resulted from linking threshold current with the reflectance of the various mirrors, which gave results according to laser theory as far as DBRs were concerned.

Although there are still points to be cleared and improved, such as the behavior of the LD's spectral output in ECL configuration, the results obtained in this project so far were interesting. Indeed, the introduction of all-polymer, flexible elements which can act as wavelength selectors in an ECL (such as all-polymer microcavities or stretchable mirrors – see **Chapter 6**) could contribute to new possibilities in designing (and perhaps reducing costs) this kind of systems.

Bibliography

1. B. E. A. Saleh , M. C. Teich, *Fundamentals of Photonics.* John Wiley & Sons, **2019**
2. H. A. Macleod, *Thin-Film Optical Filters, 5th Edition.* CRC Press, Boca Raton, FL (USA), **2017**
3. G. Giusfredi, *Manuale di Ottica.* Springer, Rome (IT), **2015**
4. M. Fleming , A. Mooradian. *IEEE J. Quantum Electron.*, **17**, 1, 44, (**1981**)
5. B. Mroziewicz. *Opto-Eletron. Rev.*, **16**, 4, 347, (**2008**)
6. Y. Fang, H. Cai, G. Chen , R. Qu, *Single Frequency Semiconductor Lasers.* Springer, **2017**
7. O. Svelto, *Principles of Lasers.* Springer, **2010**
8. RefractiveIndex.Info, Pettit and turner, https://refractiveindex.info/?shelf=main&book=InP&page=Aspnes (accessed December, 2024)
9. D. T. Cassidy. *J. Appl. Phys.*, **57**, 3, 987, (**1985**)
10. J. Sacher, *Coating process and apparatus*, US6869483B2 (**2002**)
11. M. Ettenberg, D. Botez, D. Gilbert, J. Connolly , H. Kowger. *IEEE J. Quantum Electron.*, **17**, 11, 2211, (**1981**)
12. C. Spägele, M. Tamagnone, D. Kazakov, M. Ossiander, M. Piccardo , F. Capasso. *Nat. Commun.*, **12**, 1, 3787, (**2021**)
13. S. Lasertechnik, Anti-Reflection Coated Laser Diodes, https://www.sacher-laser.com/home/laser-diodes/ar_coated_laser_diodes/ar_coated/anti-reflection_coated_laser_diodes.html (accessed December, 2024)
14. J. Sacher, *Coating process and apparatus*, US6297066B1 (**2001**)
15. P. Lova, G. Manfredi , D. Comoretto. *Adv. Opt. Mater.*, **6**, 24, (**2018**)
16. E. Hecht, *Optics, 5th Edition.* Addison-Wesley, London (UK), **2017**
17. A. Lanfranchi, H. Megahd, P. Lova , D. Comoretto. *Chem. Eng. Sci.*, **283**, 5, 119377, (**2024**)
18. P. Lova, H. Megahd, P. Stagnaro, M. Alloisio, M. Patrini , D. Comoretto, *Appl. Sci.*, 10, **2020**
19. H. Megahd, C. Oldani, S. Radice, A. Lanfranchi, M. Patrini, P. Lova , D. Comoretto. *Adv. Opt. Mater.*, **9**, 5, 2002006, (**2021**)
20. W. Streifer, D. R. Scifres , R. D. Burnham. *IEEE J. Quantum Electron.*, **18**, 1918, (**1982**)

Chapter 6 – Other Projects

Abstract

Chapters 2-5 of this thesis included the work I performed during these years regarding the main topics of research, photonics structures for thermal shielding and radiative cooling, as well as the use of the same structures for physics-oriented applications such as the assembly of an external cavity laser setup. However, I also worked on side-topics collaborating with colleagues, both internally to the research group as well as externally to it. In this final chapter I will briefly introduce these topics, with a special focus on the role I invested in the various projects. For the full picture on each work I suggest looking at the reference paper (where available), as information reported here is incomplete:

- **Subsection 6.1** covers the fabrication of red-reflecting mirrors for on-chip sensing (project in collaboration with the CNR of Bologna), that led to Benvenuti et al., *J. Mater. Chem. C* **2024**, 12, 12, 4243;[1]
- **Subsection 6.2** covers the use of photonic structures for emission control and radiative rate modification, that led to Megahd et al., *ACS Omega* 2024, **7**, 18, 15499 and *Mater. Chem. Frontiers* 2022, **6**, 17, 2413;[2, 3]
- **Subsection 6.3** covers the use of all-organic photonic structures for strong light-matter coupling. Di Fonzo et al., *in preparation*;
- **Subsection 6.4** covers the use of photonic structures as sensors of chemicals in vapor phase (Magnasco et al., ACS Omega 2024, **9**, 41, 42375)
- **Subsection 6.5** covers the fabrication of elastomeric DBRs which change color when strained, viable as strain and stress sensors (Martusciello et al., ACS *Appl. Mater. Interfaces* 2024, **16**, 38, 51384);[4]
- **Subsection 6.6** covers the integration in 3d printing workflow of thermal IR analysis (Baouch et al., *Add. Manufactur*, 2024, 83, 31, 104063);[5]
- **Subsection 6.7** covers the conversion of a 3d-printer into a dip-coating machine for the automated fabrication of photonic structures (Martusciello et al., *in preparation*).

6.1. DBRs as signal-to noise enhancers for all polymer integrated sensors.

From **Chapter 5** it clearly emerged as, although in this work I used photonic structures as near infrared reflectors for thermal shielding, they are fully functional mirrors working for restricted wavelength ranges. Due to this, I could lend the expertise accumulated over the years in the fabrication of distributed Bragg reflectors (DBRs) for a joint project with Consiglio Nazionale delle Ricerche of Bologna, led by Dr. S. Toffanin and Dr. M. Bolognesi. In the frame of this project, I designed and fabricated red reflecting mirrors to improve the sensitivity of an on-chip sensor for analytes in liquid phase.[1]

A schematic of the integrated all-organic sensor is represented in the inset of **Figure 6.1a**. An organic light-emitting diode (LED, red layer) emitting red light (red arrows) is used to excite a solution of a fluorescent dye (FS, azure layer). This emitted light (violet arrow) is then collected by an organic photodiode layer (OPD, green layer) placed below, and the intensity of the signal is evaluated to quantify the molecule concentration in the liquid. Part of the red light is reflected back at the sensor-liquid interface decreasing strongly the signal-to-noise ratio of the measurement. Here, the role of the DBR is to provide a filter in front of the photodiode, reducing the source signal coming back and increasing the signal-to-noise ratio of the measurement. This is done by finely tuning the photonic bandgap of the DBR in such a way it strongly reflects the light from the LED; placing it between the LED and the photodiode, as per the schematics represented.

6.1.1. Fabrication of DBRs. The starting idea of the project was to fabricate the DBRs directly on top of the photodiode. To do so, the photodiode was capped with a protective layer made of Cytop, a perfluorinated polymer similar to Hyflon or Teflon. The presence of the perfuorinated polymer requires a plasma treatment to activate the surface and make deposition via spin-coating feasible.[6] Initially, poly(*N*-vinylcarbazole) (PVK) and cellulose acetate (CA) were selected for the alternating layers, and DBRs consisting of 10 layer pairs were fabricated. However, the first batches showed an irreversible degradation in the performances of the photodiode when the DBR was deposited on top, with an increase of the dark saturation current and a decrease of sensitivity. Thinking this was due to the thermal treatment to avoid percolation of CA's solvent in PVK layers, CA was replaced with Aquivion (AQ).[7] However, avoiding the thermal treatment did not solve the issue. Presumably the encapsulation layer was not enough to protect the delicate structure of the photodiode from the solvents used during the spin-coating process. Henceforth, I exploited the flexibility of all-polymer DBRs to fabricate them on flexible substrates (made out of polyethylene terephthalate, PET; the common screen-protecting films). The DBRs on substrates were then cut down to the right size and

glued onto the photodiode. The LED was afterwards fabricated on top. The reflectance over 9 points of the DBRs is showed in **Figure 6.1a**, which displays the photon bandgap as a wide reflectance peak centered around 660 nm; this allows to effectively reflect light from the LED.

6.1.2. Performances of the integrated sensors. The performances of the sensors are represented in **Figure 6.1b**, which reports the signal to noise ratios in the cases with and without DBR for different dye concentrations. It is apparent that the signal to noise ratio is increased around three times when the DBR is introduced, granting a performance enhancement to the sensor. Able to detect minimal concentrations, this cheap all-organic integrated platform is extremely promising for on-site detection of analytes.

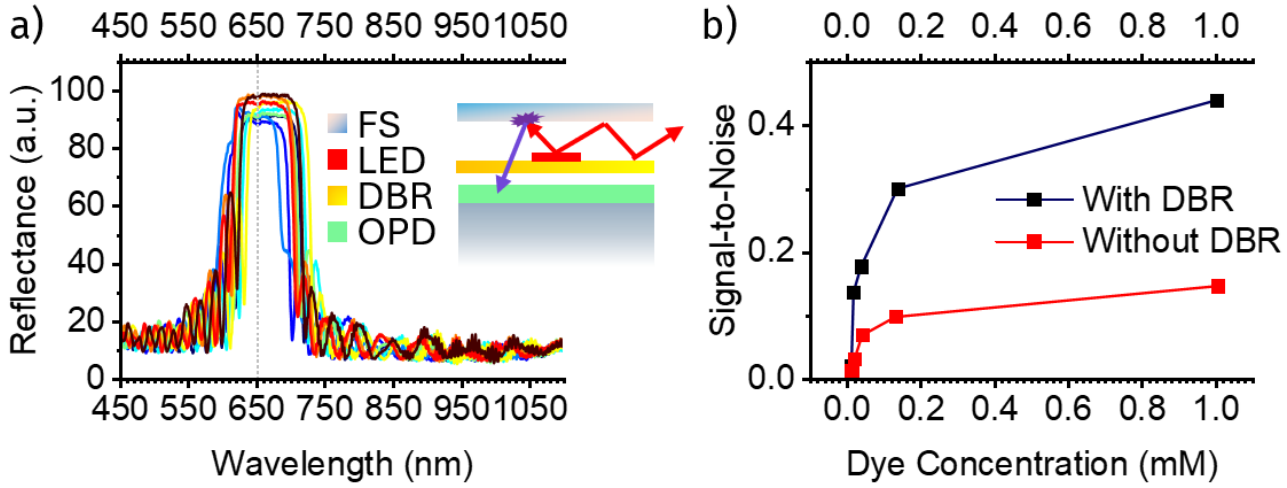

Figure 6.1. **a)** *9-points reflectance of the DBR placed on the structure. In the inset, schematic representation of the on-chip sensor (FS: fluorophore solution, LED: organic LED, DBR: distributed Bragg reflector, OPD: organic photodiode).* **b)** *Comparison of the signal to noise ratio for different dye concentrations with the on-chip sensor with (black line) and without (red line) the DBR.* Data from [1]

6.2. DBRs for emission control and lasing.

6.2.1. Optical Microcavities. In **Chapter 5**, DBRs were used as lossless mirrors to create an external cavity for a laser assembly. In that case the cavity was composed by the high reflectance back facet of the laser diode on one side and a polymer DBR on the other. However, since DBRs are full-fledged mirrors, two DBRs can be used to form an optical cavity by themselves.[8-11] Indeed, a schematic of an example optical microcavity is represented in **Figure 6.2a,** in this case made out by two DBRs 20 bilayers each. The latter are fabricated out of PVK and AQ with a capping CA layer;[3] in the center, they sandwich a layer of polystyrene/diketopyrrole pyrrole dye (DPP) blend.[12] The two mirrors effectively form a Fabry-Pérot optical resonator.[11, 13]

Therefore, the microcavity shows permitted modes for the photon to propagate through the structure in the bandgap region (cavity modes).[8, 14] Indeed, **Figure 6.2b** shows the transmittance spectrum of the microcavity represented in **Figure 6.2a**. The overall spectrum is similar to that of a standard DBR (see **Chapter 1, Figure 1.2** for reference), showing a low-transmittance plateau due to the photon bandgap, surrounded by the interference fringes region. However, at the wavelength labeled λ_C, the transmittance rises almost to 1 despite being still inside the bandgap. That wavelength is indeed the cavity mode, where photon propagation is allowed through the structure.[10]

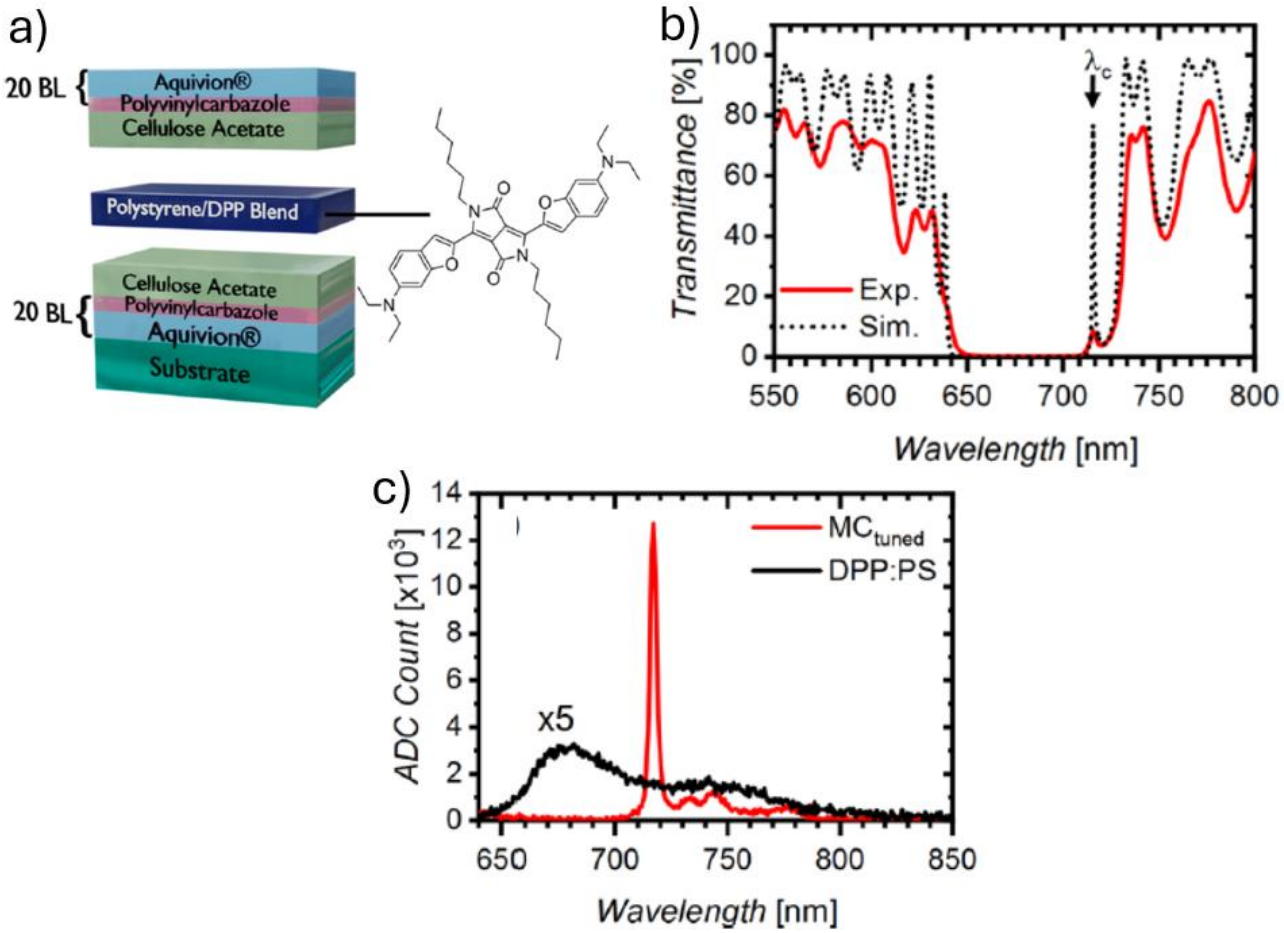

Figure 6.2. **a)** *Schematic representation of an optical microcavity and structural formula of the dye.* **b)** *Measured transmittance of the structure (red line) and calculated one (black dotted line). Arrow points to the cavity mode.* **c)** *Photoluminescence spectra of the dye blend (black line) and the microcavity (red line). The dye blend intensity is magnified 5 times.* Adapted from [3]

The main interest of optical microcavities is their effect on the local photon density of states. Indeed, in correspondence to the cavity mode the photon density of states is drastically enhanced whereas corresponding to the bandgap it is reduced essentially to zero. This spike in the photonic density of states comes into play when the defect layer is filled with a photoluminescent material, such the polystyrene-DPP blend in the example reported in **Figure 6.2a**. In this case, the effect is reported in **Figure 6.2c**. The emission spectrum of the fluorophore (black line) undergoes a spectral

redistribution according to the photonic density of states – therefore getting suppressed in correspondence to the bandgap and vastly increased in correspondence to the cavity mode (red line). This spectral redistribution with the possibility of reducing the width of emission leads to a great potential for this kind of structures in a variety of fields, mainly for the purpose of lasing.[7, 15]

6.2.1. Optical Response Calculation and Physical Characterization. The microcavity used so far as an example was fabricated by H. Megahd as part of the work leading to the publication Megahd et al., *ACS Omega* **2022**. I personally calculated the optical response of the microcavity (reported in **Figure 6.2b** as a black dotted line). The good agreement with respect to the experimental curves certifies the high-quality of the fabrication, which in this case led to a record enhancing of the photoluminescence (for all-polymer microcavities).

A physical characterization of the sample was performed via scanning electron microscopy (SEM), leading to the result reported in **Figure 6.3a**. The cross section of the structure clearly shows the different layers, AQ being composed of small spheres and PVK being more compact. This makes sense as AQ is indeed a water-based dispersion instead of a polymer solution. To analyze the picture, I designed a custom algorithm. The image matrix, is firstly averaged over rows; a vertical profile is hence obtained (**Figure 6.3b**, upper panel, black line). The layers can be identified as AQ (brighter hence more intense, and more irregular) and PVK (darker hence less intense and more spike-like). Due to the nature of the SEM analysis, the profile is not flat; a background correction with an adequate polynomial function is applied to obtain a flattened profile (lower plot, black). The flattened profile is then cut at 0 value, considering anything over being AQ and anything below being PVK. A square-like profile yielding the thicknesses of the layer is then obtained. There may be a systematic error in this analysis (the cutoff y value assumed as 0 may be higher or lower); nonetheless, it was preferred as manual analysis risked bias.

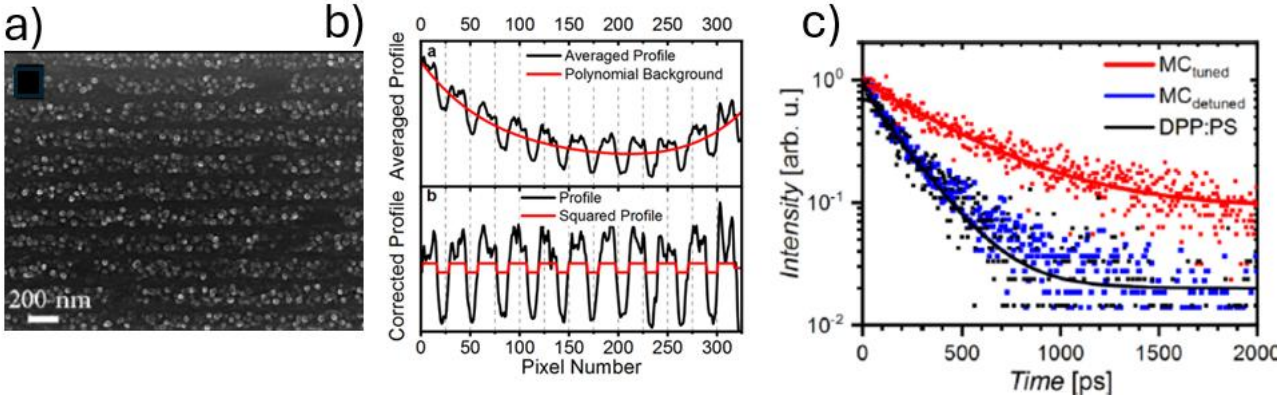

Figure 6.3. **a)** *SEM micrograph of the sample microcavity.* **b)** *Workflow of the SEM micrograph analysis.* **c)** *Radiative rate decay curves for the optical microcavity (red curve) the dye blend film (black curve) and a suitable reference for the dielectric environment of the microcavity (blue curve).* Adapted from [3]

6.2.1. Radiative Rate Modification. The most considerable result of the paper was the first report in literature of a consistent modification in the radiative rate of emission in an all-organic optical microcavity. Indeed, in **Figure 6.3c** I report the decays in photoluminescence as measured via time-correlated single photon counting. The steeper the decay, the faster the system is deexciting decaying to its ground state. It is apparent that the presence of a tuned optical microcavity (MC_{tuned}) leads to longer radiative rate and a less steep decay (red line) with respect to the dye blend alone (black line). In turn a reference made up by a similar dielectric environment but without the increase in photon density of states ($MC_{detuned}$) does not show a consistent time increase, certifying the effect of the microcavity. This result is especially important in the perspective of lasing from all-organic, flexible microcavities.[3]

6.2.1. Near-Infrared Emitting Dyes. The approach described so far was used to achieve radiative rate modification in a dye emitting in the near-infrared region, with its structure represented in Figure 6.4a.[3] The dye was embedded in poly (acrylic acid) matrix and used in an optical microcavity pictured in **Figure 6.4b** and represented in **Figure 6.4c**. The microcavity is formed by two DBRs, 20 bilayers each of PVK-AQ which sandwich the defect layer and is remarkably transparent in the visible range as seen in the picture. This is explained by looking at the transmittance spectrum of the microcavity, reported in **Figure 6.4d** (black line); the sample is transparent in the visible range (400-700 nm), as its photon band gap is in the near infrared region, around 800 nm. The good quality of the microcavity is made apparent by the calculation of the optical response I performed, reported in the same **Figure6.4d** as a grey line.

The microcavity is effective in redistributing and enhancing the photoluminescence of the dye, as shown in **Figure 6.4e**; the spectrum of the microcavity (red line) is strongly peaked in correspondence to the cavity mode (around 850 nm as seen from the transmittance measurements). Instead, the spectrum of the dye is wide, bell-shaped curve peaked around 800 nm. The $MC_{detuned}$ spectrum is a reference to guarantee the dielectric environment is not influencing the emission by itself.

The microcavity is even affecting the radiative rate, as in **Paragraph 6.2.1**. Indeed, in **Figure 6.2f** are reported the decays for the reference (blue line) the dye embedded in the film (black line) and the microcavity (red line). The radiative rate is increased by the presence of the dielectric environment, as per the reference, but the microcavity has a much stronger effect. This result is of particular significance as it is the first instance of an all-organic microcavity altering the radiative rate of a near-infrared emitting dye.[2]

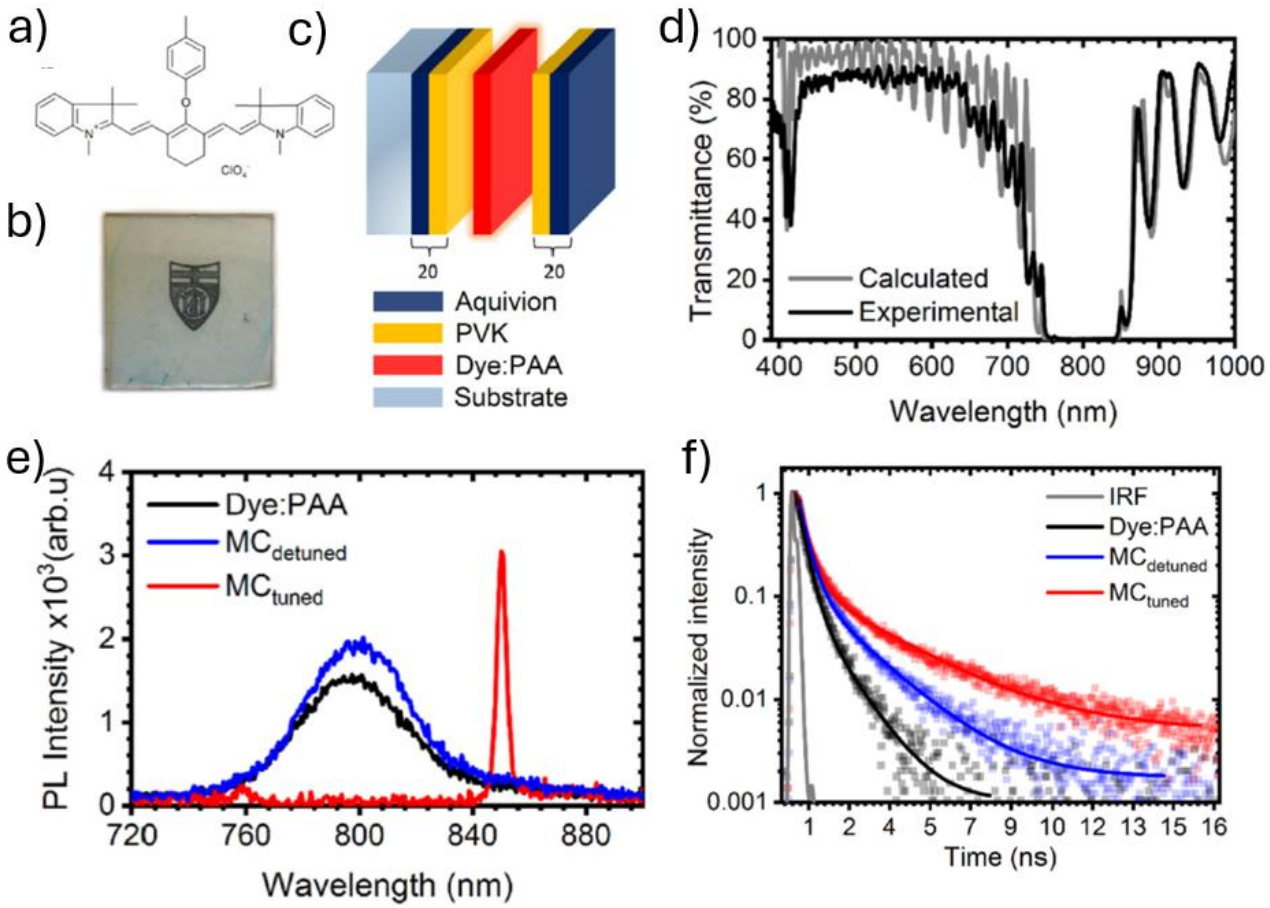

Figure 6.4. **a)** *Structure formula of the near-infrared emitting dye.* **b)** *Picture of the sample over a UniGe logo.* **c)** *Schematic of the optical microcavity.* **d)** *Calculated (grey line) and experimental (black line) transmittance spectrum of the near-infrared tuned microcavity.* **e)** *Photoluminescence spectra of the dye embedded in PAA (black curve), the suitable reference (blue curve) and the optical microcavity (red curve).* **f)** *Radiative rate decay curves for the optical microcavity (red curve) the dye blend film (black curve) and a suitable reference for the dielectric environment of the microcavity (blue curve). The instrument response function (IRF) is reported as a grey line.* Adapted from [2]

6.3. Strong Coupling in All-Organic Microcavities.

6.3.1. Introduction. When an adequate dye is placed inside a microcavity, it can lead to an effect known as strong coupling.[14-16] For the phenomenon to happen, the incident photon must excite an electronic state of the dye promoting it to an upper level – which then must spontaneously decay emitting a photon. Due to the confinement provided by the microcavity, the emitted photon is immediately re-absorbed, then immediately re-emitted, and so on and so forth. This continuous cycle causes the electronic and photonic states to mix.[17, 18] Indeed, the two particles are considered a single quasiparticle called polariton. Since polaritons are bosonic in character, they obey Bose-Einstein statistics instead of Fermi-Dirac one and can form Bose-Einstein condensates. This could lead to high

level applications such as ultra-low threshold lasers, and replacement of electronics with polaritonics.[16, 19]

6.3.2. Results and Discussion. In the case of my work, I fabricated optical microcavities out of PVK and AQ to have a sufficiently high dielectric contrast. As dye, I used a cyanine dye known as TDBC (whose structure is represented in **Figure 6.5a**) in the form of J-aggregates embedded in a poly (vinyl alcohol) matrix.[20] J-aggregates are essentially supramolecular structures in which the dipole positioning of the single molecules lead to an enhanced interaction with electromagnetic radiation and usually to extremely narrow and intense absorption/photoluminescence.[14, 15] **Figure 6.5b** shows the absorption (red line) and PL (black line) spectrum of a diluted solution of TDBC in water. The broad peak around 510 nm correspond to the absorption of the molecule, whereas the narrow absorption at 589 nm corresponds to the J-aggregates – which in turn are responsible for the strong and narrow photoluminescence. In the solid film (**Figure 6.5c**), the absorption of the molecule is no longer observed, and only the absorption of the J-aggregates is apparent. Compared to typical dyes such as those reported in **Subsection 6.2**, the emission is much narrower, with a full width at half maximum around 20 nm.

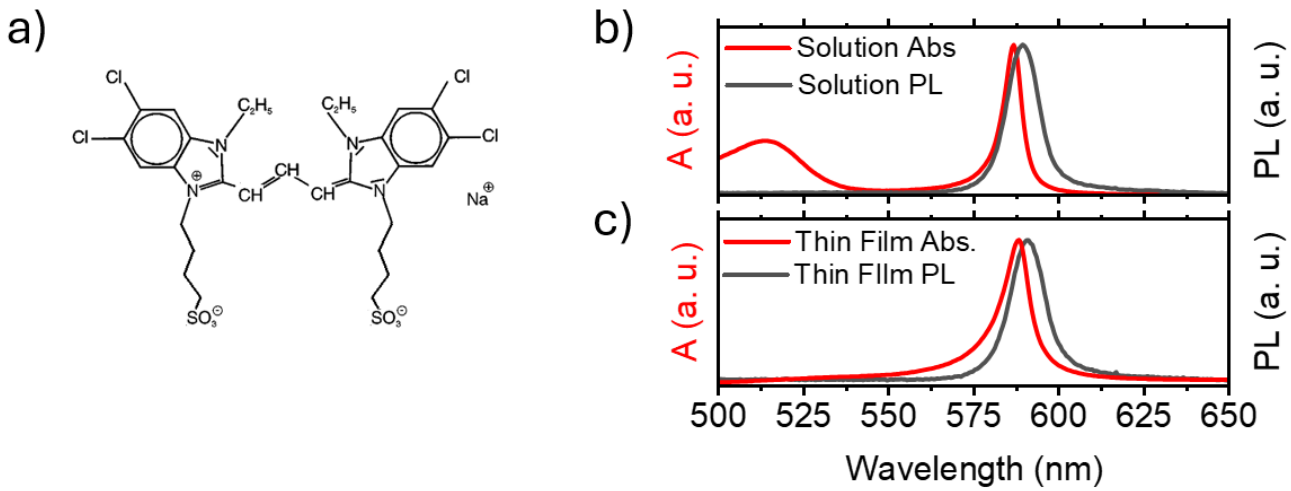

Figure 6.5. **a)** *Structure formula of TDBC.* **b-c)** *Absorbance (red line) and photoluminescence (black line) spectra of* **b)** *a diluited TDBC solution in deionized water and* **c)** *of the solid film with TDBC embedded in a PVA matrix.*

Figure 6.5a reports, as stacked plots, the measured transmission spectrum at various angles as a function of wavelength and energy for a TDBC-containing microcavity made out by 5.5 BL of PVK and AQ per mirror. The behavior for the most part follows what expected by Bragg-Snell law, with the spectrum shifting towards higher energies (shorter wavelengths). However, following the cavity mode (dotted black line) yields a small but consistent anticrossing in correspondence to the excitation wavelength of TDBC (grey line). Indeed, the cavity mode does not cross the grey line, but instead splits in two peaks. The peaks should correspond to the polariton branches, which effectively

substitute cavity mode and electronic absorption as well. A similar behavior is observed in the calculated spectra, reported in **Figure 6.6b**. In this case, the splitting is more pronounced, but the width is similar. The data suggest a Rabi splitting at the anticrossing point of around 36 meV for the measured spectra and 45 eV for the calculated ones.

From this point onward, I mostly dedicated to supervision, theoretical modeling and help with sample design and characterization. The work was taken over by my colleague D. Di Fonzo, who is currently writing a paper on the subject. In general, however, the results are extremely promising as the first-ever reported evidence of strong light-matter coupling in all-organic microcavities.

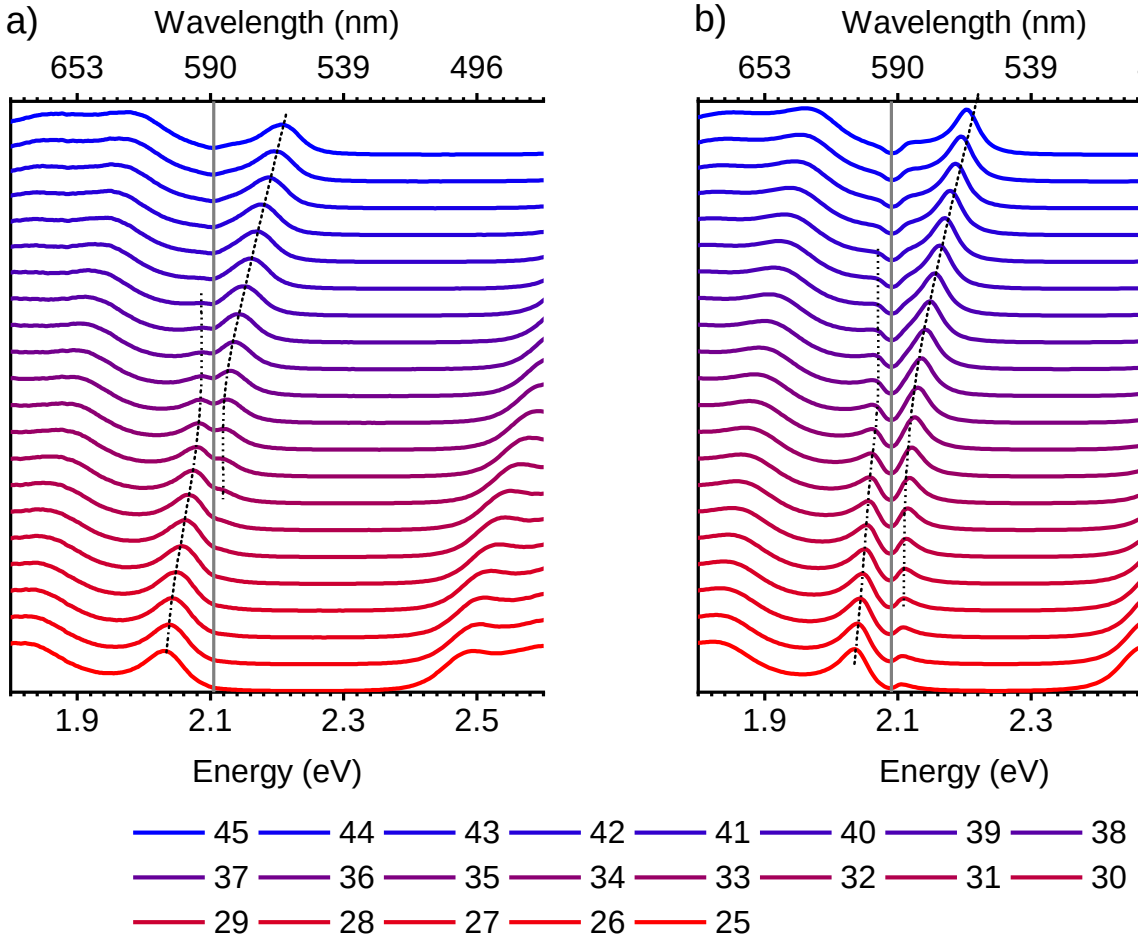

Figure 6.6. **a, b)** *Experimental (a) and calculated (b) transmittance spectra for the TDBC-containing microcavity at progressively increasing angles, as per the legend. The absorption of the dye is indicated by the grey line, the position of the cavity mode/polariton branches by the black dotted lines.*

6.4. Microcavities for Analyte Sensing.

Bragg-Snell law (**Equation 1.1**) especially in its simplified form (**Equation 1.2**), states that the position of the photon band gap is dependent on the layer thicknesses and refractive index. This means

that changing either of them causes a variation in the position of the bandgap. If the structure is tuned to show the bandgap in the visible range, a change in its spectral position means a change in the resulting color of the structure. The latter can be easily observed by naked eye, if consistent enough, or quantified with a cheap spectrophotometer. However, the refractive index varies little under normal circumstances, especially for polymer materials. The thickness of the layers, on the other hand, is easier to change. For example, polymers can swell upon absorption of solvents; this means an increase in their thickness and in turn an increase of the wavelength value where the bandgap is observed. This led to many publications from the research group over the years (including one I co-authored during my Master's thesis, Megahd et al., *Advanced Optical Materials* **2021**).[21]

The work of a Master's student (L. Magnasco) I collaborated to supervise led to the fabrication of optical microcavities used for sensing instead of traditional DBRs (Magnasco et al., *ACS Omega* **2024**).[22] This work used the diketopyrrole pyrrole dye used in the previous **Subsections 6.2** and **6.3.** Its structure formula is reported in **Figure 6.7a**, whereas pictures of the blend under white light and violet laser are reported in **Figure 6.7b-c** respectively, emphasizing the turquoise color of the dye turning to a bright red emission. The dye was embedded in PVK-AQ microcavities (schematically represented in **Figure 6.7d**) and used to absorb and detect analytes in vapor phase. My personal contribution was supervising the student, designing and assembling the experimental setup and providing software assistance for fitting the measured optical responses of the structures.

6.1.2. Assembly of the experimental setup. Fluorescence measurements of the microcavities needed to be performed across relatively long timeframes to check the evolution of the fluorescence spectrum over time upon absorption of the analytes. The dye used to fabricate the microcavities, however, suffered quenching of fluorescence upon irradiation. Therefore, some way to provide momentary irradiation – only in correspondence to the measurement – was needed. This was achieved by assembling a setup based on an electromechanical shutter.

A function generator produces a square wave of digital signal (amplitude 0 –5 V) whose frequency and duty cycle can be adjusted at discretion. The signal was relayed to the shutter as well as two spectrophotometers, one receiving white light-transmission measurements and the other receiving the photoluminescence signal. On the "high" of the square wave, the shutter is opened. The sample is irradiated with the green laser and the photoluminescence is measured, the white light transmission measurement is performed simultaneously with the second spectrophotometer. Adjusting the "low" time with respect to the "high" one allows to perform sporadic measurements avoiding the fluorescence quenching.

6.1.2. Results and Simulations. Thanks to the experimental setup assembled this way, the measurements could be performed as reported in **Figure 6.7e-h**. **Figure 6.7e** and **g** represent

respectively the transmittance spectra of the microcavities over time as the structure absorbs vapors of acetone (**e**) and dichloromethane (**g**). Overall, the behavior is relatively smooth, with the bandgap shifting towards longer wavelengths progressively according to the swelling of the layers. The first minutes, especially in the acetone case, are characterized by a splitting of the PBG. This is due to the progressive diffusion of analytes in the structures, making the layers of the microcavity swell asymmetrically and become sort of a tandem structure for a while (for tandem structures, see **Figure 1.6b**). The same changes are apparent in the fluorescence measurements (**Figure 6.7f**, **h**); the original red photoluminescence of the dye is redistributed spectrally by the presence of the microcavity (at time 0). Then, as the microcavity changes its optical response, so do the fluorescence. These results are interesting in the field of analyte label-free sensing, as optical microcavities have a different response to different substances and respond even to small amounts due to the sensitivity of the structure.

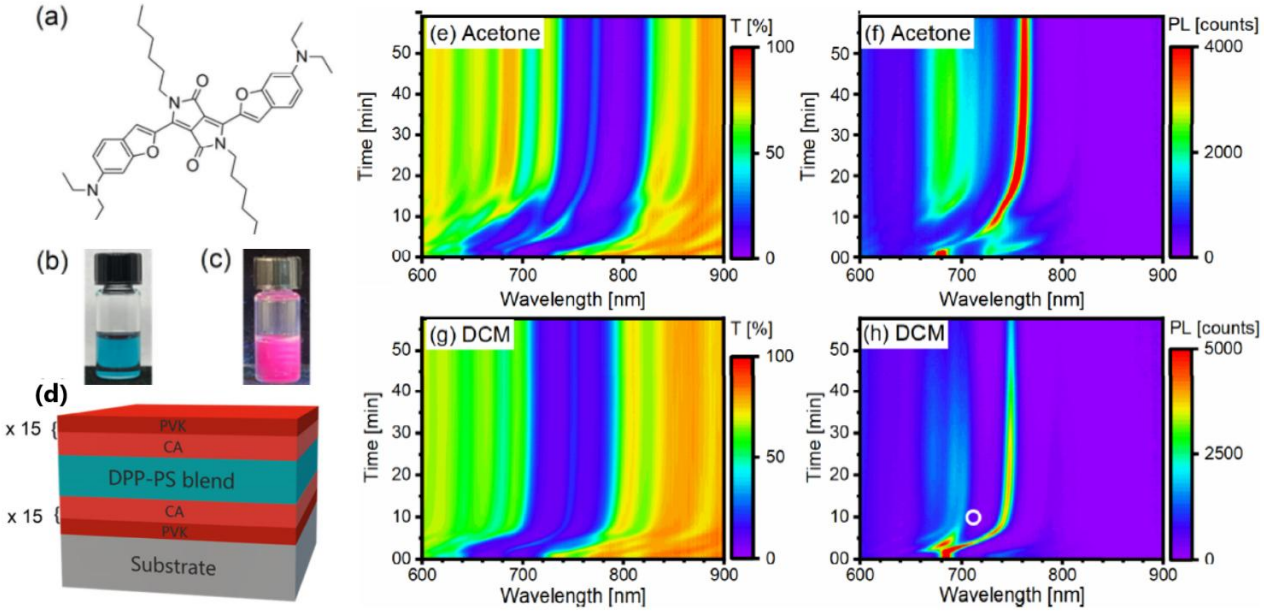

Figure 6.7. **a)** *structure of the diketopyrrole pyrrole derivative used as dye in the experiment.* **b)** *picture of the dye:polystyrene solution in toluene under white light and* **c)** *when excited via the violet 405 nm laser.* **d)** *schematic of the microcavity used in the experiment (DPP: diketopyrrole pyrrole, PS: polystyrene, PVK: poly(N-vinylcarbazole), CA: cellulose acetate).* **e, f)** *transmittance and fluorescence of the structure over time when exposed to acetone.* **g, h)** *transmittance and fluorescence of the structure over time when exposed to dichloromethane*. Adapted from [22]

6.5. Elastomeric DBRs as Strain-Stress Sensors

Another effective way to change the thickness of the layers of a DBR is to pull the structure straining it. Indeed, as easily observed with rubber bands, the increase of length corresponds to a decrease in thickness of the structure – which for DBRs translates to a variation in the thickness of

the layers and blueshifts the spectral position of the peaks. The main obstacles to this result are the materials used, as common polymers cannot sustain elastic, reversible strains greater than a few percent.[23] On the other hand, chemically crosslinked elastomers are not soluble and not compatible with the fabrication method of DBRs.[24]

Despite these challenges, my colleague M. Martusciello fabricated DBRs made out of elastomeric materials, combining a high-refractive index block copolymer (styrene-butadiene-styrene type) with a perfluorinated polymer (PFR). The block copolymer relies on physical reticulation, the chains interlocking without chemical bonds, whereas PFR is not reticulated. This allowed to fabricate DBRs which change color when strained without breaking, as reported in the pictures of **Figure 6.8a**.[4]

6.1.2. Measurement setup. To perform transmittance and reflectance measurements upon increasingly greater values of strain I designed, 3d-printed and assembled a system as reported in **Figure 6.8b.** The system is made up of two clamps with silicone jaws mounted on rails; two metric screws allow to pull the sample millimeter by millimeter apart from each other, providing a controlled way to perform reflectance and transmittance measurements over increasing strains.

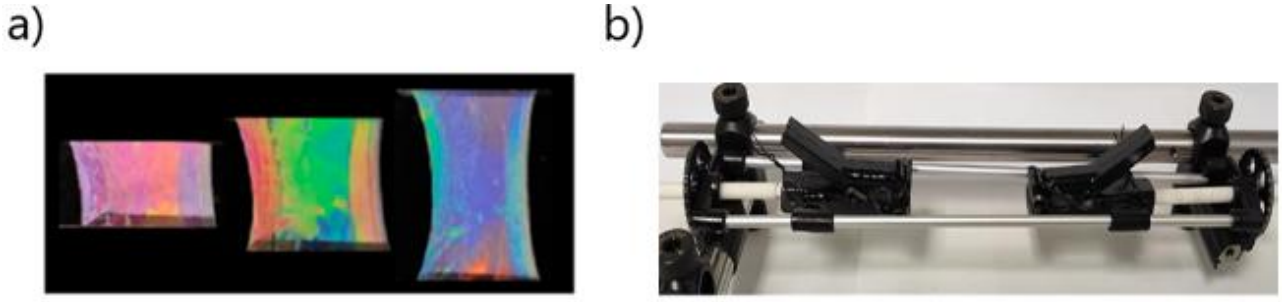

Figure 6.8. **a)** *Pictures of mechanochromic DBR in various stage of straining.* **b)** *Picture of the cad-designed, 3d-printed setup to pull the samples.* Adapted from [4]

6.4.2. Results. Thanks to the measurement setup, reflectance measurements at normal incidence could be performed over increasing strains. The reflectance spectra of the sample from 0 to 400 % strain are reported in **Figure 6.9a**, emphasizing the progressive blueshift when the strain rises from 0 % (violet curve) to 400 % (yellow curve). The system afterwards is relatively reversible and does not break even upon such a large strain. The red dashed lines follow the theoretical position of the photon band gap according to the model developed in the paper, that is in good agreement with the experimental results.

Measurements at selected angles were fitted with the calculations using the MatLab codes I developed, as reported in **Figure 6.9b**, to a good agreement. The differences are mainly due to the substrate, as the interference pattern due to the thin substrate is not present in the calculation. The good agreement with the calculated spectra allowed to track the position of the band gap as a function of the calculated layer thickness (as reported in **Figure 6.7c**), which yield a linear dependence as

expected from Bragg-Snell law. On the other hand, the dependence of the bandgap spectral position upon strain as reported in **Figure 6.7d** is nonlinear and goes according to an inverse square root law.

I reported few selected results from this extensive work. Indeed, the overall results obtained are very significant, as the first reported evidence of stretchable, mostly reversible DBRs. Note that the results are supported by a complete model, which I did not report. This work paves the way to the integration of mechanochromic sensors based on DBRs in fields such as structural and health monitoring.

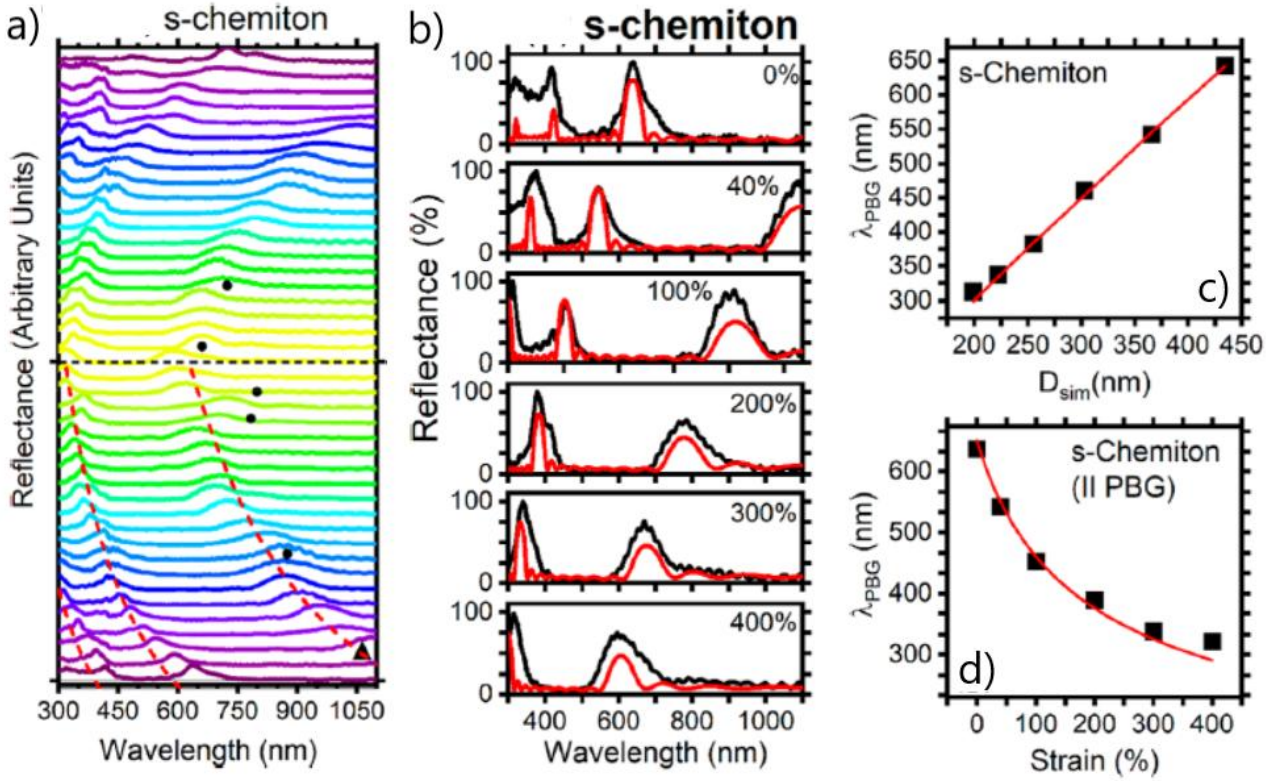

Figure 6.9. **a)** *Picture of the cad-designed, 3d-printed setup to pull the samples.* **b)** *picture of the setup as integrated with reflectance fiber probe for normal-incidence reflectance measurements.* **c)** *pictures of mechanochromic DBR in various stage of straining.* Adapted from [4]

6.6. Thermal analysis of 3D-printing processes.

The expertise I developed with the monitoring of temperature – as reported in Chapters 2-3 – allowed me to collaborate with the team of Prof. D. Cavallo at UniGe in a project studying the 3d printing process of polypropylene.

6.5.1. Fused Deposition Modeling. Fused Deposition Modeling (FDM), the most common form of 3d printing, is a process where a polymer filament is heated up in a moving head and extruded through a nozzle to form a solid line; the stacking of lines and profiles one on top of the other in subsequent planes yields the final object. The filament is extruded at a relatively high temperature to

ensure the viscosity of the melt is low enough. This means the layers undergo a cooling once they are deposited on the building plate, and the form of the final object can therefore be affected by warpage due to the release of internal stresses in the cooling polymer. With amorphous polymers, which undergo relatively little contraction due to cooling, this is a preventable issue – usually precise plate leveling, heating up the plate and spraying some adhesive is enough. However, polymers friendly with the 3d printing process have usually reduced mechanical characteristics with respect to semicrystalline ones.[25, 26]

Isotactic polypropylene is a widely used semicrystalline polymer which is difficultly compatible with the 3d printing process due to excessive warpage preventing the reliable fabrication of complex parts. The investigations on the physical reasons behind these issues using accurate models, such as that reported in the paper I co-authored (Baouch et al., *Additive Manufacturing* 2024[5]), required knowing the temperature history of each layer during the printing process.

6.5.1. Thermal measurements. Thermal cameras integrate blackbody radiation coming from samples to derive their temperature via reversing Stefan-Boltzmann law. This provides a relatively low accuracy but an extremely high spatial sensitivity (in the order of magnitude of millikelvins). A single movie of the 3d printing process can therefore assess the temperature of each point of each layer over time, knowing precisely the thermal history of the cooling polymer. I report an example of a thermal picture of the printing process in **Figure 6.10**. Each pixel's temperature over time can be extracted allowing to know the temperature history of the polymer in each zone of the structure, improving the understanding of the process.

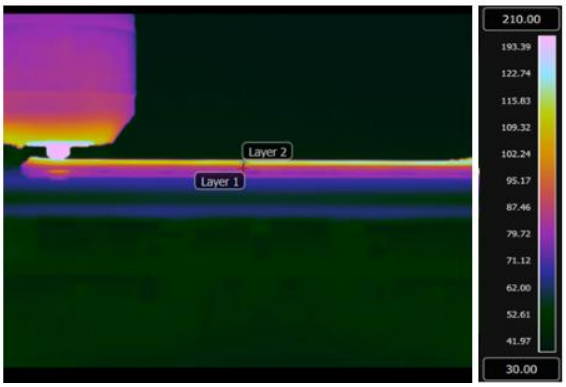

Figure 6.10. **a)** *Stop-motion of a thermal video of the 3d-printing process.*

6.7. Dip-Coating systems for all-polymer DBRs.

I co-supervised a student from Sigma-Clermont University, C. Hervieu, on a project performed in the university of Genoa. The goal was to convert a commercial 3d printer in a dip-coater for the fabrication of all-polymer distributed Bragg reflectors.

Dip coating is a method commonly used for the fabrication of thin films. It consists simply in the immersion of a substrate in a casting solution of known concentration; the controlled withdrawal of the substrate from the solution yields the formation of a thin liquid film from the meniscus, and the evaporation of the solvent leads to the formation of the final film. The thickness of the film depends on the concentration of the initial solution and the withdrawal speed, but also on the evaporation rate of the solvent which may depend on environmental conditions.[27, 28] Usually, dip-coating machines are relatively expensive and not suited for the fabrication of DBRs being limited to uniaxial movement – they can only dip in a solution at time, which should be manually changed by an operator each time to fabricate alternating layers.

A 3d printer, on the other hand, is by definition capable of triaxial movement – nothing stops it to travel between two (or more) solutions dipping alternatively in each of them. Therefore, we modified the printer substituting the extruder head with a clip to hold glass substrates. I designed and 3d printed the clip out of acrylate resin. However, the printer needs a file containing a series of codified instructions to perform its actions. To fabricate a DBR the head must go down (to dip in the first solution), then go up at a fixed speed, wait for the drying time of the film and move to the position of the second solution. The repetition of these steps form a complete DBR. Therefore, I wrote a MatLab code allowing to write the G-code necessary to move the printer from simple parameters (drying time, withdrawal speed, solutions level).

6.5.1. Results. Different parameters were studied during the process; the withdrawal speed, which conditions the final thickness of the layers upon dip-coating theory, the concentration of the solutions, and the drying time. To influence the drying time, different infrared lamps were used to heat up the substrate after withdrawal. Some results are represented in **Figure 6.11a-c**, which shows both the spectra measured in six points across the sample as well as a picture of the latter (in the inset). From left to right, the withdrawal speed is progressively increased, together with the power of the lamp used for the drying process. The first samples did not show a clear presence of photonic structure (**Figure 6.11a**). Improving the conditions lead to the formation of a beautiful but inhomogeneous structure, with peaks reflecting different wavelengths depending on the spatial position (**Figure 6.11b**). The optimization of the parameters led to a uniform sample, with consistent reflectance spectra over its extension as reported in **Figure 6.11c**.

These results are particularly interesting as the dip-coating process is automatized and allows to produce DBR over large areas, which is generally extremely difficult with the spin-coating technique.

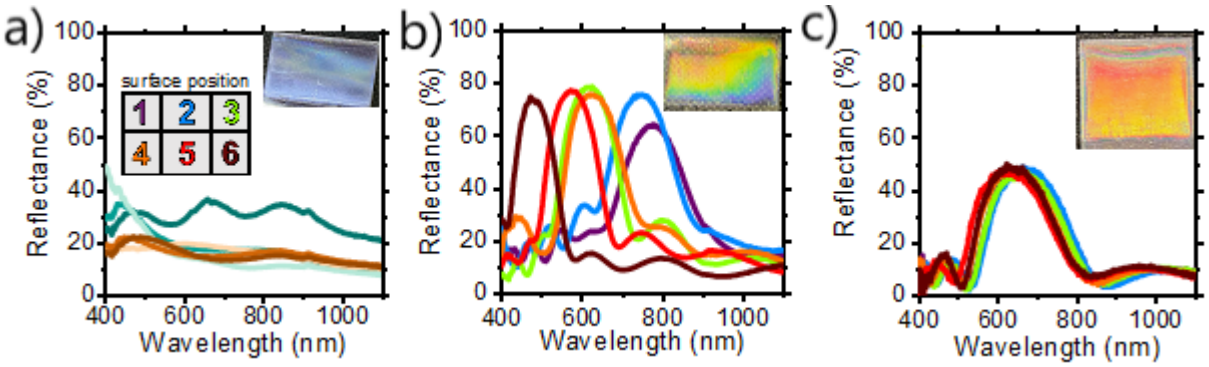

Figure 6.11. *6-points plot of DBRs fabricated via dip-coating with the rearranged 3d-printer. From a to c, the quality gets progressively better increasing withdrawal speed and lamp power.* Credits: M. Martusciello.

Bibliography

1. E. Benvenuti, A. Lanfranchi, S. Moschetto, M. Natali, M. Angelini, P. Lova, F. Prescimone, V. Ragona, D. Comoretto, M. Prosa, M. Bolognesi , S. Toffanin. *J. Mater. Chem. C,* **12**, 12, 4243, (**2024**)

2. H. Megahd, M. Villarreal Brito, A. Lanfranchi, P. Stagnaro, P. Lova , D. Comoretto. *Materials Chemistry Frontiers,* **6**, 17, 2413, (**2022**)

3. H. Megahd, P. Lova, S. Sardar, C. D'Andrea, A. Lanfranchi, B. Koszarna, M. Patrini, D. T. Gryko , D. Comoretto. *ACS Omega*, **7**, 18, 15499, (**2022**)

4. M. Martusciello, A. Lanfranchi, M. Castellano, M. Patrini, P. Lova , D. Comoretto. *ACS Appl. Mater. Interfaces*, **16**, 38, 51384, (**2024**)

5. Z. Baouch, R. Vezzoli, J. Koster, A. Costanzo, A. Lanfranchi, D. Cavallo , C. McIlroy. *Add. Manufactur.*, **83**, 104063, (**2024**)

6. P. S. Stefano Vincenzo Radice, Davide Comoretto, Serena Gazzo, *One-dimensional planar photonic crystals including fluoropolymer compositions and corresponding fabrication methods*, WO 2016/087439 Al (**2016**)

7. P. Lova, G. Manfredi , D. Comoretto. *Adv. Opt. Mater.*, **6**, 24, 1800730, (**2018**)

8. H. Megahd, D. Comoretto , P. Lova. *Opt. Mater. X*, **13**, 100130, (**2022**)

9. P. Lova, M. Olivieri, A. Surace, G. Topcu, M. Emirdag-Eanes, M. M. Demir , D. Comoretto, *Crystals*, 10, **2020**

10. H. A. Macleod, *Thin-Film Optical Filters, 5th Edition.* CRC Press, Boca Raton, FL (USA), **2017**

11. B. E. A. Saleh , M. C. Teich, *Fundamentals of Photonics.* John Wiley & Sons, **2019**

12. E. D. Głowacki, H. Coskun, M. A. Blood-Forsythe, U. Monkowius, L. Leonat, M. Grzybowski, D. Gryko, M. S. White, A. Aspuru-Guzik , N. S. Sariciftci. *Org. Electron.*, **15**, 12, 3521, (**2014**)

13. G. Giusfredi, *Manuale di Ottica.* Springer, Rome (IT), **2015**

14. D. G. Lidzey, Strong Optical Coupling in Organic Semiconductor Microcavities, in Thin Films and Nanostructures, Academic Press, **2003**

15. D. G. Lidzey, D. D. C. Bradley, M. S. Skolnick, T. Virgili, S. Walker , D. M. Whittaker. *Nature*, **395**, 6697, 53, (**1998**)

16. A. V. Zasedatelev, A. V. Baranikov, D. Urbonas, F. Scafirimuto, U. Scherf, T. Stöferle, R. F. Mahrt , P. G. Lagoudakis. *Nature Photonics*, **13**, 6, 378, (**2019**)

17. Y. Zakharko, A. Graf , J. Zaumseil. *Nano Lett.*, **16**, 10, 6504, (**2016**)

18. N. J. Herrmann, M. Hertzog, A. Mischok, M. C. Gather , J. Zaumseil. *ACS Appl. Opt. Mater.*, **2**, 8, 1619, (**2024**)

19. J. D. Plumhof, T. Stöferle, L. Mai, U. Scherf , R. F. Mahrt. *Nat. Mater.*, **13**, 3, 247, (**2014**)

20. D. G. Lidzey , D. M. Coles, Strong Coupling in Organic and Hybrid-Semiconductor Microcavity Structures, in Organic and Hybrid Photonic Crystals, Springer International Publishing, Cham, **2015**

21. H. Megahd, C. Oldani, S. Radice, A. Lanfranchi, M. Patrini, P. Lova , D. Comoretto. *Adv. Opt. Mater.*, **9**, 5, 2002006, (**2021**)

22. L. Magnasco, A. Lanfranchi, M. Martusciello, H. Megahd, G. Manfredi, P. Lova, B. Koszarna, D. T. Gryko , D. Comoretto. *ACS Omega*, **9**, 41, 42375, (**2024**)

23. J. S. I. M. Ward, *Mechanical Properties of Solid Polymers, 3rd Edition.* John Wiley & Sons, Ltd, London (UK), **2012**

24. H. L. S. Anil K. Bhowmick, *Handbook of Elastomers, 2nd Edition.* CRC Press, Boca Raton, FL (USA), **2001**

25. M. Doshi, A. Mahale, S. Kumar Singh , S. Deshmukh. *Mater. Today Proc.*, **50**, 2269, (**2022**)

26. N. Bachhar, A. Gudadhe, A. Kumar, P. Andrade , G. Kumaraswamy. *Bull. Mater. Sci.*, **43**, 1, 171, (**2020**)

27. A. Vital, M. Vayer, T. Tillocher, R. Dussart, M. Boufnichel , C. Sinturel. *Appl. Surf. Sci.*, **393**, (**2017**)

28. Z. Zhang, F. Peng , K. G. Kornev, *Micromachines*, 13, **2022**

Thesis Conclusion - Final Considerations.

During my master's Thesis, I recollect memories of discussing with my former colleague and friend Heba Megahd. I clearly remember saying something about not being cut for Academia, and surely not for a PhD. Almost three and a half years later, here I am trying to wrap up the conclusion of this summary of these challenging, stressful, but undeniably amazing years. Maybe I was wrong to not being cut for the PhD after all – even though, I'll let others judge on this.

I found it very challenging to decide what exactly I could put inside this section. The bland list of nice results obtained sounded fine, but very boring and a bit unnecessary; each chapter already has its own Conclusions, which are – how to say, conclusive on their own. **Chapters 2** and **3** have also the conclusions written in their respective reference papers, as **Chapter 6** does. Therefore, I decided to write a conclusion trying to combine the two aspects of the PhD, the scientific one and the human one, to write something unusual, with more general – perhaps more personal – considerations.

I found working in the field of photonics for thermal management very stimulating, and I am glad I could perform this research; starting from the beginning, the fabrication of the first aegises presented a series of technical challenges. Indeed, the choice of materials, the design of structures able to reflect sufficient near infrared light was not trivial, as it was not trivial to design and assemble setups to observe the thermal shielding effect. The solutions joined many disciplines, physics, chemistry, material science, a little bit of engineering – or tinkering if you will – and a fair share of code development. I would say that I thrived in the interdisciplinarity I was forced to adapt to, as it is probably my favorite aspect of doing research.

In this regard, the work was built from little up to quite interesting achievements; all-polymer distributed Bragg reflectors reflecting in the near-infrared range were developed and their efficiency in the thermal shielding field was investigated using a variety of custom-made setups. In the first place, this allowed us to obtain a first confirmation of the efficacy of all-polymer distributed Bragg reflectors as aegises against overheating, obtaining efficiencies as high as 21 % (or 52 % in extreme cases) in heating reduction. On the other hand, an overview of the best all-polymer structures to perform as thermal shields, which resulted being superperiodic and tandem ones, was presented. This first investigation allowed to follow up with a more thorough work, going in-depth in modeling theoretically the thermal shielding efficacy of a known structure, whereas initially only a qualitatively correct parameter, the spectral coverage, was linked to the aegises' efficiency. The latter model allowed to reverse engineer a best-performing structure to pursue the research comparing different materials as building blocks for aegises. Here, the results were impressive; the best-performing

material pair, formed by the technical polymers Aquivion and poly (*N*-vinylcarbazole) provided efficiencies as high as 27 %, outperforming commodities as the cellulose acetate/polystyrene pair only attained 6 %. In addition to the high performances, these materials can allow for a consistent materials saving with respect to less-performing ones. The complete rationale developed, and the efficiencies obtained are very promising towards the implementation of these kinds of structures as part of the efforts towards energy efficiency and sustainability of our lifestyle.

I carried over the same mindset and tinkering when working on radiative cooling, this time insisting on other aspects, developing knowledge quite outside that shared by research group. Indeed, everything was new, both in the fundamentals of the phenomenon as well as in the fabrication of effective samples, and many trials, errors, solutions and paths needed to be explored. Notwithstanding the difficulties, promising results were obtained in this field. In the first place, I covered the theoretical and experimental aspects by developing a complete model for the phenomenon and implementing it in Matlab, as well as assembling a portable setup able to measure the phenomenon outside of laboratory conditions and in the environment. Additionally, interesting results were obtained in the development of porous white scatterers, with cellulose acetate samples only heating up slightly under strong summer sun (+3.2 °C under direct sunlight) and achieving subambient cooling in the shadow (-1.7 °C). Preliminary results on upcycled poly(vinyl chloride) waste were interesting as well, attaining subambient cooling under winter Sun. These results are especially stimulating, alongside the future perspective of joining aegises to white reflectors to achieve sub-ambient cooling as predicted by the model.

Changing topic completely, I was glad I could experience a different viewpoint on science as well as a profoundly different environment with the spin-off research I performed at Lausanne; it allowed me to get a better understanding of the physics and fundamentals of lasers and light emission, as well as on the assembly of optical setups. Additionally, I could see scientific research in a group strictly physics/electronic engineering oriented, which I felt extremely formative. In general, the scientific results obtained during the period were interesting as well, as I built an external cavity laser assembly from scratch, able to receive optical feedback from even low-reflectance mirrors such as bare glass. Additionally, I could prove distributed Bragg reflectors such as those initially developed for thermal shielding can perform effectively as outcoupling mirrors, envisaging a future development of the work in the use of mechanochromic distributed Bragg reflectors or optical microcavities as wavelength-selective outcouplers.

Last, I was thrilled by the possibility to expand my horizon further via the many collaborations I had during these years – most, but not all reported in **Chapter 6**. Of course, they were centered on the skills I developed while working on my main research topic, such as the use of distributed Bragg-

reflectors in various fields. Emission control and strong coupling, as well as sensing – as part of an on-chip all-organic integrated sensing platform, as stretchable samples whose optical response varied with respect to stress and strain, and samples fluorescing differently upon absorption of analytes – were investigated. With each of these works, and for the more technical implementation of infrared thermal imaging in the 3d-printing workflow and the conversion of a 3d-printer in a dip coater for distributed Bragg reflectors, I could add bits here and there to my knowledge baggage.

In general, this is what I appreciated the most, for whom I developed a love and knack during my PhD: the continuous challenges, the obstacles, the strife to overcome them. The need and desire of knowing more, of discovering new problems in search of a solution, of coming up with ideas to solve them. Never yielding, never stopping, no matter what. And this, if I learned something in the last years, is doing science.

And with all the accumulated knowledge, I cannot do otherwise than borrowing my closing lines from the words of Ulysses:

I am a part of all that I have met;
Yet all experience is an arch wherethro'
Gleams that untravell'd world whose margin fades
For ever and forever when I move.

A. Tennyson, *Ulysses*

Acknowledgements

I thank all the people who supported me during these years.

First and foremost, of course my parents, standing by my side unconditionally, always pushing me up and forward. There are no words to express my gratitude for them. Thanks to Vavà and her family, supportive and loving; and then all my uncles, aunts and cousins. Thanks to my girlfriend and all my friends, my happiness pill during free time.

Inside of UniGe, I would like to thank of course my supervisor, Davide. He is always there, always supportive and available for advice (and sweet treats), always blasting new ideas. I think I could not have asked for a better supervisor. With him, I thank Paola; she is the always vigilant frontline helper providing advice, assistance and proofreading. It is definitely a pleasure to work with both of them.

Of course, I would like to thank the colleagues that worked with me during these years; thanks to them, the stress and anxiety of experiments not working was greatly relieved. I have special acknowledgement for Heba, my *senpai*, who helped me greatly, and for E., my historical office and conference mate; we had a lot of fun together in Italy and abroad. Then I thank every member of *Chokkino*; our time together inside and outside the walls of UniGe was delightful. Lastly, thanks to the current members of the lab, Daniela, Francesco (my Pixie), Agnese and Alessandro for keeping the Lab a relaxed and productive environment.

From Lausanne, I would like to thank Cristina, HyLab's supervisor, for having me there during my period abroad. I am grateful to HyLab's group for accepting and befriending me almost immediately; I especially thank Zari, with whom I shared the difficulties of the project, and Francesco, who couldn't have helped me more there. Last but not least, thank you Luc, for making me feel home inside my Swiss home. Hope to see all of you again, guys.

There are indeed more people I would like to thank for their support, but I would risk losing someone along the way. If I already forgot someone, *credete che non s'è fatto apposta*.

Appendices

Appendix A. Theory of distributed Bragg reflectors

A.1. Fresnel Coefficients.[1, 2] The latter regulate the reflection and refraction at interfaces, defining the ratio between the electric fields of the incident ($E_{s/p,I}$), reflected ($E_{s/p,R}$) and transmitted ($E_{s/p,T}$) beams for polarizations *s* and *p*:

$$\frac{E_{s,R}}{E_{s,I}} = r_s = \frac{n_1 \cos\theta_I - n_2 \cos\theta_T}{n_1 \cos\theta_I + n_2 \cos\theta_T} \quad (A.1.1) \qquad \frac{E_{p,R}}{E_{p,I}} = r_p = \frac{n_2 \cos\theta_I - n_1 \cos\theta_T}{n_1 \cos\theta_I + n_2 \cos\theta_T} \quad (A.1.2)$$

$$\frac{E_{s,T}}{E_{s,I}} = t_s = \frac{2\, n_1 \cos\theta_T}{n_1 \cos\theta_I + n_2 \cos\theta_T} \quad (A.1.3) \qquad \frac{E_{p,T}}{E_{p,I}} = t_p = \frac{2\, n_1 \cos\theta_T}{n_2 \cos\theta_I + n_1 \cos\theta_T} \quad (A.1.4)$$

And in turn give the coefficients for reflectance and transmittance, relative to intensities instead that to fields:

$$R_{s/p} = \left|r_{s/p}\right|^2 \quad (A.1.5)$$

And

$$T_{s/p} = \frac{Re(n_2 \cos\theta_T)}{Re(n_1 \cos\theta_I)} \left|t_{s/p}\right|^2 \quad (A.1.6)$$

The behavior of intensity coefficients is reported in Figure A.1.1.

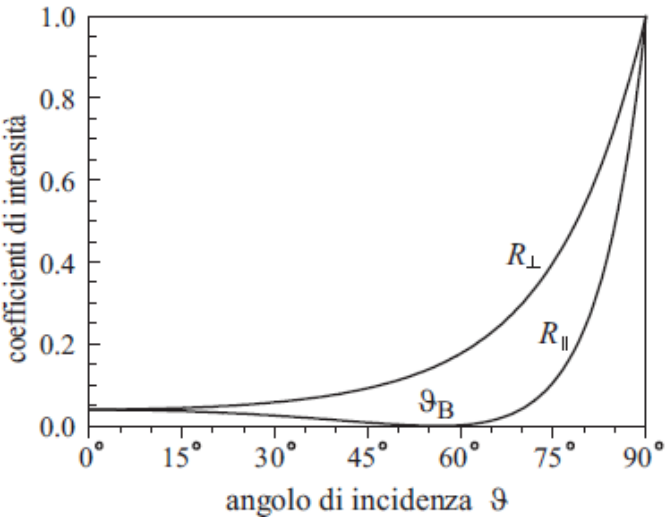

Figure A.1.1. *Behaviour of intensity Fresnel coefficients for increasing incidence angle of impinging radiation for p polarization ($R_{//}$) and s polarization ($R_\perp$). Brewster angle is reported as θ_B.* Reproduced from G. Giusfredi, *Manuale di Ottica*.

A.2. Transfer Matrix Method.[1] Let us start by considering a monochromatic plane wave propagating inside a multilayer. The general equation in complex notation of a plane wave propagating over time *t* along the axis *z* is:

$$\mathbf{E} = \mathbf{E_0} e^{i\varphi} e^{i\left[\omega\left(t - \frac{N_m z}{c}\right)\right]} \tag{A. 2.1}$$

Where E is the electric field, $\mathbf{E_0}$ the amplitude of the wave, ω its angular frequency, φ its phase, c the speed of light and N_m the complex refractive index of the medium. At any interface, since no physical mechanism can change the wave's frequency, the field is reflected and refracted according to a multiplication by Fresnel's coefficients (see **Equations A.1.1-A.1.4**):

$$E_R = r \cdot E_I \tag{A. 2.2}$$

$$E_T = t \cdot E_I \tag{A. 2.3}$$

And via Snell's laws for reflection and refraction respectively:

$$\sin(\theta_I) = sin(\theta_R) \tag{A. 2.4}$$

$$n_1 \sin(\theta_I) = n_2 sin(\theta_T) \tag{A. 2.5}$$

Now, **Figure A.2.1a** represent schematically the propagation of a monochromatic plane wave inside a multilayer structure at normal incidence. Due to refraction/reflection occurring at each interface, there are infinite transmitted and reflected rays, propagating respectively forward (in the same direction of the original ray) and backward (in the opposite direction with respect to the original ray). Each reflection/refraction influences the respective wave via multiplication by the appropriate complex Fresnel's coefficient, which can be obtained as per **Equation A.1.1-A.1.4**, but their frequency is unchanged. Since the sum of plane waves with equal frequency is still a plane wave with that frequency, the situation can be strongly simplified, as schematized in **Figure A.2.1b**.

Within the n^{th} layer, there are now only two plane waves: one propagating forward, representing the sum of all forward propagating transmitted waves, and one propagating backward that is the sum of all backward propagating ones.

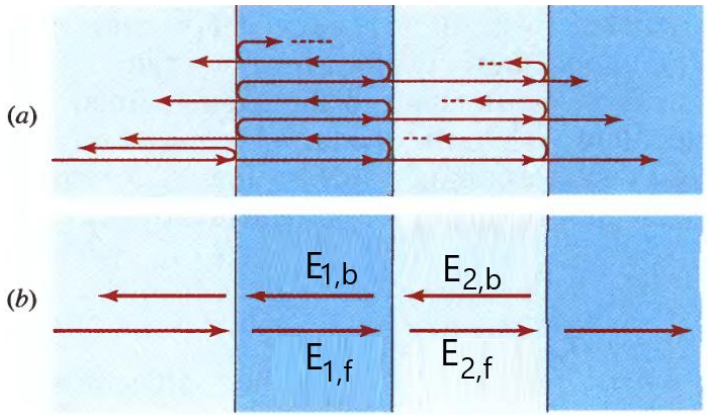

Figure A.2.1: **a)** *Representation at normal incidence of the infinite reflections and transmissions experienced by light in the first two layers of a multilayer structure, and* **b)** *how these can be simplified into a pair of waves per layer*. Adapted from B. A. Saleh, *Fundamentals of Photonics*

These single waves are much easier to deal with, as their crossing between the interfaces is regulated by single Fresnel coefficients. Let us therefore consider a situation as represented in **Figure A.2.2a**, where the constraint of normal incidence has been relaxed. Referring specifically to **Figure A.2.2b**, let us define $E_{m-1,f}$ and $E_{m-1,b}$ the electric fields propagating forward and backward respectively in layer $m-1$ and let $E_{m,f}$ $E_{m,b}$ denote the corresponding electric fields in layer m.

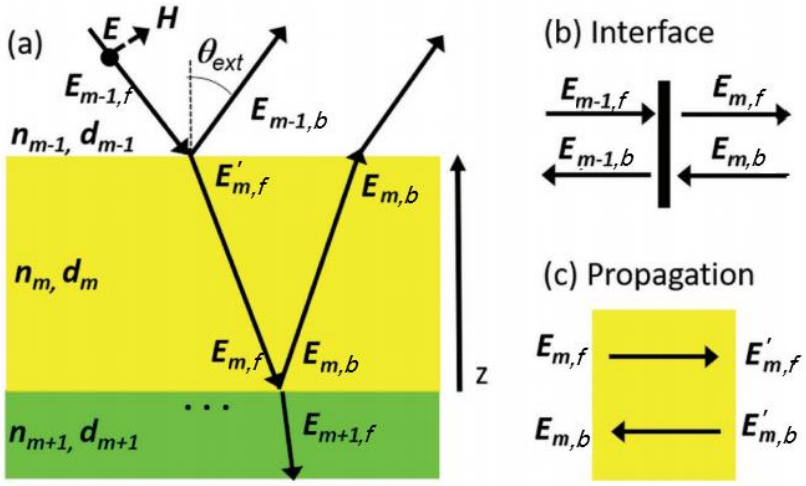

Figure A.2.2 a) *Representation of the fields summarized in forward and backward propagating waves in the m^{th} layer of a multilayer structure* **b)** *schematic of the interface* **c)** *schematic of the propagation*.

Using Fresnel coefficients and considering the various reflections and transmissions, we obtain:

$$\begin{cases} E_{m,f} = t_{m-1,m}E_{m-1,f} + r_{m,m-1}E_{m,b} \\ E_{m-1,b} = r_{m-1,m}E_{m-1,f} + t_{m,m-1}E_{m,b} \end{cases} \quad \text{(A. 2.6)}$$

This mixed form is useless, being $E_{m,b}$ unknown. The terms must be arranged with simple algebraic manipulations:

$$\begin{cases} E_{m,f} = \dfrac{1}{t_{n,n-1}}\left[\left(t_{m,m-1}t_{m-1,m} - r_{m,m-1}r_{m-1,m}\right)E_{m-1,f} + r_{m,m-1}E_{m-1,b}\right] \\ E_{m,b} = \dfrac{1}{t_{m,m-1}}\left(-r_{m-1,m}E_{m-1,f} + E_{m-1,b}\right) \end{cases} \quad \text{(A. 2.7)}$$

The system in equation (9.1) can be rewritten using matrix notation, allowing the introduction of the interface matrix J.

$$\begin{pmatrix} E_{m,f} \\ E_{m,b} \end{pmatrix} = \frac{1}{t_{m,m-1}}\begin{pmatrix} t_{m,m-1}t_{m-1,m} - r_{m,m-1}r_{m-1,m} & r_{m,m-1} \\ -r_{m-1,m} & 1 \end{pmatrix}\begin{pmatrix} E_{m-1,f} \\ E_{m-1,b} \end{pmatrix} =$$

$$= J_{m,m-1} \times \begin{pmatrix} E_{m-1,f} \\ E_{m-1,b} \end{pmatrix} \quad \text{(A.2.8)}$$

Considering now **Figure A.2.2c**, the propagation of radiation from one end of layer *m* to the other end over its thickness d_m can be expressed as:

$$\begin{cases} E'_{m,f} = e^{-i\varphi}E_{m,f} \\ E'_{m,b} = e^{i\varphi}E_{m,b} \end{cases} \qquad \varphi = \frac{2\pi}{\lambda}\, N_m\, d_m \cos\theta_m \quad \text{(A. 2.9)}$$

With N_m refractive index of the layer and θ_m being the propagation angle in the layer. This simply states the phase change the way undergoes while crossing the layer – plus the eventual absorption if N_m is complex with nonzero imaginary part. In matrix form, this is expressed by the introduction of the propagation matrix P_m:

$$\begin{pmatrix} E'_{m,f} \\ E'_{m,b} \end{pmatrix} = \begin{pmatrix} e^{-i\varphi} & 0 \\ 0 & e^{i\varphi} \end{pmatrix} \times \begin{pmatrix} E_{m,f} \\ E_{m,b} \end{pmatrix} = P_m \times \begin{pmatrix} E_{m,f} \\ E_{m,b} \end{pmatrix} \quad \text{(A. 2.10)}$$

. Thus, both propagation within media and crossing of interfaces can be considered. Since it has been possible to uniquely relate the fields in layer *(m–1)* to those in layer *m* through a matrix product considering layer *(m+1)*, the following holds:

$$\begin{cases} \begin{pmatrix} E_{m,f} \\ E_{m,b} \end{pmatrix} = J_{\,n,n-1} \times \begin{pmatrix} E_{m-1,f} \\ E_{m-1,b} \end{pmatrix} & \text{(A. 2.11)} \\ \begin{pmatrix} E_{m+1,f} \\ E_{m+1,b} \end{pmatrix} = J_{\,m+1,m} \times \mathrm{P}_m \times \begin{pmatrix} E_{m,f} \\ E_{m,b} \end{pmatrix} & \text{(A. 2.12)} \end{cases}$$

Or substituting **(A.2.11)** in **(A.2.12)**.

$$\begin{pmatrix} E_{m+1,f} \\ E_{m+1,b} \end{pmatrix} = J_{\,m+1,m} \times \mathrm{P}_m \times J_{\,m,m-1} \times \begin{pmatrix} E_{m-1,f} \\ E_{m-1,b} \end{pmatrix} \qquad \text{(A. 2.13)}$$

The fields before a layer are hence related to the fields observed after crossing the entire layer. It follows that, if there were *i* layers instead of just one, the situation would be:

$$\begin{pmatrix} E_{m+i,f} \\ E_{m+i,b} \end{pmatrix} = J_{\,m+i,m+i-1} \times \mathrm{P}_{m+i-1} \times \ \ldots \ \times \mathrm{P}_m \times J_{\,n,n-1} \times \begin{pmatrix} E_{m-1,f} \\ E_{m-1,b} \end{pmatrix} = M_{tot} \times \begin{pmatrix} E_{m-1,f} \\ E_{m-1,b} \end{pmatrix}$$

The effect on electromagnetic waves by the entire multilayer structure has been reduced to a matrix, which is the product of matrices that can be calculated based on known quantities, i.e., the thicknesses and refractive indices of the layers, the wavelength, and the angle of incidence of the light. Knowing these quantities is sufficient to write the interface matrices J and the propagation matrices P for each layer and interface, and then calculate the total matrix M_{tot}, which is called the transfer matrix of the system. This essentially solves the problem. In fact, considering the entire structure, we have:

$$\begin{pmatrix} E_f \\ E_b \end{pmatrix} = M_{tot} \times \begin{pmatrix} E_{0,f} \\ E_{0,b} \end{pmatrix} \qquad \text{(A. 2.14)}$$

Now, $E_{0,f}$ is the field of the incident wave (propagating forward, before the structure), $E_{0,b}$ is the field of the reflected wave (propagating backward, before the structure), while E_f is the field of the transmitted wave (propagating forward, after the structure). $E_b = 0$ assuming the light arrives from only one direction. Thus, we have:

$$\begin{pmatrix} E_t \\ 0 \end{pmatrix} = \begin{pmatrix} A & B \\ C & D \end{pmatrix} \times \begin{pmatrix} E_i \\ E_r \end{pmatrix} \qquad \text{(A. 2.15)}$$

Skipping some trivial algebra, this can be written in system notation and rearranged as:

$$\begin{cases} \dfrac{E_t}{E_i} = t = \dfrac{1}{D}\,(AD - BC) \\ \dfrac{E_r}{E_i} = r = -\dfrac{C}{D} \end{cases} \qquad \text{(A. 2.16)}$$

Therefore, from the elements of the transfer matrix, the reflection and transmission coefficients of the structure can be obtained. The reflectance and transmittance of the structure can be easily derived from *r* and *t* by taking the square modulus (corrected for angle cosine and refractive index for the transmission case).

A.2.1. Intensity Matrix.[3] Everything described here holds true as long as the layers thickness is lower than the coherence length of the incident light. If a layer is thicker than that, light will stop being coherent rendering any consideration regarding the phase change over propagation meaningless. Light intensities must be considered instead of fields in this case. This is usually true for DBRs' substrates, as they are most likely to be cast on a relatively thick glass and analyzed via white light, which typically has a coherence length on the order of magnitude of tens of micrometers. In this case, the layer must be treated differently, using appropriate an appropriate intensity-based interface matrix:

$$J^{int}_{m,m+1} = \frac{1}{\left|t_{m,m+1}\right|^2}\begin{pmatrix} 1 & -\left|r_{m+1,m}\right|^2 \\ \left|r_{m,m+1}\right|^2 & \left|t_{m,m+1}t_{m+1,m}\right|^2 - \left|r_{m,m+1}r_{m+1,m}\right|^2 \end{pmatrix} \qquad \text{(A. 2.17)}$$

And the incoherent layer gets its own intensity matrix:

$$J^{int}_{m-1,m+1} = J^{int}_{m-1,m} \times \mathrm{P}^{int}_{m} \times J^{int}_{m,m+1} \qquad \text{(A. 2.18)}$$

For DBRs on substrates, $J^{int}_{m-1,m}$ corresponds to the intensity matrix of the whole DBR, obtained from the coefficients of M_{tot} (**A.2.14 - A.2.16**) whereas $J^{int}_{m,m+1}$ corresponds to the interface between substrate and air. The incoherent propagation matrix is obtained just by the square module of the components of the coherent one; this means it corresponds to the identity matrix as long as the substrate is transparent (which usually is the case).

Appendix B. Experimental Details.

B.1. Chapter 1.

The modeling of the aegises reflectance spectra was performed using custom MatLab codes based on the transfer matrix method described in **Appendix A.2**. The materials refractive index dispersions as well as the incoherent glass substrate were taken into account when not specified otherwise.

B.2. Chapter 2.

B.2.1. Transmittance Measurements. A custom setup based on optical fibers was used to measure the reflectance spectra of the aegises. Samples were placed on a rotating stage in front of collimated, polarized white light from DH-2000-BAL (Ocean Optics) deuterium and tungsten–halogen sources (spectral range 230–2500 nm). The transmitted spectrum was relayed to an AvaSpec-ULS4096CL-EVO detector (Complementary Metal-Oxide Semiconductor; spectral range 200–1100 nm; resolution 1.3 nm), and to an Arcoptix NIR-Rocket Fourier Transform-interferometer (900−2600 nm, resolution 8 cm-1), for collection. Transmittance was measured as the ratio between the transmitted signal with and without the sample in place.

For the transmittance of liquid paraffin, 1 mm and 1 cm optical path were used to investigate the 2500-1100 and the 1100-700 nm region respectively; for the transmittance of Parafilm, source and collector were placed close together to reduce scattering.

B.2.2. Aegises Fabrication: Aegises were spin-coated on clear glass substrates sized 25 × 25 × 1 mm3, using poly(N-vinylcarbazole) (Carlo Erba, Mw = 135000) solvated in toluene (Aldrich, reagent grade, ≥ 98 %), alternating it with CA (Aldrich, Mw = 50000) solvated in 4-hydroxy-4-methyl-2-pentanone (Aldrich, reagent grade, ≥ 98 %), poly(acrylic acid) (Aldrich, Mw = 2000) solvated in 4-hydroxy-2-pentanol (Aldrich, reagent grade, ≥ 98 %) was used instead of CA. Layers were cast by dynamically spin-coating 100 µl of polymer solutions, alternating between high and low index polymers. The number of layers constituting each structure is reported in Table 2.1. Concentrations used varied depending on the aegis, remaining in the 40-55 mg ml^{-1} range for PVK, 30-45 mg ml^{-1} for CA, and 60-75 mg ml^{-1} for PAA. Rotation speeds used were also typical of spin-coating, ranging between 80 and 200 revolutions per second (4800 to 12000 rpm).

B.2.3. Reflectance Measurements. A custom setup based on optical fibers was used to measure the reflectance spectra of the aegises. Samples were placed under an Avantes BIF-600 UV-VIS-NIR optical fiber. The incident light beam was impinged on the PAE surface from DH-2000-BAL (Ocean Optics) deuterium and tungsten–halogen sources (spectral range 230–2500 nm). The reflected signal was relayed to an AvaSpec-ULS4096CL-EVO detector (Complementary Metal-Oxide Semiconductor; spectral range 200–1100 nm; resolution 1.3 nm), and to an Arcoptix NIR-Rocket

Fourier Transform-interferometer (900−2600 nm, resolution 8 cm-1), for collection. The reflectance was measured as the ratio between the collected signal and a reference, which is an aluminum mirror.

B.2.4. *Scanning Electron Microscope (SEM) Measurements*. Samples were at first frozen in liquid nitrogen, then fractured to reveal the cross section. A thin carbon layer was deposed on the fracture edge by a high vacuum evaporator (Polaron 6700). SEM measurements were then performed using FE-SEM Zeiss SUPRA 40 VP at an acceleration voltage of 5 kV. Images were then analyzed with the software ImageJ and thicknesses extrapolated when possible.

B.2.5. *Thermal Experiments.* As stated in the main text, to assess the efficiency of aegises in thermal shielding, different homemade setups were designed and fabricated. Light source for the Parafilm measurement (setup represented in Figure 2.7a) was an illuminator (Edmund Optics Model 21AC), its light carried by the associated polymer optical fiber. Parafilm temperature was measured with a Testo 110 digital thermometer (range -50/150 °C, resolution 0.1 °C) with a flat probe. For water measurements a PC-linkable, dual channel thermocouple thermometer TSP-01 from Thorlabs (range -20/110 °C, resolution 0.05 °C) with two immersion probes was used instead of Testo. The incandescent lamp for the setup represented in Figure 2.7b was a Philips IR250, 250 W. The circuit for the setup represented in **Figure 2.7d-e** powered, with a current of 59 mA, two groups of four LEDs each (Thorlabs 5 mW 970 nm). Those provided illumination to each of the two water vials through the aegis/reference, as visible in Figure **Figure 2.7d-e**. The main body of the TSP-01 thermometer was used to measure ambient temperature near the vials.

B.3. Chapter 3.

B.3.1. Aegises Fabrication. Aegises were created by spin-coating on clear glass substrates sized 25 × 25 × 1 mm3, using polystyrene (PS, Aldrich, Mw = 192000) solvated in toluene, poly(*N*-vinylcarbazole (PVK, Carlo Erba, Mw = 135000) solvated in toluene materials and cellulose acetate (CA, Aldrich, Mw = 50000) solvated in 4-hydroxy-4-methyl-2-pentanone and an Aquivion D79-25BS water dispersion (Solvay Specialty Polymers). Layers were cast by dynamic spin-coating of 150 µl of polymer solutions, alternating between high and low index polymers, respectively pairing PS-CA, PVK-CA and PVK-AQ. Each structure is made up of 4 DBRs with 8 BL each, stacked one on top of the other, ordered from the thickest to the thinnest. A capping layer of high-index material raise the total number of layers to 65 for each structure. Concentrations used varied depending on the aegis, remaining in the 45-50 mg ml-1 range for PVK, 32-35 mg ml^{-1} range for CA, 40 mg ml^{-1} for PS, and 2 AQ : 7 Ethanol for AQ. Rotation speeds used were also typical of spin-coating, ranging between 60 and 170 revolutions per second (3600 and 10200 rpm).

B.3.2. Reflectance Measurements. See B.2.2.

B.3.3. Transmittance Measurements. See B.2.3.

B.3.4. Numerical Calculations. See B.2.4. The codes were modified to allow calculations of the rational described thoroughly in **Chapter 3**.

B.3.5. Thermal Experiments. A PC-linkable, dual channel thermocouple thermometer TSP-01 from Thorlabs (range -20/110 °C, resolution 0.05 °C) with two immersion probes was used. Light source was the incandescent lamp Philips IR250, 250 W, concentrated to a spot 25 mm in width by an aluminum cone. For the thermal images, a thermal camera FLIR T560 (Accuracy @25°C, 2 °C, Measurement range -20 : 120 °C, Sensitivity <30 mK) was used in conjunction with FLIR Research Studio software.

B.4. Chapter 4.

B.4.1. Calculation of Atmospheric Transmittance. The software MODTRAN (MODerate resolution atmospheric TRANsmission) was used to simulate the transmittances reported in **Figure 4.1b**.[4] The software simulate the scattering and absorption due to atmosphere composition to provide an estimate of the atmospheric transmittance based on various parameters; the default curves relative to Mid-Latitude Winter and Summer, Tropical and Sub-Arctic climates were used. I report some of the parameters in **Table B.4.1**.

Table B.4.1. *Main parameters of the MODTRAN model for atmosphere transmittance*.

Model	Water Vapor Column (atm-cm)[a]	Ozone Column (atm-cm)[a]	Ground Temperature (°C)	Aerosol Model
Sub-Arctic Winter	518	2.50	257	Desert
45° Winter	1059	0.38	272	Urban
45° Summer	3635	0.33	294	Urban
Tropical	5119	0.28	300	Urban

[a] *atm-cm: if all the water vapor/ozone in the vertical column of atmosphere considered was concentrated to saturation, it would reach this height in cm.*

B.4.2. Fabrication of white samples. Acetone (99.8 % Reagent grade, Sigma Aldrich) is used to dissolve cellulose acetate (M_w = 50000, Sigma Aldrich) up to 25 % concentration. The glue-like solution is cast on glass using a 500 μm knife and put in the deionized water bath for nonsolvent induced phase separation kept at room temperature for eight hours. Tetrahydrofuran (Sigma Aldrich)

and *N,N*-dimethylformamide (Sigma Aldrich) in a 50:50 weight ratio are used to dissolve PVC from drug blisters up to 15 % concentration by weight.

B.4.3. Radiative Cooling Setup. Two Thorlabs TSP01-B thermometer with TSP01-TH thermistors (see **B.2.5**) are implemented in the setup. The microcomputer (Raspberry Pi 4B) reads and store the data from the thermometers through a custom python3 routine. To integrate the microcomputer, the resistive touch screen (Waveshare) and the wires to the case I CAD-designed and 3d-printed out of poly(lactic acid) suitable parts. The powerbank used to power the system is a Charmast 26800 mAh.

B.4.4. NIR Measurements. A spectrophotometer (Perkin Elmer Lambda-9, spectral range 175-3300 nm, 2 nm resolution) equipped with a white integrating sphere is used to characterize samples in the NIR range. Reflectance of the sample is measured by placing it to close a gap in the sphere's walls and calculated with respect to a reference which is assumed to be 100 % reflective.

B.4.5. MIR Measurements. A Fourier-Transform Infrared spectrophotometer equipped with Drift aluminum-coated integrating hemisphere was used to perform the analysis (Bruker Vertex 70, Range 400-4000 cm^{-1}, Resolution 4 cm^{-1}). Reflectance is measured with respect to a reference, which is an aluminum mirror.

B.5. Chapter 5.

B.5.1. Assembly Description. The uncoated laser diode (LPS-1550-FC, 1550 nm, multimode, Thorlabs) was mounted on a specific mount (LDM21/M, Thorlabs). To provide current and temperature control to the LD, a current controller (ILX Lightwave LDX-3412, Newport, range 0-200 mA, resolution 0.1 mA) was used in conjunction with a temperature controller (ILX Lightwave LDT-54128, Newport, resolution 0.1 °C). The controllers' outputs are 9- and 15-pins D-Sub connectors. The controllers-to-mount wiring was custom-assembled from cable bundles (MH Connectors) soldered adequately to D-sub connectors to ensure input-output pin correspondence.

A powermeter (Thorlabs PM100D with S122C Germanium photodiode, spectral range 700-1800 nm) was placed along the beam path, 10 cm away from the LD. To measure the spectrum, the powermeter was replaced with a free space-to-fiber coupler, and the signal analyzed via an optical spectrum analyzer (Anritsu Corporation MS9740B, spectral range 600-1750 nm, resolution 0.03 nm).

The HR-AR coated LD is instead a SAL-1550-10 (SacherLaser Gmbh – Discontinued). Reflectance of the facet are HR ≅ 90%, AR ≤ 0.01 %, and the diode is made out of indium phosphide (InP), with the active region most probably made out of indium gallium arsenide phosphide (InGaAsP). The diode is mounted in a standard TO Can configuration 9 mm in diameter, including a monitoring photodiode.

The optical isolator to avoid unwanted feedback is a Thorlabs IO-4-1550-VLP, T = 95 %, Isolation = 38-42 dB.

B.5.2. Metallic Outcoupling Mirrors Design, Fabrication and Characterization. The metallic mirrors used as outcouplers in the experiments here described were designed via a custom python code based on the transfer matrix method (TMM). This allows to calculate the optical response in terms of both reflectance and transmittance of an ensemble of films, known the refractive index dispersion. The code was validated through comparison with already validated MatLab codes developed by the Rely Photonics group at the University of Genoa across the years.[15] The mirrors were fabricated via evaporation with Alliance-Concept EVA 760 in EPFL's clean room at 2 nm/hours evaporation rate over a fused silica substrate. A layer of 2 nm of chromium ensures gold adhesion. The mirrors were afterwards characterized at EPFL with a tunable laser (Menlo) by Z. Basiri measuring their reflectance with respect to a gold mirror reference.

B.5.3. Dielectric Outcoupling Mirrors Design, Fabrication and Characterization. See **B.3.1** for fabrication. The characterization was carried out at EPFL as for the metallic mirrors.

B.6. Chapter 6.

Any experimental detail is described in the referenced paper.

References

1. B. E. A. Saleh , M. C. Teich, *Fundamentals of Photonics.* John Wiley & Sons, **2019**
2. G. Giusfredi, *Manuale di Ottica.* Springer, Rome (IT), **2015**
3. C. C. Katsidis , D. I. Siapkas. *Appl. Opt.*, **41**, 19, (**2002**)
4. MODTRAN, http://modtran.spectral.com/ (accessed December, 2024)